Quantum impurity dynamics

and formation of polarons and bipolarons in Bose-Einstein condensates

Magnus Graf Skou
Department of Physics and Astronomy
Aarhus University, Denmark

Ph.D. Thesis
March 2021

Front cover illustration: Impurities dynamically interacting with a surrounding medium and forming both polarons and bipolarons.

ABSTRACT

Quasiparticles are an important concept in physics since they can reduce the complexity of many quantum systems. The polaron is a prominent example of such a quasiparticle and describes the scenario of an impurity interacting with a surrounding medium. While polarons are significant for the understanding of novel technologies, they are also difficult to study in solid-state materials. In contrast, ultracold gases provide an excellent platform for investigating the behavior of impurities, since these quantum gases are marked by a high degree of purity, low densities and furthermore allow complete tunability of interactions between the atoms.

In this thesis, the dynamics of impurities in ultracold atomic gases is studied experimentally. In particular, a Bose-Einstein condensate of ^{39}K is used as a medium and impurity physics is explored using another quantum state of the potassium atoms. These investigations include interferometric measurements of initial two-body dynamics and the subsequent formation of the polaronic quasiparticle. Interestingly, three distinct regimes of dynamical behavior are identified and the transition times between the regimes are extracted in agreement with theoretical predictions. Moreover, interferometric and spectroscopic polaron results are analyzed and compared, thus providing a complete characterization of the Bose polaron in both time-domain and frequency-domain. Finally, interactions between polarons leading to the emergence of bipolarons are observed using a spectroscopic approach. These measurements reveal the dynamical formation of bipolarons and allow their ground state energies to be obtained, which are successfully compared with predicted values.

The results presented in this thesis thus consolidate and expand the current understanding of polarons and bipolarons in Bose-Einstein condensates. This, in turn, paves the way for new exciting research of quantum impurities and their interactions.

RESUMÉ

DANISH ABSTRACT

Kvasipartikler er et vigtigt koncept inden for fysik, da de kan reducere kompleksiteten af mange kvantesystemer. Polaronen er et prominent eksempel på sådan en kvasipartikel og beskriver scenariet, hvor en urenhed vekselvirker med et omgivende medium. Selvom polaroner er signifikante for forståelsen af nye teknologier, er de også svære at studere i faststof materialer. Ultrakolde gasser er derimod et fortræffeligt system for at undersøge opførslen af urenheder, da disse kvantegasser i særdeleshed er rene, har lave densiteter og derudover kan have fuldstændig justerbare interaktioner imellem atomerne.

I denne afhandling undersøges dynamikken af urenheder i ultrakolde atomare gasser eksperimentelt. Til dette bruges et Bose-Einstein kondensat af ^{39}K som medium, og urenhedsfysik udforskes så ved at benytte en anden kvantetilstand af kalium atomerne. Disse undersøgelser inkluderer interferometriske målinger, som viser både tolegeme dynamik og senere dannelse af den polaroniske kvasipartikel. Tre forskellige regimer af dynamisk opførsel identificeres og tiderne for overgangene imellem disse ekstraheres i overensstemmelse med teoretiske værdier. Derudover analyseres og sammenlignes interferometriske og spektroskopiske polaron resultater, hvilket danner grundlag for en komplet karakterisering af Bose polaronen i både tidsdomæne og frekvensdomæne. Afslutningsvis undersøges interaktionen imellem polaroner, som leder til dannelsen af bipolaroner, ved brug af en spektroskopisk metode. Disse målinger afslører den dynamiske fremkomst af bipolaroner og tillader, at deres grundtilstandsenergier kan bestemmes og sammenlignes med teoretiske værdier.

Resultaterne, som præsenteres i denne afhandling, sørger dermed både for at cementere og udvide den nuværende forståelse af polaroner og bipolaroner i Bose-Einstein kondensater. Dette baner til gengæld vejen for ny, spændende forskning af kvanteurenheder og deres vekselvirkninger.

PREFACE

This thesis presents the highlights of the scientific research I have conducted during my Ph.D. studies. Here, I have been a part of the Ultracold Quantum Gases Group at the Department of Physics and Astronomy at Aarhus University, and the experimental work has been carried out at the Multi Species Quantum Gases Experiment.

The journey towards this thesis began in August 2016, when I joined the group and started my Ph.D. studies. During the next two and a half years, I learned how to operate the laboratory, acquired the first data and eventually obtained my Master's degree in 2019. In the last two years, I have focussed on publishing joint results while also beginning new experimental investigations. This work lays the foundation for the research described in the thesis.

The main subject of this thesis is the experimental investigation of impurity dynamics in Bose-Einstein condensates. However, as the list of publications suggests, I have also been involved in other research topics during my Ph.D. studies. These include investigations of Efimov physics in ^{39}K, time-of-flight expansion of binary mixtures and the observation of a Lee-Huang-Fluid. Nonetheless, I have chosen to focus the thesis on impurity dynamics, since this has been the central part of my research.

This thesis would not have been possible without the help of many people. First, a big thanks to my supervisor Jan Arlt for welcoming warmly in your group and for always having time for deep discussions. You have

taught me how to be a proper scientist with a curios mind, who always strives to understand the world that surrounds us a little better.

A special thanks to Lars Wacker, Kristoffer Theis Skalmstang and Nils Byg Jørgensen, who mentored me when I first joined the experimental team. Because of you, the true spirit of MIX lab endured during my time as a Ph.D. student, and it will always have a special place in my heart.

I would also like to thank Thomas Guldager Skov, with whom I have spent countless hours in the lab. I am certain that our many discussions have broadened our knowledge of both quantum physics and musical genres.

In the last year of my Ph.d. studies, our experimental team grew with Anders Ploug Hansen and Andreas Madsen Morgen, who I would like to thank for our time together. I am sure they will both go on to accomplish great results in the future!

Furthermore, I would like to thank the Lattice and HighRes teams for valuable support, numerous fun events and unforgettable moments. I would also like to thank my other scientific collaborators, both at Aarhus University and abroad, for many fruitful discussions along the way.

A big thanks to my family and friends as well. Your persistent encouragement have been crucial for me, and I will always be grateful for the support I have received.

Lastly, I would like to give a special thanks to Benedicte Ravn, Andreas Madsen Morgen, Thomas Guldager Skov, Mick Kristensen and Jan Arlt for proofreading the thesis.

I hope you will all enjoy reading my thesis!

To my dad, who was there for some of the road but never got to see the end result.

Magnus Graf Skou

LIST OF PUBLICATIONS

L. J. Wacker, N. B. Jørgensen, K. T. Skalmstang, M. G. Skou, A. G. Volosniev, and J. J. Arlt, Temperature dependence of an Efimov resonance in ^{39}K, Phys. Rev. A **98**, 052706 (2018).

K. L. Lee, N. B. Jørgensen, L. J. Wacker, M. G. Skou, K. T. Skalmstang, J. J. Arlt, and N. P. Proukakis, Time-of-flight expansion of binary Bose–Einstein condensates at finite temperature, New J. Phys. **20**, 053004 (2018).

T. G. Skov, M. G. Skou, N. B. Jørgensen, and J. J. Arlt, Observation of a Lee-Huang-Yang Fluid, arXiv:2011.02745 (2020).

M. G. Skou, T. G. Skov, N. B. Jørgensen, K. K. Nielsen, A. Camacho-Guardian, T. Pohl, G. M. Bruun, and J. J. Arlt, Non-equilibrium quantum dynamics and formation of the Bose polaron, Nat. Phys. (2021).

M. G. Skou, T. G. Skov, N. B. Jørgensen, and J. J. Arlt, Initial dynamics of quantum impurities in a Bose–Einstein condensate, Atoms **9**, 22 (2021).

M. G. Skou, T. G. Skov, N. B. Jørgensen, K. K. Nielsen, A. Camacho-Guardian, T. Pohl, G. M. Bruun, and J. J. Arlt, Life and death of the Bose polaron, in preparation.

CONTENTS

CHAPTER 1

INTRODUCTION

Quantum mechanics is founded on the paradigmatic idea that essential properties of nature, such as energy and momentum, are quantized. This theory has led to many profound insights into the universe we live in and has been fundamental for the development of many technologies that we use in our everyday life.

Modern quantum mechanics began at the dawn of the previous century, when Max Planck introduced discrete states of energy as a mathematical tool to explain the spectrum of black-body radiation [1]. The physical implications were subsequently widely considered by his contemporary colleagues, and eventually led Niels Bohr to propose a quantized model of the hydrogen atom [2]. In the following decades, the field of quantum mechanics was further developed by the great minds of Albert Einstein, Louis de Broglie, Erwin Schrödinger, Paul Dirac, Werner Heisenberg and Richard Feynman just to mention a few.

Nowadays, quantum mechanics is extensively used in many areas of physics and has even branched out into quantum chemistry [3] and quantum biology [4]. It has provided the foundation for the groundbreaking inventions of the laser [5] and the transistor [6] that have shaped the society of today. Currently, the frontier is pushed further as novel technologies are explored by simulating their quantum properties in laboratories [7]. These investigations, known as *quantum simulations*, imitate the interactions of complicated quantum systems in well-controlled environments. This complete control of complex quantum systems is one of the hallmarks of the so-called second quantum revolution [8], and in this thesis, quantum simulation of impurity dynamics in ultracold quantum gases is investigated.

1.1 Ultracold quantum gases

Ultracold gases are an excellent test bed for quantum simulation. They are characterized by exceedingly low temperatures, down to only a billionth of a degree above absolute zero, which provides an unprecedented control of their quantum behavior. This is especially true for particles known as bosons, since they accumulate in the quantum mechanical ground state of the system when cooled below a critical temperature. In this extreme regime of temperatures, the system constitutes a special state of matter called a *Bose-Einstein condensate* (BEC), which was predicted by Satyendra Nath Bose and Albert Einstein in the early days of quantum mechanics [9, 10].

Cooling atoms to such low temperatures is exceptionally challenging and it took nearly a century, before it was experimentally feasible to realize and measure BECs. In 1995, three groups reported the observation of a condensate [11–13] and subsequently a fermionic cloud of atoms, known as a Fermi gas, was cooled to quantum degeneracy four years later [14]. Initially, alkali metals were used for these measurements, however, the list of possible candidates has expanded rapidly and now, among others, includes helium [15], alkaline earth metals [16] and rare earth metals [17, 18].

Today, many groups routinely make BECs around the world and even in space [19]. The numerous atomic species with suitable isotopes for cooling to quantum degeneracy allow for many interesting research directions to be pursued. Important experimental techniques include tuning of interactions between atoms, confinement using external trapping potentials and single-atom resolution [20]. This versatile toolbox permits engineering of quantum systems with remarkable precision, which makes ultracold atomic gases an excellent platform for quantum simulation. Using these tools, recent investigations have for instance observed dipolar supersolids [21–23] and studied analogous black-hole radiation in a flowing Bose-Einstein condensate [24]

1.2 Impurities and polarons

Impurities and their interactions with a surrounding medium are a widespread scenario in nature. This ubiquitous concept is e.g. responsible for cloud formation by water condensation on dust particles, and mineral crystals derive their unique colors from their specific impurity composition.

In a quantum mechanical setting, impurities and their interactions can be described as *quasiparticles*. This idea was originally developed by Lev Landau and Solomon Pekar [25] to describe electrons moving through a crystal lattice. Here, the electrons couple with the vibrations of the lattice and form so-called *polarons*. Moreover, it is possible for these polarons to interact with each other and form bound states known as *bipolarons*. Both polarons and bipolarons have important technological aspects [26, 27].

Dilute quantum gases have recently been used extensively to study impurity physics. The ultracold clouds act as an exceedingly pure medium, and their low densities allow the correspondingly slow dynamical evolution to be resolved. Furthermore, interactions between impurities and the medium can be controlled precisely using so-called *Feshbach resonances* [28] by applying a magnetic field to the atoms. This allows complete tunability from weak interactions to the unitary regime, where the interactions are as strong as permitted by the density.

The first studies of polarons in ultracold atomic clouds were conducted in a quantum degenerate Fermi gas. Here, spectroscopy was used to measure the energy of the attractive polaron in 2009 [29] and additional investigations soon followed, revealing the spectral response of both the attractive and the repulsive polaron branch [30–34]. Subsequently, studies also observed the initial dynamics of the impurity in a Fermi gas and the eventual formation of the polaron [35, 36]. Due to the challenging nature of Bose-Einstein condensates, the impurity in a BEC, called the Bose polaron, was not experimentally realized until 2016 [37, 38], and so far its dynamical evolution has remained elusive to observation. However, investigations of the Bose polaron are particular important for expanding the current knowledge of the generic solid-state polaron, since interactions of the impurity with the bosonic nature of the medium more closely resemble the scenario of electrons coupling to phononic vibrations in a crystal lattice.

1.3 Thesis outline

This thesis investigates impurity dynamics in Bose-Einstein condensates and is structured as follows.

Chapter 2: Polarons in quantum gases

The key concepts of polarons are introduced in the context of ultracold quantum gases. Theoretical approaches are presented and recent experimental results are discussed.

Chapter 3: Impurity dynamics and polaron formation
The experimental procedure and interferometric sequence for measuring impurity dynamics in a BEC are introduced. Subsequently, two publications are presented, which observe initial dynamics and eventual formation of the Bose polaron.

Chapter 4: Energy and timescales of the polaron
Spectroscopic and interferometric approaches to investigate the Bose polaron are introduced and compared. Furthermore, impurity dynamics at repulsive interaction strengths, the polaronic energy and the timescales of the polaron are discussed. A publication is presented, which analyzes these concepts in greater detail.

Chapter 5: Observation of bipolarons
Effective interactions between polarons forming the bipolaron are introduced, and an experimental procedure to investigate this is discussed. A physically motivated model is then constructed and compared with experimental data yielding experimental evidence of bipolarons in a BEC. The dynamical formation is resolved and the bipolaron energy is observed for a range of attractive interaction strengths. Finally, the quasiparticle residue of the polaron is measured.

Chapter 6: Conclusion and outlook
The thesis concludes by summarizing key results and providing an outlook for future work.

CHAPTER 2

POLARONS IN QUANTUM GASES

The concept of impurities interacting with a surrounding medium is widely studied in many areas of physics. The impurity and its excitations of the medium can be described as a quasiparticle known as a Fermi or a Bose polaron depending on the quantum statistics of the medium. In this chapter models of such polarons are examined before experimental results are discussed.

The chapter is structured as follows. First, key properties of bosonic quantum gases are introduced in Sec. 2.1 and interactions between ultracold atoms are considered. In Sec. 2.2 the history of the polaron as a theoretical concept is presented from initial idea by Landau and Pekar to recent theoretical models of polarons in ultracold gases. This is followed by a discussion of experimental studies of the Fermi polaron in Sec. 2.3 and, finally, of the Bose polaron in Sec. 2.4. This constitutes a comprehensive background for the dynamical investigations of the Bose polaron in the following chapters.

2.1 Properties of Bose-Einstein condensates

The special phenomenon of Bose-Einstein condensation describes a macroscopic population accumulating in the ground state of a quantum system. This is possible for particles known as bosons, whereas fermions can never occupy the same quantum state. The behavior of bosons was first considered in 1924 when Bose published a derivation of Planck's radiation law using massless, indistinguishable particles [9]. This was later extended to particles of mass by Einstein, and he realised that bosons condense into a single quantum state below a critical temperature [10]. In this section, the physics of BECs are briefly reviewed and interactions between ultracold atoms are examined following the theoretical introduction in Ref. [39].

2.1.1 Condensation of bosons

Generally, a gas of thermal atoms can be described classically by the Maxwell-Boltzmann distribution of states. However, when cooling the atoms their wave functions expand revealing their inherent quantum nature. In the regime of ultralow temperatures, it is therefore important to use the correct distribution function. For non-interacting bosons, the average number of particles in a quantum state ν is thus given by the Bose distribution

$$f(\epsilon_\nu) = \frac{1}{e^{(\epsilon_\nu - \mu)/k_\mathrm{B}T} - 1}, \tag{2.1}$$

where k_B is the Boltzmann constant, ϵ_ν is the energy of state ν, μ is the chemical potential and T is the temperature of the gas. This function describes how the bosons are distributed across the possible quantum states of the system.

If the bosonic gas is cooled even further, a critical temperature T_C is reached. This temperature describes a transition into a system, where a macroscopic fraction of the bosons is condensed in a single quantum state being the lowest energy state of the system. For atoms in a three-dimensional harmonic oscillator potential characterized by the trapping frequencies ω_x, ω_y and ω_z, the critical temperature is given as

$$k_\mathrm{B} T_\mathrm{C} = \frac{\hbar\bar{\omega} N^{1/3}}{[\zeta(3)]^{1/3}} \approx 0.94\hbar\bar{\omega} N^{1/3}, \tag{2.2}$$

where $\hbar$ is Planck's reduced constant, N is the number of particles, ζ is the Riemann zeta function and $\bar{\omega} = (\omega_x \omega_y \omega_z)^{1/3}$ is the geometric mean of the trapping frequencies. Remarkably, Eq. (2.2) predicts a macroscopic ground state population at temperatures $T \sim T_\mathrm{C}$, where the corresponding energy is still higher than the energy spacing of the harmonic oscillator $k_\mathrm{B} T_\mathrm{C} \approx 0.94\hbar\bar{\omega} N^{1/3} \gg \hbar\bar{\omega}$.

Below the critical temperature, a large fraction of the atoms accumulates in the ground state. The fraction of condensed bosons N_0 relative to the total number N is determined by

$$\frac{N_0}{N} = 1 - \left(\frac{T}{T_\mathrm{C}}\right)^3. \tag{2.3}$$

This simple relation derived for an ideal Bose gas is useful to predict the expected condensate fraction at a given temperature. For precise calculations, small corrections are required, which include effects due to finite particle number and interactions between the atoms [40]. However, for most applications Eq. (2.3) provides a good estimate of the population in the ground state.

2.1.2 Interactions between ultracold atoms

Interactions between atoms are in general complicated to describe especially for intricate many-body systems. However, in dilute ultracold gases the low densities n allow using simplified models. Since the atoms are far apart, the interparticle distance is often much larger than length scales associated with atom-atom interactions. In this regime, it is therefore sufficient to use two-body models and neglect higher-order interactions when describing the atomic interactions .

A central concept for two-body interactions is the scattering length a. Using the formalism of partial wave theory, this parameter expresses the effects of s-wave scattering events which, for low temperatures, dominate the interactions. The physical implications of a can be motivated by considering the cross section σ of two distinguishable particles with a spherical symmetric interaction. For elastic scattering with wave number k, the low-energy limit of σ is then given as

$$\lim_{k\to 0} \sigma = 4\pi a^2. \tag{2.4}$$

The scattering cross section at low temperatures is thus fully described by a single parameter a, which may in some sense be interpreted as the length at which the two particles see each other.

Interactions between atoms also lead to losses in a trapped ultracold cloud. In particular, it is possible for three atoms to be lost in a so-called three-body recombination event. Here, a deeply bound dimer is created and the excess energy is distributed between the dimer and the remaining atom, which allows all three atoms to escape the trap. Furthermore, depending on the exact states of the atoms, two-body inelastic losses are possible. These occur if two atoms in a spin-exchange process can decay into other spin states and gain energy thus enabling them to leave the trap.

The ability to control both the magnitude and the sign of the scattering length, between the constituents of an ultracold gas, is essential for many investigations. This is possible due to Feshbach resonances, which can be used to tune the interaction between two atoms. Specifically, the effects of elastic scattering in a certain open channel may be dramatically altered, if a bound state of a closed channel is energetically close by [28]. For an ultracold gas, the states involved in such processes are often atomic hyperfine states exhibiting different magnetic moments. Due to the Zeeman effect, it is therefore possible to apply a magnetic field B, which then controls the energetic difference between the states and thus the scattering length of the interaction. Close to a Feshbach resonance the scattering length may be expressed as

$$a(B) = a_{\mathrm{bg}}\left(1 - \frac{\Delta B}{B - B_0}\right), \tag{2.5}$$

where ΔB is the width of the resonance and B_0 is the position of the resonance center. This simple relation shows that it is possible to tune the magnitude of the scattering length a through the applied magnetic field B. Furthermore, Eq. (2.5) reveals the accessibility of both negative and positive scattering length resulting in attractive and repulsive interactions, respectively.

For the atomic species of ^{39}K investigated in this thesis, many hyperfine intrastate and interstate Feshbach resonances have been predicted theoretically [41]. However in this thesis, the focus will be on scattering lengths characterizing internal scattering in the $|F = 1, m_F = -1\rangle$ state and scattering with the $|F = 1, m_F = 0\rangle$ state, which are denoted a_{B} and a, respectively. The scattering lengths of these states and their Feshbach resonances have also recently been studied experimentally [42]. Both scattering lengths are shown in Fig. 2.1 and clearly display resonant behavior at certain magnetic fields. Importantly, there exists an interval where a_{B} is positive and constant while a resonance is present in a. This allows experiments in this region to be conducted with tunable interstate interactions and with an unchanged scattering length for interactions between atoms in the $|F = 1, m_F = -1\rangle$ state.

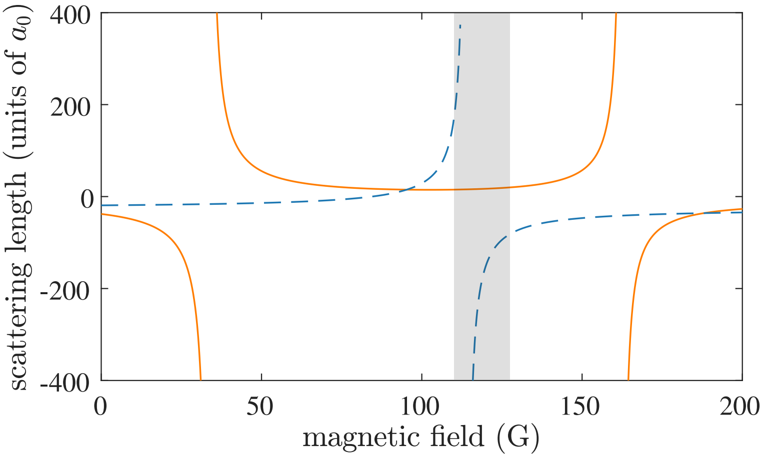

Figure 2.1: Scattering lengths and Feshbach resonances for two states in ^{39}K [41]. The scattering length of internal interactions in the $|F = 1, m_F = -1\rangle$ state is shown as a solid orange line and the scattering length for interactions with the $|F = 1, m_F = 0\rangle$ state is shown as a dashed blue line. The shaded grey region indicates the region of magnetic fields investigated in this thesis.

2.1.3 The Gross-Pitaevskii equation

It is important to consider the influence of interatomic interactions on the physics of a BEC. Qualitatively, repulsive interactions between bosons are expected to increase the size of the condensate relative to the size of a non-interacting BEC. Correspondingly, a condensate with attractive interactions is expected to be smaller or even unstable to collapse. Indeed such a collapse, known as a bosenova, has been observed experimentally [43].

To describe a BEC containing interactions, a Schrödinger-like equation is presented and discussed in the following. This is known as the

Gross-Pitaevskii equation and is valid for weak interactions in the condensate. The criterion can be characterized using the gas parameter na^3 that must fulfil $na^3 \ll 1$ corresponding to the interparticle spacing $n^{-1/3}$ being much larger than the scattering length. In this regime, the interactions are well-described by two-body interactions as previously discussed. The scattering between two atoms of equal mass m and at positions $\mathbf{r}$ and $\mathbf{r'}$ is therefore modelled by a contact potential $U_0\delta(\mathbf{r}-\mathbf{r'})$. Here, the coupling constant $U_0 = 4\pi\hbar^2 a/m$ and δ denotes the Dirac delta potential.

For a BEC held in an external trapping potential $V(\mathbf{r})$ at temperature $T = 0$, all the atoms are condensed in the same single-particle quantum state $\phi(\mathbf{r})$. A condensate wave function is therefore defined as $\psi(\mathbf{r}) = N^{1/2}\phi(\mathbf{r})$. It is then possible to write the following wave equation

$$-\frac{\hbar^2}{2m}\nabla^2\psi(\mathbf{r}) + V(\mathbf{r})\psi(\mathbf{r}) + U_0|\psi(\mathbf{r})|^2\psi(\mathbf{r}) = \mu\psi(\mathbf{r}). \tag{2.6}$$

This is the Gross-Pitaevskii equation, which has the same overall form as the familiar Schrödinger equation. However, it differs by containing a non-linear term $U_0|\psi(\mathbf{r})|^2$ and moreover by having the chemical potential μ as the eigenvalue of the equation.

For sufficiently large condensates at repulsive interactions, the contribution from the kinetic energy is negligible. This is known as the Thomas-Fermi approximation and is often realized experimentally. Rearranging the terms of Eq. (2.6), it is then possible to determine the density as

$$n(\mathbf{r}) = |\psi(\mathbf{r})|^2 = \frac{\mu - V(\mathbf{r})}{U_0}. \tag{2.7}$$

At the boundaries of the cloud, where the density approaches zero, one obtains $V(\mathbf{r}) = \mu$. This can be used to calculate the spatial extension of the cloud. For a harmonic potential characterized by the trapping frequencies ω_i where $i = x, y, z$, the three semi-axes are thus given as

$$R_i^2 = \frac{2\mu}{m\omega_i^2}. \tag{2.8}$$

This parameter is also known as the Thomas-Fermi radius. It can furthermore be used to calculate the density profile as $n(\mathbf{r}) \propto \sum_{i=1}^{3}(1 - r_i^2/R_i^2)$ for $0 \leq r \leq R$, which results in a distinctive parabolic shape of the condensate.

This concludes the brief review of condensates and interacting atoms. Importantly, at ultralow temperatures bosons may condense into the lowest energy state of a system thus forming a BEC. The interactions between the atoms can be characterized by the scattering length a, and a Schrödinger-like wave equation was introduced to describe a weakly interacting condensate. This section was primarily concerned with bosons and BECs. For fermions, a similar condensation of particles into a single quantum state is not possible due to the Pauli exclusion principle. However, it is possible to cool a Fermi gas to quantum degeneracy corresponding to a macroscopic occupation of quantum states below the Fermi energy. Implications of this are further elaborated in Sec. 2.3.

2.2 Theoretical descriptions of polarons

Interacting impurities and the notion of polarons have been the center of substantial theoretical efforts. The explored models have applications for many physical systems and have recently been realized in the context of ultracold quantum gases. In this section, the history of the polaron from initial conception to recent theoretical methods is outlined. It is not the aim to develop a complete framework but merely to motivate the physical implications of polarons following the works of Refs. [44, 45].

2.2.1 History of the polaron

The polaron was originally studied by Landau and Pekar in the middle of the previous century, when they considered the motion of electrons in a crystal [25]. The negatively charged electrons couple to the vibrations of the positively charged ions, and a central concept is therefore the electron-phonon interaction (EPI). For a continuous polarizable medium, this results in a polaron with a large wave function propagating through a solid similarly to a free electron but with an increased effective mass.

In 1954, Fröhlich expanded the previous work by applying second quantization to the EPI [46]. The model was developed in the weak coupling regime of interactions between electrons and phonons. This criterion may be quantified using the dimensionless coupling constant $\alpha = (e^2/\kappa)\sqrt{m/2\omega_0}$, given by the elementary charge e, electron mass m, phonon frequency ω_0 and the high-frequency and static dielectric constants, ε and ε_0, through $\kappa = (\varepsilon^{-1} - \varepsilon_0^{-1})^{-1}$. The weak coupling regime is then characterized by $\alpha < 1$. For a medium of volume V, the relevant term of the Hamiltonian can in this regime be written as [44]

$$H_{\text{EPI}} = \sum_{\mathbf{q}} \frac{M}{q\sqrt{V}} \rho(\mathbf{q})(a_{\mathbf{q}} + a^{\dagger}_{-\mathbf{q}}), \tag{2.9}$$

where $\rho(\mathbf{q})$ is the electron density operator and $a^{\dagger}_{\mathbf{q}}$ ($a_{\mathbf{q}}$) is the creation (annihilation) operator of a phonon with momentum $\mathbf{q}$. The matrix element M can be attributed to dielectric screening effects due to phonons and is given as $M^2 = 2\pi e^2 \hbar\omega_0 \kappa^{-1}$.

Several interesting properties can be calculated using perturbation theory to solve this weak coupling model. For a slow electron of momentum $\mathbf{k}$, the second-order energy $\tilde{E}_{\mathbf{k}}$ is given as

$$\tilde{E}_{\mathbf{k}} = -\alpha\omega_0 + \frac{k^2}{2m^*}, \tag{2.10}$$

where the first term is the polaron binding energy $\alpha\omega_0$ and the second term contains the effective mass $m^* \sim m(1+\alpha/6)$. This increase in mass is the result of virtual phonons being dragged along with the electron. For the polaron at rest, the number of virtual phonons can be found to be $N_{\text{ph}} = \alpha/2$, which reveals the physical implications of the coupling constant α [45].

These results of the Fröhlich model thus predict that a stronger coupling constant α leads to a larger binding energy and an enhanced effective mass of the polaron. In the following, polarons in quantum gases are discussed. Here, the polaronic shift in energy is found to increase in size for stronger interactions between the impurity and the medium similarly to the behavior of the energy in the Fröhlich model. Furthermore, the quasiparticle residue is introduced, which quantifies how much interactions change the impurity comparable to the effective mass considered here.

2.2.2 Models of polarons in ultracold gases

In recent decades, both theoretical and experimental studies have been conducted in the settings of ultracold quantum gases. Generally, these permit quantum engineering of systems with precise control over such parameters as geometry and interactions. Ultracold gases are therefore an ideal candidate for quantum simulations [20].

The notion of quantum simulation refers to an adaptable and controllable physical environment mimicking a complicated system. For the scenario of a polaron, this includes imitating the interactions between the impurity and the medium. This can be achieved by placing an impurity in a BEC, which then closely resemble the solid-state polaron as the medium in both cases is bosonic. This parallel is shown in Fig. 2.2 displaying a polaron being formed by an electron coupling to the lattice phonons (Fig. 2.2(a)) and an impurity dressing a surrounding quantum degenerate Bose gas (Fig. 2.2(b)).

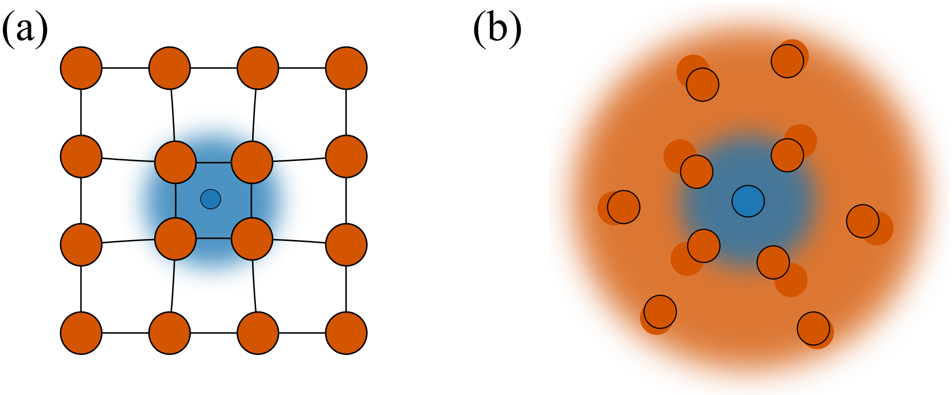

Figure 2.2: Illustration of the polaron in a crystal lattice and in a bosonic quantum gas. (a) The electron in a crystal distorts the medium and couples to the lattice phonons. (b) The impurity in a BEC interacts with the atomic cloud and dresses the surrounding medium bosons.

Numerous theoretical models have been developed to study polarons in quantum gases. Recently, investigations have expanded the Fröhlich model to include important interaction terms [47–49]. The part of the Hamiltonian responsible for interactions between the impurity and the medium is here written as

$$H_{\mathrm{I}} = \frac{1}{V}\sum_{\mathbf{k},\mathbf{k}',\mathbf{q}} V_{\mathrm{I}}(q)\, c^{\dagger}_{\mathbf{k}+\mathbf{q}} a^{\dagger}_{\mathbf{k}'-\mathbf{q}} a_{\mathbf{k}'} c_{\mathbf{k}}, \tag{2.11}$$

where $c^{\dagger}_{\mathbf{k}}$ and $a^{\dagger}_{\mathbf{k}}$ respectively creates an impurity and a boson with momentum $\mathbf{k}$ and V is the system volume. The interaction potential $V_{\mathrm{I}}(q)$ between the impurity and the medium is assumed to be short-ranged. It can be expressed using the impurity-medium scattering length a as $V_{\mathrm{I}}(q) = 2\pi\hbar^2 a/m_{\mathrm{r}}$, where $m_{\mathrm{r}} = m_{\mathrm{I}} m/(m_{\mathrm{I}} + m)$ is the reduced mass of the system consisting of impurity atoms with mass m_I and medium atoms with mass m.

Different theoretical approaches have been used to solve the Hamiltonian of the system. These models include a perturbative analysis [49], variational calculations [48, 50, 51] and quantum Monte Carlo simulations [52, 53] to name a few. For the investigations of the polaron in this thesis, a diagrammatic description is often employed. This model uses a ladder approximation in order to describe the interactions. After being developed for the Bose polaron [47], it has subsequently been compared with experimental observations obtaining good agreement [54]. Furthermore, the model has been used to investigate a temperature dependence of the polaron [55], to calculate effective interactions between polarons [56] and to predict the existence of Bose bipolarons [57].

2.2.3 Energy and quasiparticle residue of the polaron

Generally, interactions between the impurity and the medium lead to the formation of a polaron containing a ground state and a continuum of scattering states. For the spectral response of the impurity, this corresponds to a polaron peak and a tail of excited states. In the following, two fundamental parameters of this polaron peak are discussed.

To characterize the ground state of the polaron, it is imperative to calculate the energetic location of the polaron peak E_P and the spectral weight of the peak Z_P called the quasiparticle residue. The former describes the energy shift of the polaron branch due to impurity-medium interactions, and the latter qualitatively describes how similar a polaron and a non-interacting impurity are. It can be calculated as the squared overlap $Z_\mathrm{P} = |\langle\psi_0|\psi_\mathrm{pol}\rangle|^2$ between the polaron state $|\psi_\mathrm{pol}\rangle$ and the non-interacting impurity state $|\psi_0\rangle$. The residue Z_P therefore ranges from 0 to 1, where the latter reflects zero interactions. The polaron energy and residue are frequently shown as a function of the inverse interaction strength $1/k_n a$. Here, the characteristic wave number of the system

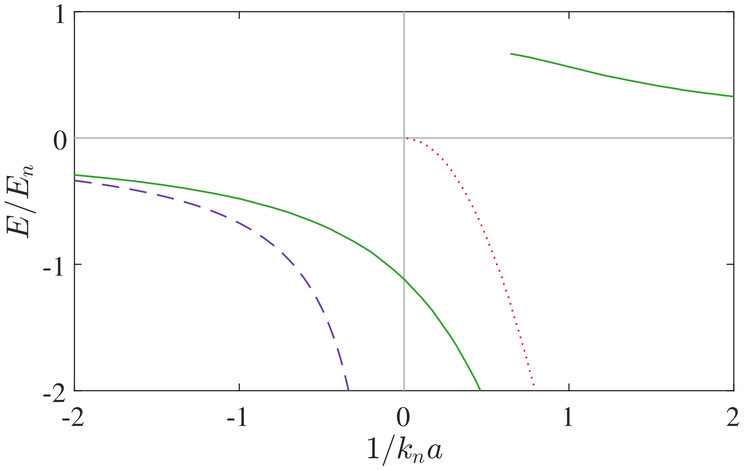

Figure 2.3: Energy of the Bose polaron. A diagrammatic prediction [54] is shown as a solid green line and the mean-field energy at attractive interaction strengths is shown as a dashed purple line. The molecular energy is shown as a dotted red line.

$k_n = (6\pi^2 n_\mathrm{B})^{1/3}$ is given by the density of the medium n_B. Furthermore, the energy spectrum is often scaled by the interaction independent energy of the system $E_n = \hbar^2 k_n^2 / 2m$.

Figure 2.3 shows the diagrammatically predicted polaron energy as a function of the inverse interaction strength [54]. This reveals an attractive polaron branch at negative interaction strengths and a repulsive polaron branch at positive interaction strengths. The energy shift of both branches generally increases as the resonance is approached. For the attractive branch this follows the expectation that an increase in interaction strength leads to deeper bound polarons.

The attractive mean-field energy is also shown in Fig. 2.3. This is given as $2\pi\hbar^2 n_\mathrm{B} a / m_\mathrm{r}$ and is one of the simplest ways of including interactions in a model through an average potential felt by the impurities. At weak interaction strengths, the mean-field energy agrees with the diagrammatic predicted energy. However, the mean-field energy increasingly diverges as the resonance is approached indicating that the simple model is here insufficient for describing the system. Figure. 2.3 additionally shows the molecular energy $\hbar^2/2m_\mathrm{r}a^2$. Remarkably, the attractive polaron branch crosses the resonance and approaches this energy. This behavior can qualitatively be understood by regarding the molecule as the extreme case of an impurity interacting attractively with the medium thereby forming a bound state of the impurity and a medium atom.

The diagrammatic predicted quasiparticle residue is shown in Fig. 2.4 for the attractive polaron branch. At weak interaction strengths, the residue is close to 1 but decreases as the resonance is approached. Besides the polaron peak with amplitude Z_P, the spectral response of the polaron also contains a continuum of excited states. The decrease of Z_P therefore reflects how spectral weight is increasingly distributed from the polaron peak to the continuum. This redistribution is analogous to the enhanced effective mass of the polaron at stronger couplings as predicted by the Fröhlich model.

The behavior of the residue can be motivated by considering how much interactions affect the system. To quantify this, the relative size of the scattering length compared to the interparticle spacing $n_\mathrm{B}^{-1/3}$ can be examined. However, the scattering length diverges close to the resonance and no longer sufficiently characterizes the interactions in this regime. The effective scattering length is therefore defined as $1/|a_\mathrm{eff}| = 1/|a| + 1/n_\mathrm{B}^{-1/3}$ [54]. At weak interaction strengths, $|a_\mathrm{eff}|$ is equal to the absolute value of the scattering length, whereas it yields the interparticle separation in the density-limited regime of unitary interactions [58]. Using the effective scattering length, the fraction $|a_\mathrm{eff}|/n_\mathrm{B}^{-1/3}$ is thus examined, which gives a dimensionless interaction parameter $|a_\mathrm{eff}|/n_\mathrm{B}^{-1/3} = |a|/(|a| + n_\mathrm{B}^{-1/3})$. This yields the value ~ 0 at weak interactions and 1 at unitary interactions. The fraction $|a_\mathrm{eff}|/n_\mathrm{B}^{-1/3}$ therefore qualitatively rep-

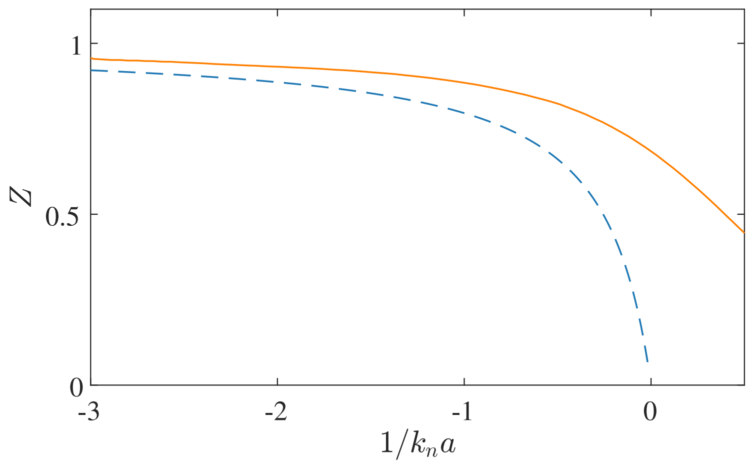

Figure 2.4: Residue of the Bose polaron. A diagrammatic prediction for the attractive polaron branch [55] is shown as a solid orange line and a simple model (see text) is shown as a dashed blue line.

resents how much interactions perturb the system. In a simple picture, this can naively be used to characterize the increased spectral weight of the continuum of excited states. Since the total spectral function is normalized to one, the parameter $1-|a_{\text{eff}}|/n_{\text{B}}^{-1/3}$ is consequently used to describe the amplitude of the polaron peak and its corresponding decrease of spectral weight. Thus, the quasiparticle residue is expressed as $Z_{\text{P}} \sim 1-|a|/(|a|+n_{\text{B}}^{-1/3})$, where a value of 1 describes a non-interacting impurity.

This simple model is also shown in Fig. 2.4 and displays a slow decrease of Z_{P} at weak interaction strengths in qualitative agreement with the diagrammatic description. However, close to the resonance the estimated residue diverges and approaches 0 too fast, which indicates its limited applicability. Nonetheless, the simple model has showed how an increase in interaction strength corresponds to a redistribution of spectral weight from the polaron peak to the continuum of excited states.

The polaron energy and its residue have thus been discussed through the results of a diagrammatic model. This description predicts an attractive and a repulsive polaron branch exhibiting an increasing energy shift with increasing interaction strengths. Furthermore, the attractive polaron branch reveals a decreasing quasiparticle residue when nearing the resonance.

2.3 Experimental investigations of the Fermi polaron

Ultracold gases have proven to be a great experimental setting for studying polarons due to their high degree of purity, tunable interactions and flexibility of trapping geometries. Significant experimental efforts led to the first study of a polaron in an ultracold gas in 2009, where a ^{6}Li Fermi gas was used as the medium [29], and subsequently followed numerous investigations elucidating the properties of the Fermi polaron. In this section, the Fermi polaron, selected experimental studies and their results are briefly reviewed.

Generally, an impurity immersed in a Fermi gas differs from the bosonic scenario due to the quantum statistics of the medium. A Fermi gas obeys the counting statistic of a Fermi-Dirac distribution, and at $T = 0$ this results in a unity filling of each quantum state below the Fermi energy E_F. The Fermi polaron therefore realizes a different setting than the canonical example of an electron moving through a crystal and coupling to a bosonic medium of lattice phonons. Instead, it is an excellent platform for investigating Landau's theory of Fermi liquids [59] and the Kondo effect [60].

2.3.1 Spectroscopic observations

The first observation of the Fermi polaron was realized using radio-frequency (rf) spectroscopy to measure the spectral response of the Fermi polaron at attractive interaction strengths [29]. These results were later complemented by similar rf investigations of both the attractive and repulsive polaron in two-dimensional and three-dimensional Fermi gases [30–34].

Common for these studies is the use of two impurities states, where one is interacting with the surrounding medium and the other is not. Due to the presence of the medium, the energy of the interacting impurity state is therefore shifted with a certain detuning as compared to the atomic state. This detuning can be extracted as a function of interaction strength by measuring the transition frequency between the interacting and non-interacting impurity state. This approach exactly corresponds to mapping the polaron energy across the resonance, which was used to measure and identify the attractive and repulsive polaron branch.

Radio-frequency spectroscopy has also been employed to measure the quasiparticle residue Z_P of the Fermi polaron. In Ref. [29] the residue was obtained from the amplitude of the polaron peak and displayed a decrease as the interaction strength was increased from weakly attractive towards the unitary regime. In Refs. [30, 32, 34] the residue was extracted by driving Rabi oscillations between the polaron state and a non-interacting impurity state. The measured residue revealed similarly decreasing behavior for increasing interaction strength and was furthermore compared with theoretical predictions obtaining good agreement.

2.3.2 Interferometric observations

An excellent tool for measuring dynamical properties of the polaron is interferometric investigations. These permit observing the evolution of the impurity on the timescale given by the Fermi energy as $t_\mathrm{F} = \hbar/E_\mathrm{F}$.

Similarly to rf spectroscopic approaches, a non-interacting and an interacting impurity state is used. Furthermore, these experiments typically employ a two-pulse Ramsey scheme with a variable evolution time in between. This allows measuring a complex-valued Ramsey signal $S(t) = |S(t)|e^{-i\varphi(t)}$, where the contrast $|S(t)|$ describes decoherence due to scattering events and the phase $\varphi(t)$ is governed by the polaron energy in the limit of long evolution times. The interferometric sequence thus permits observations of both initial impurity dynamics and subsequent formation of the polaron. The technical details of such Ramsey schemes are further elaborated in Sec. 3.3.

While an initial dynamical study of the Fermi polaron investigated breathing modes of an impurity component [61], it was using interferometric techniques that polaron formation in real time was first observed [35, 36]. At weak interaction strengths, a transient parabolic behavior of the contrast revealed initial two-body impurity dynamics. For longer times, an exponential decay of the contrast and a linear phase evolution instead reflected the quasiparticle properties of the polaron. At resonant interactions, the observed Ramsey signal was distinctively different and $|S(t)|$ displayed oscillatory behavior. This indicated the presence of two polaron states resulting in the Ramsey signal exhibiting a quantum beat. At all interaction strengths, the observed dynamics was furthermore in agreement with theoretical predictions, thus consolidating the understanding of the Fermi polaron.

2.4 Experimental investigations of the Bose polaron

The Bose polaron closely resembles the solid-state polaron pioneered by Landau and Pekar. In both scenarios, the medium is composed of bosons with similar dispersion relations. Furthermore, Bose polarons are important for understanding central effects in novel technologies such as electronic transport in organic transistors [26] and even high-temperature superconductivity [27]. However, due to the possibility of three-body collisions in BECs, the lifetime of the Bose polaron is shorter than the corresponding lifetime of the Fermi polaron. This inherently complicates the experimental realization of polarons in a BEC.

Following the first observation of the Fermi polaron in 2009, several investigations were conducted with impurities in Bose gases. These include single impurities in an uncondensed Bose gas [62], impurities in a one-dimensional Bose gas [63], charged impurities in a BEC [64–66] and impurities confined by a species-selective potential immersed in a BEC [67, 68]. However, it was not until 2016 that two independent studies realized the generic, mobile impurity in a BEC [37, 38], which most closely resemble the canonical polaron. Subsequently, the Rydberg polaron in a BEC has also been observed [69]. This features the novel ability of multiple medium atoms forming molecular bonds with the polaron.

The first two investigations of the mobile Bose polaron were conducted using rf spectroscopy [37, 38] similarly to the observations of the Fermi polaron [29–31]. Using a non-interacting and an interacting impurity state, the two studies measured the rf response of transferring impurities into the polaron state. This is known as *injection* spectroscopy, and the energy spectrum clearly revealed an attractive and a repulsive polaron branch. In a following paper, the polaron energy was extracted by fitting a physically motivated line shape function to the data [54]. The polaron energy was furthermore compared with quantum Monte Carlo simulations and a diagrammatic calculation, and excellent agreement was obtained with both models.

Recently, the Bose polaron was investigated using *ejection* spectroscopy [70]. This measures the spectral response of transferring impurities from the interacting impurity state to a non-interacting state. Using this method, it is possible to prepare equilibrated polarons before probing them. The study revealed an intriguing polaronic temperature dependence and furthermore measured the short-range correlations of the polaron.

These spectroscopic studies have provided clear experimental evidence of the Bose polaron at both attractive and repulsive interaction strengths. However, important aspects of the polaron still remain unresolved. Similarly to the Fermi polaron, the impurity dynamics is expected to occur on the timescale $t_n = \hbar/E_n$ set by the system energy E_n. However, the formation of the Bose polaron has not yet been observed. Furthermore, it is of interest to measure the quasiparticle residue as well as induced polaron-polaron interactions that may expand the understanding of the Bose polaron. The experimental investigations of these properties are the focus of the remainder of this thesis.

CHAPTER 3

IMPURITY DYNAMICS AND POLARON FORMATION

Impurities interacting with a surrounding medium form quasiparticles known as polarons. The formation dynamics of polarons is highly nontrivial and connects initial few-body scattering with later many-body correlations. Such dynamical evolution has previously been measured in a Fermi gas, as discussed in Sec. 2.3, but has so far remained experimentally elusive for the Bose polaron.

In this chapter, experimental observations of impurity dynamics in Bose-Einstein condensates are presented and compared with theoretical predictions. The chapter is structured as follows. First, the central concept of impurity coherence is introduced in Sec. 3.1. Then, the experimental procedure for realizing BECs in the laboratory is briefly presented in Sec. 3.2. This is in Sec. 3.3 followed by a discussion of the employed interferometric sequence and some of the experimental challenges. In Sec. 3.4, theoretical descriptions of the impurity evolution are introduced. Finally, in Sec. 3.5 and Sec. 3.6 the results and perspectives of two publications, constituting the first observations of impurity dynamics in a BEC, are discussed and my contributions clarified, before each publication is presented.

3.1 Impurity coherence

The study of out-of-equilibrium systems is intriguing, albeit inherently challenging in many solid-state materials due to fast evolution times. However, the low densities of ultracold quantum gases allow such non-equilibrium dynamics to be experimentally investigated [71]. For an interacting impurity that is suddenly immersed in a medium, the subsequent dynamics eventually leads to polaron formation. It is therefore important to explore this evolution to better understand the equilibration processes of the polaron.

To investigate the dynamical evolution of the impurity state, a parameter linking predictions and observations is needed. The coherence function is a reasonable choice of such a parameter, since it can be described theoretically and is experimentally accessible. The coherence $C(t)$ is here defined as the dynamical overlap $C(t) = \langle\psi(0)|\psi(t)\rangle$ between the initial state $|\psi(0)\rangle$ and the time evolved impurity state $|\psi(t)\rangle$. The coherence therefore entails how the system decoheres through scattering processes between the impurity state and the medium state. In Sec. 3.3, the experimental extraction of the coherence using a Ramsey-like sequence is explained, and in Sec. 3.4 two theoretical methods for predicting the coherence are discussed.

3.2 Production of BECs

In the following section, the initial procedure leading to the production of BECs is discussed. Generally, the experiment is capable of working with mixtures of ^{87}Rb and ^{39}K or ^{41}K [72]. However, the work presented in this thesis only investigates impurity dynamics in ^{39}K BECs. The apparatus and techniques have previously been explained in great detail [73–75] and only central parts of the experimental sequence are reviewed here.

Initially, rubidium and potassium atoms are captured from a background vapor and cooled in a dual magneto-optical trap (dual MOT). Here, detuned cooling light and repumper light are for both species applied to the $|F = 2\rangle \rightarrow |F' = 3\rangle$ and $|F = 1\rangle \rightarrow |F' = 2\rangle$ transitions, respectively, where the prime denotes excited states. To reduce destructive light-assisted collisions between rubidium and potassium atoms in the cooling cycle, a dark spontaneous optical force trap (dark-SPOT) is employed [76, 77]. This is achieved by placing a small opaque disk in the center of the Rb repumper laser beam. A dark-SPOT thus permits accumulation of cold rubidium atoms in the dark $|F = 1\rangle$ state in the center of the trap, where the repumper light is consequently blocked. To enhance population in this state, additional depumper light is applied resonantly with the $|F = 2\rangle \rightarrow |F' = 2\rangle$ transition for Rb, which allows decay into the dark state.

The MOT is typically employed for 25 s. The magnetic field is then turned off and an optical molasses scheme is applied to cool the atoms below the Doppler limit [78, 79]. Subsequently, the MOT coils are turned on again and the atoms are optically pumped to the $|F = 2, m_F = 2\rangle$ state. This is obtained using σ^+ polarized light resonant with the $|F = 2\rangle \rightarrow |F' = 2\rangle$ transition. Thus, the atoms can be trapped by the magnetic field produced by the current in the coils.

At this stage, the atoms are transferred to a vacuum chamber with a lower background pressure. This is achieved by moving the MOT coils, which are located on a transport sleigh. Once the atoms are in this vacuum chamber, they are loaded into a new magnetic quadrupole trap by increasing the current through a stationary set of coils, while the current in the MOT coils is decreased. Subsequently, forced evaporative cooling is performed on the rubidium atoms by applying microwave radiation transferring the hottest atoms to the untrapped $|F=1, m_F=1\rangle$ state. This process also cools the potassium atoms sympathetically due to the spatial overlap of the two clouds. For decreasing temperatures, Majorana spin-flips become increasingly destructive, since the density near the magnetic field zero-point grows. Therefore, a third coil is turned on transforming the quadrupole trapping potential into a quadrupole Ioffe-Pritchard configuration (QUIC) trap [80]. Importantly, a QUIC trap features a magnetic field raised slightly above zero at the trap center. The evaporation is then continued until all Rb atoms have been removed.

The background scattering length of ^{39}K is negative, which prohibits the realization of condensates in a magnetic trap. It is therefore necessary to transfer the atoms to an optical dipole trap (ODT) by turning on two intersecting 1064 nm laser beams. By gradually increasing the power in the ODT, the potassium atoms are captured due to the dipole force [81], while the magnetic trap is slowly turned off. Subsequently, the configuration of the coils is changed and a homogeneous magnetic field is applied to the atoms. This allows the use of Feshbach resonances to tune the scattering length between the atoms via the magnetic field [28]. Two rapid adiabatic passages are employed to transfer the atoms to the $|F=1, m_F=-1\rangle$ state. The final evaporative cooling is then performed in the vicinity of an intrastate Feshbach resonance located at 34 G [41] by decreasing the intensity of the laser beams. After a sufficient number of atoms have condensed, the magnetic field is ramped to a target value around 115 G. At this point, typically 5×10^4 BEC atoms are ready for the subsequent Ramsey scheme, which is discussed in the following section.

After the interferometric sequence, the atoms are released from the trap. In a following time-of-flight, they expand for 28 ms, before they are measured using absorption imaging. An example of a typical ^{39}K BEC is

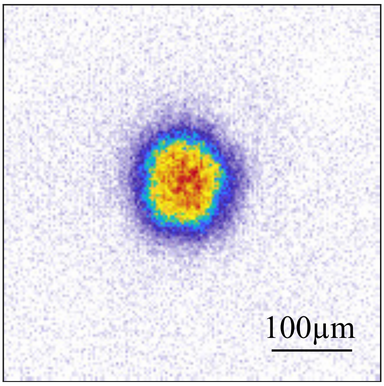

Figure 3.1: An example image of a ^{39}K BEC obtained using absorption imaging after 28 ms time-of-flight. Typically, 5×10^4 BEC atoms are realised in the optical dipole trap before the interferometric sequence.

shown in Fig. 3.1, where the number of BEC atoms can be extracted using bimodal fits.

3.3 Interferometric sequence

Ramsey interferometry is a useful tool to manipulate and investigate quantum states of a system. The original experimental design by Norman Ramsey used the interference signal of two internal states to measure their transition frequency with high precision [82]. This technique has later on been extended to include translational states and is now frequently used in atom interferometry [83]. In this section, the principles behind Ramsey sequences are outlined and their role in recent investigations is considered. Moreover, the modified Ramsey sequence that is employed in the interferometric measurements presented in the following two publications [84, 85] is discussed.

Generally, a Ramsey sequence uses two pulses to probe a two-level system. The scheme is most conveniently described using a Bloch sphere as illustrated in Fig. 3.2(a-c). Here, the two states are represented by either of the two poles and the Bloch vector pointing anywhere else on the sphere represents a superposition of the two states. Since the system starts in a single quantum state, the Bloch vector is initially oriented towards one of the two poles. The first pulse typically creates an equal superposition of the first and second state, and it thus rotates the Bloch vector to the equatorial plane as shown in Fig. 3.2(a). Such a pulse is referred to as a $\pi/2$-pulse. The system then evolves for a variable evolution time. This is shown in Fig. 3.2(b), where the Bloch vector precesses if the frequency of the first pulse is not resonant with the transition frequency between the two states. A second $\pi/2$ pulse with a variable phase then rotates the vector again as shown in Fig. 3.2(c). Finally, the population in each state is measured. By repeating this measurement with different phases of the second pulse, a sinusoidal signal of the spin-population is obtained. This signal is characterized by an amplitude, often referred to as the contrast, and a phase which, in turn, may be used to describe the orientation of the Bloch vector after the variable evolution time.

Recently, this procedure was employed to investigate impurity dynamics in a Fermi gas [35, 36] and the evolution of a unitary thermal Bose gas [86]. In particular, the interferometric sequence was used to observe the evolution of a quantum state driven by interactions with other states in the atomic cloud. This was achieved by applying the sequence to an atomic two-level system with an interacting state and a non-interacting reference state, thus allowing the Ramsey scheme to precisely measure the relative evolution of the two states. Since the probing pulses were chosen to be resonant with the atomic transition frequency, the precession of the Bloch vector in the variable evolution time was only driven by the interactions, which also caused a decay of the contrast. By extracting the evolution of the contrast and the phase, the two studies were able to infer important properties of their respective systems.

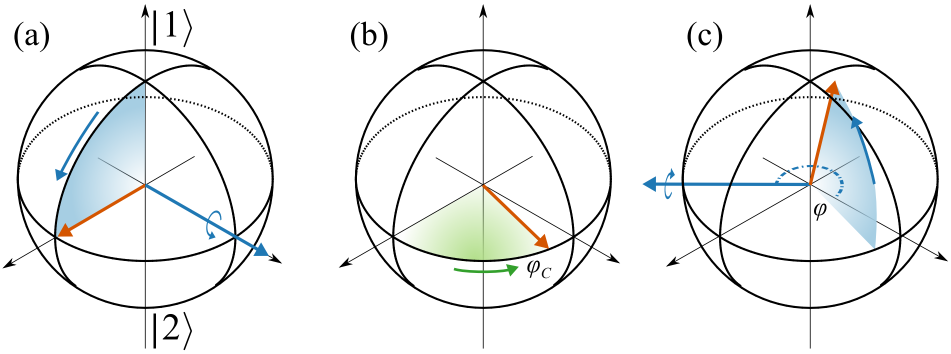

Figure 3.2: A Ramsey sequence illustrated using the Bloch sphere. The north and south pole represents the $|1\rangle$ state and the $|2\rangle$ state, respectively. (a) An initial pulse rotates the Bloch vector away from the $|1\rangle$ state to the equatorial plane and creates an equal superposition of the two states. (b) In a variable evolution time, the Bloch precesses with a phase φ_C due to a detuning of the initial pulse. (c) A second pulse with a variable phase φ rotates the Bloch vector again, whereafter the spin-population is measured. A similar figure was published in Ref. [84].

The interferometric sequence employed in the following publications [84, 85] follows a similar procedure to investigate impurity dynamics in a ^{39}K BEC. Initially, the system is in the $|F = 1, m_F = -1\rangle \equiv |1\rangle$ state and a resonant rf pulse is then used to drive a transition to the $|F = 1, m_F = 0\rangle \equiv |2\rangle$ state. However, since the $|1\rangle$ state is used as the medium state and the $|2\rangle$ state as the impurity state, a $\pi/2$-pulse cannot be employed. This would create an equal mixture of the two states. Instead, the Bloch vector is retained close to the initial state with a short $\pi/7$-pulse as shown in Fig. 3.3(a). This creates an imbalanced mixture corresponding to a small impurity population of ~ 5% in the $|2\rangle$ state. In the subsequent variable hold time t, the evolution of the system is driven

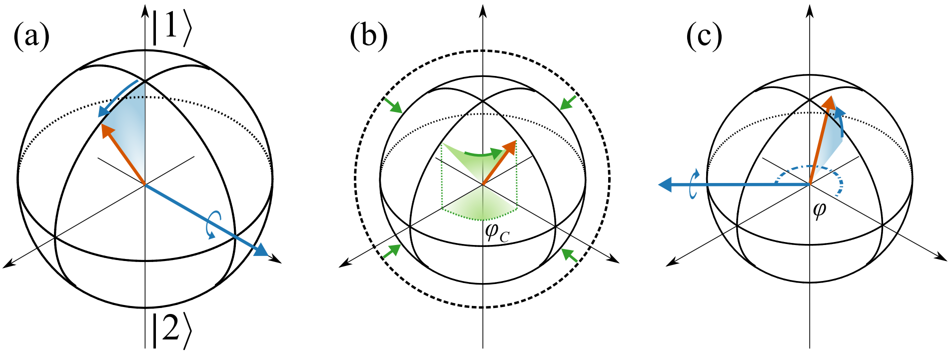

Figure 3.3: The interferometric sequence used in Ref. [84, 85] illustrated using the Bloch sphere. The north and south pole represents the $|F=1, m_F=-1\rangle \equiv |1\rangle$ state and the $|F=1, m_F=0\rangle \equiv |2\rangle$ state in ^{39}K, respectively. (a) First, a short radio-frequency pulse rotates the Bloch vector slightly away from the initial state thus creating a population-imbalanced superposition of the two states. (b) Subsequently, the Bloch vector shrinks and precesses with phase φ_C in a variable evolution time due to interactions between the two states. (c) Finally, a second pulse with a variable phase φ rotates the Bloch vector again. The spin-population is then extracted using absorption imaging. A similar figure was published in Ref. [84].

by interactions between the $|1\rangle$ state and the $|2\rangle$ state. As illustrated in Fig. 3.3(b), this may initially be envisioned as a precession and a shrinking of the Bloch vector. A second $\pi/7$-pulse with a variable phase φ then rotates the vector again, as shown in Fig. 3.3(c), which marks the end of the interferometric sequence.

The interference signal is normally obtained through a measurement of the population in both states after the second pulse. Unfortunately, fast three-body losses in the system at hand prohibit a direct measurement of the final population in the impurity state. Instead, the atoms are held in the ODT for an additionally 2 ms, where two medium atoms are lost for each impurity. Finally, the atoms are released from the trap, and the remaining number of atoms in the medium state is measured after time-of-flight using absorption imaging. This atom number $N(\varphi)$ constitutes the interference signal and varies sinusoidally with the phase φ of the second rf pulse. The function $N(\varphi) = N_0 - \mathscr{A}\cos(\varphi - \varphi_C)$ is therefore fitted to the measured population in the medium state, where the offset N_0 and the sinusoidal amplitude $\mathscr{A}$ and phase φ_C are free parameters. Thus, the coherence amplitude is extracted as $|C(t)| = |\mathscr{A}(t)/\mathscr{A}(0)|$ and the phase as $\varphi_C(t)$ both as a function of the evolution time t.

Using the interferometric sequence, the evolution of the impurity coherence can be measured and consequently compared to theoretical predictions. However, to accurately model the observed impurity dynamics, it is important to identify and incorporate the effects of additional experimental decoherence sources in these predictions. Thus, three decoherence sources are investigated, which include dephasing due to the inhomogeneous density distribution, loss of the impurity during the evolution time and shot-to-shot fluctuations of the magnetic field. To incorporate the effects due to dephasing, the predicted coherence is integrated over the condensate density distribution. The lifetime of the impurity is measured independently and included by multiplying the coherence with an exponential decay. Similarly, the average magnetic field noise is also measured independently at very weak interaction strengths. It is then incorporated by integrating the distribution of phases caused by the fluctuating magnetic field and multiplying the resulting function with the coherence.

An interferometric sequence has thus been introduced and the effects of additional decoherence sources have been considered. This procedure allows the impurity coherence to be experimentally determined, and in the following section two theoretical approaches used to model impurity dynamics are introduced.

3.4 Theoretical description of impurity dynamics

The Bose polaron is generally an intricate quasiparticle consisting of complex many-body correlations between the impurity and the medium. It is often characterized by its quasiparticle residue Z_P and ground state energy E_P as discussed in Sec. 2.2. However, these parameters only describes the polaron peak and its many-body nature. To gain a complete understanding of the quasiparticle it is furthermore necessary to investigate the initial few-body dynamics and the gradual formation of the polaron. In this section, theoretical models of the dynamical evolution is therefore discussed.

The coherence function can be obtained from the spectral function $A(\omega)$ of the impurity. This generally contains a polaron peak and a continuum of excited states and has previously been experimentally investigated using spectroscopic methods [37, 38, 70]. By Fourier transforming the spectral function, the coherence is obtained as

$$C(t) = \frac{1}{2\pi}\int_{-\infty}^{+\infty} A(\omega)e^{-i\omega t}d\omega. \tag{3.1}$$

Thus, the characterization of the impurity in the frequency-domain can be used to describe its dynamical behavior. However, there is no exact solution for the spectral function at arbitrary interaction strength between the impurity and medium. Therefore, the two theoretical predictions used in the following publications [84, 85] either capture only a part of it or rely on approximations to describe the full spectral function.

The initial dynamics is governed by high-frequency two-body scattering between the impurity and the medium. Importantly, the high-frequency tail of the spectral function can be described by an exact solution [87]. An example of this model is shown in Fig. 3.4 as a function of energy. Close to zero the description diverges and yields unphysically values of the spectral function, however, at higher energies it reveals a slow decrease as expected. By Fourier transforming this solution, an expression for the coherence is obtained, which represents the initial two-body dynamics at all attractive interaction strengths. Furthermore, two regimes can be inferred from this expression of the coherence by calculating its limits. These regimes display distinct dynamical behavior with a smooth transition between them, and in the presented papers [84, 85] the two regimes are further elaborated.

Following the initial regimes of two-body dynamics, the evolution is expected to transition into a regime governed by higher-order interactions. Therefore, impurity dynamics at these longer evolution times is now considered. To predict this dynamical behavior, it is necessary to include both the continuum of scattering states and the polaron peak in a model of the spectral function. This can be achieved using a diagrammatic approach to estimate the scattering between the impurity and the medium [47]. Moreover, this method can be employed at both attractive and repulsive interaction strengths. An example of a diagrammatic predicted spectral function is also shown in Fig. 3.4 and clearly displays a polaron peak and a tail of excited states. Importantly, the model recovers the exact solution for high frequencies. In Fig. 3.4, this is reflected by the diagrammatic predicted tail of excited states agreeing with the rigorous two-body description at high energies. The Fourier transform of the diagrammatic model then describes not only the initial dynamics but also a many-body regime at longer evolution times. This regime is further elaborated in the following publication [84] as well.

The investigated theoretical models thus include an exact two-body calculation valid for short-time impurity dynamics and a diagrammatic description capable of prediction the dynamical evolution for longer times. Though only approximate, diagrammatic predictions for the Bose polaron energy have previously been compared to both quantum Monte Carlo and spectroscopic results obtaining excellent agreement [54]. Both models are therefore expected to capture essential parts of the observed

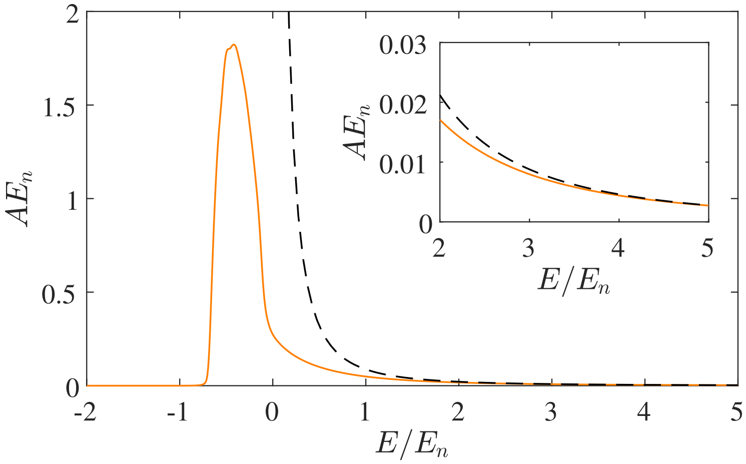

Figure 3.4: Theoretically predicted spectral functions of the polaron at an intermediate interaction strength. An exact solution for the tail of the spectral function due to two-body scattering is shown as a dashed black line [87]. A numerically calculated diagrammatic prediction, which includes the many-body peak of the attractive polaron, is shown as a solid orange line [47, 84]. (Inset) A close up of the tail of the spectral function is shown to highlight the agreement of the two predictions. Both models are used in the following publication [84].

impurity dynamics in the regimes, where they are valid.

3.5 Non-equilibrium quantum dynamics and formation of the Bose polaron

The following paper [84] investigates how a superposition of an impurity state and medium state decoheres leading to the eventual formation of polarons in the system. In the previous sections, the experimental and theoretical methods have been outlined and here, the main results are briefly introduced and discussed before the publication is presented.

3.5.1 Results

The experiment is centered around an interferometric sequence, which employs a two-pulse Ramsey-like scheme to obtain an interference signal. From this signal, the impurity coherence is extracted and in the presented publication [84], the coherence amplitude and phase are shown at three interaction strengths. They are furthermore compared to an exact short-time prediction and a diagrammatic description obtaining excellent agreement with both theories in their respective regime of validity.

The agreement between theory and experimental data highlights how the observed dynamical evolution can be divided into three distinct regimes. First, two-body universal dynamics governs the impurity evolution which, importantly, occurs not only at unitarity. This is followed by two-body weak coupling dynamics, whereafter many-body dynamics dominates the evolution at later times.

Moreover, the transition times between these regimes are extracted from the data. These times are shown in Fig. 1 in the main manuscript together with theoretical predictions. Again, good agreement is obtained between the experimentally extracted transition times and the predicted values. Finally, the instantaneous energy of the impurity at unitarity is obtained from the measured phase evolution, which reveals an equilibration process of the impurity towards the Bose polaron energy.

3.5.2 Outlook

The Bose polaron has previously been investigated using rf spectroscopy [37, 38, 54, 70]. These studies measured the energy spectrum of the polaron, which allowed the polaron branches to be identified.

Good agreement was obtained with theoretical descriptions including variational, diagrammatic and quantum Monte Carlo models. It is therefore important to compare the spectroscopic polaron results with the observations presented in the following publication [84]. Such a detailed analysis is beyond the scope of this section and is instead the main topic of Chap. 4. However, Fig. 4 in the main manuscript does show how the instantaneous energy of the impurity equilibrates towards the previously measured polaron energy [54]. This indicates that the spectroscopic and interferometric approaches are connected in investigating the same quasiparticle.

While this publication [84] constitutes the first observation of impurity dynamics in a BEC, previous experiments have studied the evolution of an impurity in a Fermi gas [35, 36]. These investigations were also conducted using an interferometric sequence and similarly to the results presented in this thesis, they observed distinct dynamical behavior of the impurity evolution and the eventual formation of the polaron. This qualitative agreement between the experimental results of Bose and Fermi polaron studies highlights, how the Ramsey scheme in both scenarios is a successful approach to explore different regimes of impurity dynamics. However, the observed evolutions are not expected to be identical, since the two mediums obey different quantum statistics and exhibit different dispersion relations.

3.5.3 Publication

For the following paper [84], I was part of designing and conducting the experiment. In the main manuscript, I performed all data analysis, created all figures and wrote first drafts of the parts regarding the experimental sequence, the data analysis, the comparison between data and theory, and the corresponding discussion of the results. In the supplementary information, I performed the data analysis and wrote first drafts of the subsections regarding decoherence from the harmonic trap and magnetic field fluctuations, and the sections regarding impurity fraction and experimental data analysis.

The paper was first published in Nature Physics (2021) by Springer Nature and is reproduced with permission from Springer Nature.

nature physics

LETTERS

https://doi.org/10.1038/s41567-021-01184-5

Non-equilibrium quantum dynamics and formation of the Bose polaron

Magnus G. Skou[1]✉, Thomas G. Skov[1], Nils B. Jørgensen[1], Kristian K. Nielsen[1], Arturo Camacho-Guardian[1], Thomas Pohl[1], Georg M. Bruun[1,2] and Jan J. Arlt[1]

Advancing our understanding of non-equilibrium phenomena in quantum many-body systems remains one of the greatest challenges in physics. Here we report on the experimental observation of a paradigmatic many-body problem, namely the non-equilibrium dynamics of a quantum impurity immersed in a bosonic environment[1,2]. We use an interferometric technique to prepare coherent superposition states of atoms in a Bose–Einstein condensate with a small impurity-state component, and monitor the evolution of such quantum superpositions into polaronic quasiparticles. These results offer a systematic picture of polaron formation[3–7] from weak to strong impurity interactions. They reveal three distinct regimes of evolution with dynamical transitions that provide a link between few-body processes and many-body dynamics. Our measurements reveal universal dynamical behaviour in interacting many-body systems and demonstrate new pathways to study non-equilibrium quantum phenomena.

Landau's quasiparticle theory[1] is one of the most powerful concepts with which to understand many-body phenomena. Originally, the theory was developed to describe the interaction of an electron with phonons in a solid, leading to the formation of a quasiparticle[2]. Nowadays it is widely used in many areas of physics and forms the basis for understanding fundamental phenomena such as transport processes, colossal magnetoresistance[8] and superconductivity[9]. Yet, the dynamical processes leading to the formation of quasiparticles has remained elusive in condensed-matter systems because of their high densities and, consequently, fast evolution times. Ultracold quantum gases offer a unique quantum simulation platform[10] to address this problem, as they permit the controlled generation of impurity atoms inside a fermionic[11–19] or bosonic[20–23] quantum gas, where they perturb the surrounding medium to form quasiparticles called polarons. The study of Bose polarons is particularly important because the linear sound dispersion of the Bose–Einstein condensate (BEC) is analogous to that of phonons in crystals, prompting recent theoretical efforts to describe their non-equilibrium evolution[3–7].

In this Letter, we make use of this capability to induce and trace the non-equilibrium dynamics of a quantum impurity from its initial creation to the eventual formation of the Bose polaron. We drive an atomic transition to coherently create a small population of an impurity state in a BEC. Its interaction with the surrounding BEC induces fast quantum evolution, which we probe by monitoring interferometrically the coherence between the initial state $|1\rangle$ of the atoms and the impurity state $|2\rangle$. This, in turn, yields a direct measurement of the time-dependent Green's function of the impurity and thereby allows us to observe the non-equilibrium dynamics of the impurity that leads to the eventual formation of Bose polarons in a BEC.

Our measurements reveal distinct regimes of impurity evolution and thus yield a complete map of its dynamical behaviour, as shown in Fig. 1a. At short times, we observe a universal $\sim t^{3/2}$ decay of the impurity coherence[24] that does not depend on the coupling to the bosonic environment. This behaviour originates in high-energy two-body scattering with the surrounding condensate and governs the initial relaxation. It thus provides a clear experimental signature for such unitarity-limited processes. For weak interactions, an intermediate dynamical regime subsequently emerges. Here, low-energy collisions dominate the dynamical evolution, giving rise to a distinct $\sim t^{1/2}$ decay of the impurity coherence. At longer times, we eventually observe pronounced deviations from such power-law behaviour, reflecting the emergence of many-body correlations that usher in the formation of the Bose polaron. The transitions between these dynamical regimes are shown in Fig. 1a. We observe remarkable agreement between theory and experiment for all impurity interaction strengths and evolution times, providing a quantitative understanding of the non-equilibrium dynamics of this quantum many-body system.

The experiment was performed with Bose–Einstein condensates of ^{39}K atoms in the $|F=1, m_F=-1\rangle \equiv |1\rangle$ hyperfine ground state[25], where F and m_F are the total angular momentum quantum number and its projection, respectively. The average condensate density n_B sets the interaction independent energy scale $E_n = \hbar^2(6\pi^2 n_B)^{2/3}/2m$ of the system and the corresponding timescale $t_n = \hbar/E_n = 4.8\,\mu\text{s}$. Here m is the mass of ^{39}K and the subscript n indicates that the parameter is only density dependent in our experiments. For the controlled population of the impurity state we use a radiofrequency (RF) pulse to drive the transition to the $|F=1, m_F=0\rangle \equiv |2\rangle$ state[20]. The strength of the interaction is characterized by the dimensionless parameter $1/k_n a$, where a is the scattering length for collisions between the impurity and the condensate state, and $k_n = (6\pi^2 n_B)^{1/3}$ is the characteristic wavenumber. We tune the scattering length a by applying a homogeneous magnetic field in the vicinity of a Feshbach resonance at 114 G (refs. [20,26,27]), which does not affect the scattering length a_B for collisions between the condensate atoms.

The interferometric sequence to populate the impurity state and probe its dynamics is illustrated in Fig. 1, showing the evolution of the collective spin on the Bloch sphere[15,28,29]. In this Ramsey-type scheme, we retain the orientation of the Bloch vector close to the initial one, corresponding to a low population of the impurity state. This allows the use of short RF pulses, which can resolve the evolution at times much shorter than t_n.

---

[1] Center for Complex Quantum Systems, Department of Physics and Astronomy, Aarhus University, Aarhus, Denmark. [2] Shenzhen Institute for Quantum Science and Engineering and Department of Physics, Southern University of Science and Technology, Shenzhen, China. ✉e-mail: magnus.skou@phys.au.dk

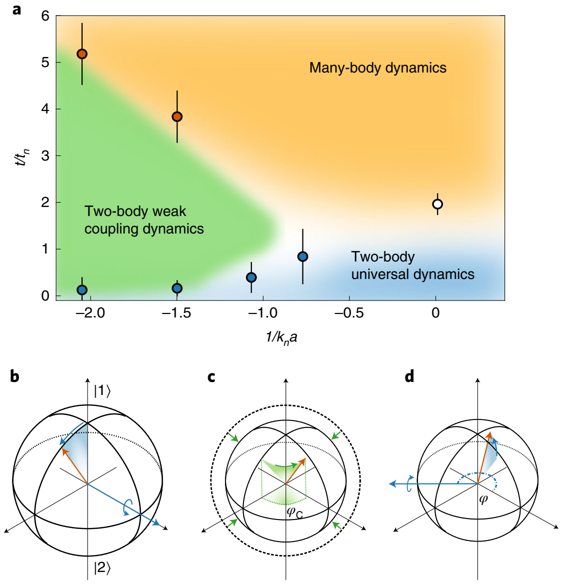

Fig. 1 | Dynamical regimes of impurity evolution and the experimental method. **a**, Characteristic dynamical regimes of impurity evolution as a function of the inverse interaction strength $1/k_n a$ and evolution time t/t_n. The measurements (circles) and theoretical analysis (coloured areas) show three distinct dynamical regimes that extend from ultrafast two-body processes to the many-body regime of polaron formation. The blurring indicates smooth temporal transitions and the error bars correspond to the 1σ confidence intervals of the fitted values (blue) and the data resolution (red and white) (Supplementary Information). **b**–**d**, Interferometric sequence to probe the dynamics illustrated using the collective spin of the atoms on the Bloch sphere. The north pole represents the initial state $|1\rangle$ of the Bose–Einstein condensate and the south pole represents the impurity state $|2\rangle$. A short RF pulse prepares the system in a population-imbalanced collective superposition state (**b**). The subsequent evolution due to the interaction between the impurity state and its bosonic environment gives rise to a phase evolution φ_C and a contraction of the Bloch sphere (**c**). A second pulse with variable phase φ rotates the Bloch vector again (**d**), whereafter the atomic spin population is obtained using an absorptive imaging technique.

The measurement is initiated by applying a RF pulse tuned to the atomic resonance with a duration of 0.5 μs, well below the typical timescales of the subsequent impurity dynamics. As illustrated in Fig. 1b, this coherently generates an admixture of the impurity state with a small population of ~5%. Subsequently, this state evolves for a chosen time t driven by the interaction between the impurity state and the surrounding condensate. Initially, this can be visualized as a rotation and shrinking of the Bloch vector as shown in Fig. 1c. The corresponding dynamics of the impurity state is monitored by closing the interferometric sequence with a second RF pulse with variable phase φ. As shown in Fig. 1d, this second pulse implements a rotation of the Bloch vector around an axis defined by φ. The final spin population is obtained by measuring three-body recombination losses after a 2 ms relaxation time with absorption imaging. This interferometric sequence results in a sinusoidal dependence of the final atom number N on the probe phase φ, as shown in Fig. 2a for various evolution times. We perform a fit $N(\varphi) = N_0 - \mathcal{A}\cos(\varphi - \varphi_C)$ for each evolution time t. Generally, amplitudes can be extracted for longer evolution times even at small signal-to-noise ratio, where the phase determination fails.

Based on these fits, we obtain the normalized coherence function $C(t) = |\mathcal{A}(t)/\mathcal{A}(0)|e^{i\varphi_C(t)}$ (Supplementary Information). This, in turn, is directly proportional to the impurity Green's function $G(t) = -iC(t) = -i\langle\psi_{\mathrm{BEC}}|\hat{c}(t)\hat{c}^\dagger(0)|\psi_{\mathrm{BEC}}\rangle$, where $|\psi_{\mathrm{BEC}}\rangle$ describes the state of the BEC before the first RF pulse and $\hat{c}^\dagger$ is the operator that creates an impurity in the condensate. Consequently, $C(t)$ is directly related to the spectral function of the impurity, which we compute using both a two-body and a many-body description to obtain $C(t)$ throughout the impurity dynamics.

The initial dynamics can be calculated exactly for high energies, where it is determined by two-body physics[30]. A Fourier transform gives the corresponding exact short time dynamics, which has the limiting forms (Supplementary Information)

$$C(t) = \begin{cases} 1 - (1-i)\frac{16}{9\pi^{3/2}}\left(\frac{t}{t_n}\right)^{3/2} & t \ll t_a \\ 1 + \frac{2}{3\pi}(k_n|a|)^3 - iE_{\mathrm{mf}}t/\hbar - (1+i)\left(\frac{t}{t_{\mathrm{w}}}\right)^{1/2} & t \gg t_a \end{cases} \tag{1}$$

where $E_{\mathrm{mf}} = 4\pi\hbar^2 n_{\mathrm{B}} a/m$ is the mean field energy due to impurity state interactions with the BEC and $t_a = ma^2/\hbar$. For times $t \ll t_a$, equation (1) describes universal dynamics where the coherence of the impurity state decays with a power-law exponent of 3/2 on a timescale t_n independent of the (non-zero) interaction strength (Fig. 1a, blue area). This universal short time relaxation directly reflects the unitarity-limited scattering cross-section for short-range interactions, which does not depend on a for collision energies greater than $\hbar^2/ma^2$. Hence, the time t_a marks the crossover (Fig. 1a, blue to green transition) to a regime where the dynamics is governed by the mean field phase evolution $E_{\mathrm{mf}}t/\hbar$, and the coherence decays with a power-law exponent 1/2 on an interaction strength-dependent timescale $t_{\mathrm{w}} = m/32\pi\hbar n_{\mathrm{B}}^2 a^4$ (Fig. 1a, green area). This behaviour arises from weak two-body collisions with a constant cross-section $\sim a^2$ (ref. [5]).

An intuitive understanding of the power laws in equation (1) can be gained from the cross-section $\sigma(k) = 4\pi a^2/(1+(ka)^2)$ assuming that the rate of decoherence is given by the collision rate $\dot{C}(t) \approx -n_{\mathrm{B}}\sigma v$. At a time t after initializing the system, decoherence is caused by coupling to states with $E \approx \hbar/t$ setting the wavenumber $k \approx \sqrt{m/\hbar t}$ and the collisional velocity $v \approx \sqrt{\hbar/mt}$. For $t \ll t_a$ the cross-section is unitarity-limited, $\sigma \approx 1/k^2 \approx \hbar t/m$ and integrating the decoherence rate yields the universal limit $C(t) \approx (t/t_n)^{3/2}$. At longer times $t \gg t_a$ the cross-section is determined by low-energy collisions $\sigma \sim a^2$ and integrating gives $C(t) \approx (t/t_{\mathrm{w}})^{1/2}$ in accordance with the weak coupling limit (Supplementary Information).

At later times, interactions between multiple particles lead to pronounced deviations from the two-body prediction given by equation (1) and the system enters a regime of many-body dynamics (Fig. 1a, orange area). We describe this many-body dynamics using a diagrammatic theory (Supplementary Information), which has previously been applied to the equilibrium physics of Bose polarons[23,31]. Because our many-body theory contains the dominant two-body processes, it moreover recovers the two-body prediction of equation (1) for short times. For weak interactions, deviations from two-body weak coupling $t^{1/2}$ dynamics occur at times $\sim\hbar/E_{\mathrm{mf}}$ and signal the onset of many-body physics (Fig. 1a, green to orange transition). However, for large interaction strengths where $E_{\mathrm{mf}} > \hbar^2/ma^2$ and consequently $|1/k_n a| < (2/3\pi)^{1/3}$, the many-body dynamics emerges directly from the initial universal regime at times $\sim 1.4t_n$ (Fig. 1, blue to orange transition). We emphasize that these changes in dynamical behaviour correspond to smooth temporal crossovers, as indicated by the blurred boundaries in Fig. 1a.

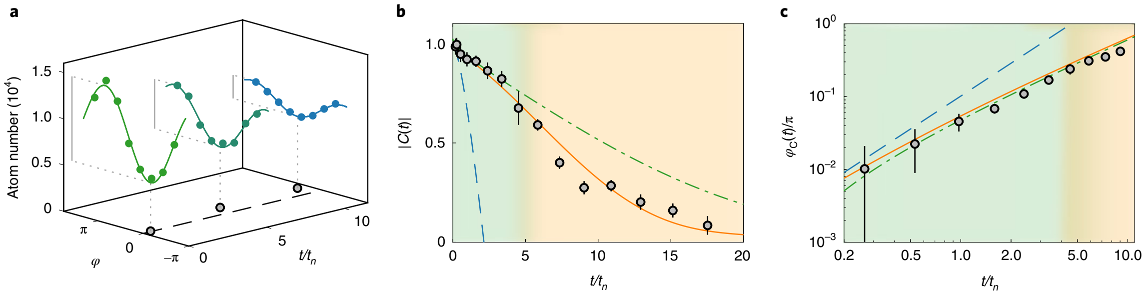

Fig. 2 | Impurity dynamics at weak interaction strength. a, The interference signal recorded at different evolution times as a function of the probe pulse phase φ for an interaction strength $1/k_na = -2$. Sinusoidal fits are shown as solid lines and the obtained amplitude and phase are indicated using grey lines and open circles, respectively. **b**, Coherence amplitude $|C(t)|$. The impurity state decoheres due to interactions with the condensate. **c**, Phase of the coherence, $\varphi_C(t)$. The impurity phase increases as the state rotates on the Bloch sphere, which at weak interaction strength is primarily due to the impurity state mean field interactions E_{mf}. The dashed blue line shows the two-body universal $t^{3/2}$ and the dash-dotted green line shows the weak coupling $t^{1/2}$ prediction according to equation (1). The solid orange line provides the diagrammatic description and the coloured areas illustrate the theoretically predicted dynamical regimes from Fig. 1a. The error bars are 1σ confidence intervals of the fitted values.

Figure 2b,c shows the measured coherence amplitude and phase in the regime of weak interactions. Both measured quantities agree well with the $t^{1/2}$ evolution given by equation (1) for $t \lesssim \hbar/E_{mf}$. The transition between the universal and weak coupling two-body dynamics at short times is extracted by simultaneously fitting the coherence amplitude and phase with the general two-body description (Supplementary Information) using the transition time as a free parameter. These times are shown in Fig. 1a as blue data points. Moreover, the subsequent transition to the many-body regime is identified with the time when the observed coherence amplitude deviates more than two standard deviations from the prediction of equation (1), also shown in Fig. 1a (red data points). Finally, we compare the observations to the diagrammatic prediction, which captures the dynamics on all timescales. In particular, the many-body behaviour is clearly visible for the amplitude at long evolution times. In principle, theory predicts that $|C(t)|$ decays towards the quasiparticle residue[4,5]. However, experimentally this is not observed due to additional decoherence processes (Methods). The excellent agreement between theory and experiment nonetheless provides a benchmark for our measurement approach and theoretical understanding.

For intermediate interaction strengths, the initial coherence amplitude and phase display universal $t^{3/2}$ dynamics extending for longer evolution times as illustrated in Fig. 3. There is no regime exhibiting $t^{1/2}$ dynamics because $t \gg t_a$ is not reached before the smooth transition to many-body dynamics. Furthermore, a measurement of the transition to the many-body regime is prohibited by the inhomogeneous density of our condensate, which obscures the observation of a clear deviation from equation (1). Nonetheless, we obtain excellent agreement with the diagrammatic prediction for all evolution times, which includes these experimental effects.

At unitarity, the crossover time t_a diverges, such that the universal $t^{3/2}$ dynamics dominates the entire two-body scattering regime. Indeed, the initial amplitude and phase evolution shown in Fig. 4 agree very well with the dynamics predicted by equation (1), confirming both the characteristic decay exponent and the associated time constant t_n. This agreement highlights the importance of two-body dynamics over a substantial timespan of initial relaxation, even in the unitary limit.

For longer evolution times, we observe pronounced deviations from equation (1), signalling the onset of many-body correlations due to the strong interaction between the impurity state and the condensate. This behaviour is captured by the diagrammatic prediction, which yields an excellent description of the non-equilibrium dynamics of impurities in the regime of strong interactions and thus demonstrates the many-body nature of the long-time impurity evolution in our experiments. In particular, the data reveal a clear crossover between the initial two-body $t^{3/2}$ dynamics and a slower many-body decay at a transition time, as indicated as a white data point in Fig. 1a.

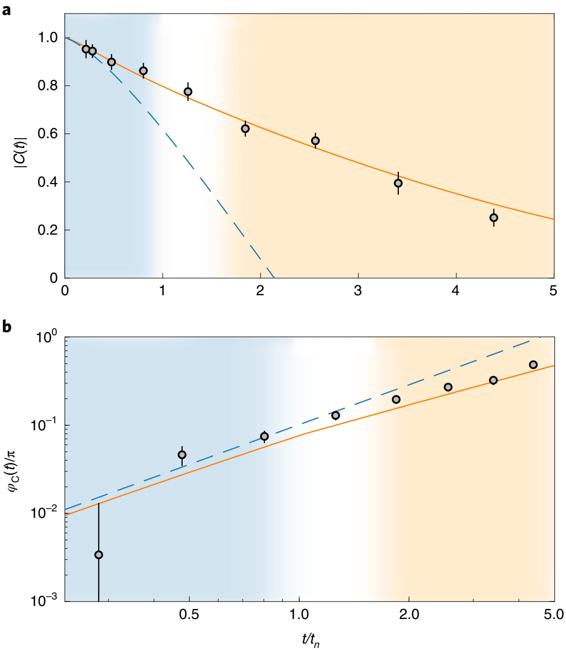

Fig. 3 | Impurity dynamics at intermediate interaction strength. a,**b**, Coherence amplitude (**a**) and phase evolution (**b**) for $1/k_na = -0.77$. The two-body universal $t^{3/2}$ prediction of equation (1) is shown as a dashed blue line. The solid orange line is the diagrammatic prediction and the coloured areas illustrate the theoretically predicted dynamical regimes from Fig. 1a. The error bars are 1σ confidence intervals of the fitted values.

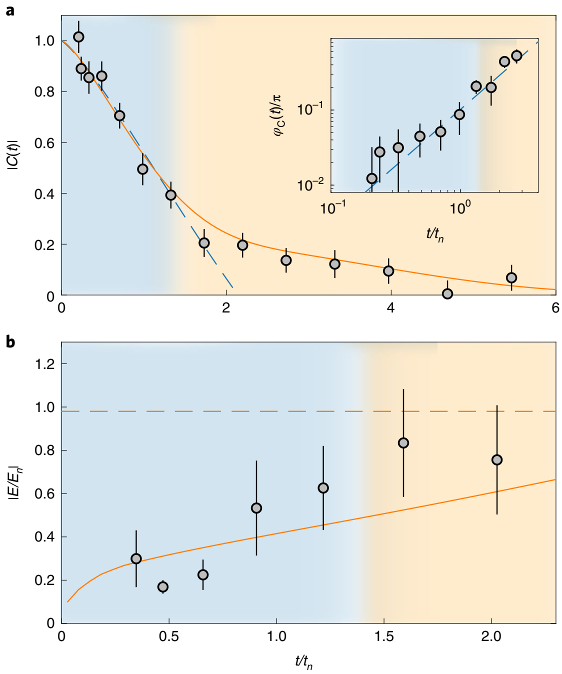

Fig. 4 | Impurity dynamics at unitarity. a, Coherence amplitude and phase evolution (inset). The fast initial decay of the coherence amplitude is in good agreement with the unitary two-body prediction of equation (1), shown as a dashed blue line. At longer times, many-body physics dominates the decay, which is well described by a diagrammatic description that accounts for many-body effects, shown as a solid orange line. **b**, Instantaneous energy obtained from the time derivative of the observed phase. The measured energies agree with the result of diagrammatic theory, shown as a solid orange line, and approach the expected equilibrium energy of the Bose polaron E_p, marked with a dashed line. The coloured areas illustrate the theoretically predicted dynamical regimes from Fig. 1a and the error bars are 1σ confidence intervals of the fitted values.

Moreover, the measured phase evolution allows us to track the instantaneous energy of the impurity. Because the phase evolution $\varphi_C(t)\to -E_p t/\hbar$ for long times is governed by the polaron energy E_p, we obtain the instantaneous energy from $E(t)=-\hbar d\varphi_C/dt$. As shown in Fig. 4b, the observed impurity energy approaches the expected equilibrium polaron energy. Therefore, our measurements directly display the dynamical emergence of the Bose polaron in the regime of strong interactions.

Our experiment covers all relevant timescales of quasiparticle formation and thus opens up new pathways to study non-equilibrium phenomena in strongly interacting quantum many-body systems. The demonstrated technique will enable investigations of bosonic analogues of Anderson's orthogonality catastrophe[32] and transport processes[33,34] via time-domain measurements. Similar measurements at repulsive impurity interactions will be able to explore the predicted formation of multi-phonon bound states[4]. Experiments with higher impurity concentrations will permit the investigation of effective polaron interactions[35]. Such mediated interactions are believed to play a vital role for transport properties of condensed-matter systems[36]. Ultimately, this may enable the observation of strongly bound bosonic bipolarons[37] and their formation in a time-resolved manner. Elucidating the dynamics of induced quasiparticle interactions could prove essential, as strong retardation and relaxation effects[5,35] may render such bipolarons inaccessible to common spectroscopic methods[20,21].

Online content

Any methods, additional references, Nature Research reporting summaries, source data, extended data, supplementary information, acknowledgements, peer review information; details of author contributions and competing interests; and statements of data and code availability are available at https://doi.org/10.1038/s41567-021-01184-5.

Received: 1 May 2020; Accepted: 22 January 2021;

References

1. Landau, L. D. Über die Bewegung der Elektronen in Kristalgitter. *Phys. Z. Sowjet.* **3**, 644–645 (1933).
2. Pekar, S. I. Autolocalization of the electron in an inertially polarizable dielectric medium. *Zh. Eksp. Teor. Fiz.* **16**, 335 (1946).
3. Shashi, A., Grusdt, F., Abanin, D. A. & Demler, E. Radio-frequency spectroscopy of polarons in ultracold Bose gases. *Phys. Rev. A* **89**, 053617 (2014).
4. Shchadilova, Y. E., Schmidt, R., Grusdt, F. & Demler, E. Quantum dynamics of ultracold Bose polarons. *Phys. Rev. Lett.* **117**, 113002 (2016).
5. Nielsen, K. K., Ardila, L. A. P., Bruun, G. M. & Pohl, T. Critical slowdown of non-equilibrium polaron dynamics. *New J. Phys.* **21**, 043014 (2019).
6. Mistakidis, S. I., Katsimiga, G. C., Koutentakis, G. M., Busch, T. & Schmelcher, P. Quench dynamics and orthogonality catastrophe of Bose polarons. *Phys. Rev. Lett.* **122**, 183001 (2019).
7. Drescher, M., Salmhofer, M. & Enss, T. Theory of a resonantly interacting impurity in a Bose–Einstein condensate. *Phys. Rev. Res.* **2**, 032011 (2020).
8. Mannella, N. et al. Nodal quasiparticle in pseudogapped colossal magnetoresistive manganites. *Nature* **438**, 474–478 (2005).
9. Lee, P. A., Nagaosa, N. & Wen, X.-G. Doping a Mott insulator: physics of high-temperature superconductivity. *Rev. Mod. Phys.* **78**, 17–85 (2006).
10. Bloch, I., Dalibard, J. & Nascimbène, S. Quantum simulations with ultracold quantum gases. *Nat. Phys.* **8**, 267–276 (2012).
11. Schirotzek, A., Wu, C.-H., Sommer, A. & Zwierlein, M. W. Observation of Fermi polarons in a tunable Fermi liquid of ultracold atoms. *Phys. Rev. Lett.* **102**, 230402 (2009).
12. Kohstall, C. et al. Metastability and coherence of repulsive polarons in a strongly interacting Fermi mixture. *Nature* **485**, 615–618 (2012).
13. Koschorreck, M. et al. Attractive and repulsive Fermi polarons in two dimensions. *Nature* **485**, 619–622 (2012).
14. Massignan, P., Zaccanti, M. & Bruun, G. M. Polarons, dressed molecules and itinerant ferromagnetism in ultracold fermi gases. *Rep. Prog. Phys.* **77**, 034401 (2014).
15. Cetina, M. et al. Ultrafast many-body interferometry of impurities coupled to a Fermi sea. *Science* **354**, 96–99 (2016).
16. Scazza, F. et al. Repulsive Fermi polarons in a resonant mixture of ultracold ^{6}Li atoms. *Phys. Rev. Lett.* **118**, 083602 (2017).
17. Schmidt, R. et al. Universal many-body response of heavy impurities coupled to a Fermi sea: a review of recent progress. *Rep. Prog. Phys.* **81**, 024401 (2018).
18. Yan, Z. et al. Boiling a unitary Fermi liquid. *Phys. Rev. Lett.* **122**, 093401 (2019).
19. Darkwah Oppong, N. et al. Observation of coherent multiorbital polarons in a two-dimensional Fermi gas. *Phys. Rev. Lett.* **122**, 193604 (2019).
20. Jørgensen, N. B. et al. Observation of attractive and repulsive polarons in a Bose–Einstein condensate. *Phys. Rev. Lett.* **117**, 055302 (2016).
21. Hu, M.-G. et al. Bose polarons in the strongly interacting regime. *Phys. Rev. Lett.* **117**, 055301 (2016).
22. Yan, Z. Z., Ni, Y., Robens, C. & Zwierlein, M. W. Bose polarons near quantum criticality. *Science* **368**, 190–194 (2020).
23. Peña Ardila, L. A. et al. Analyzing a Bose polaron across resonant interactions. *Phys. Rev. A* **99**, 063607 (2019).
24. Parish, M. M. & Levinsen, J. Quantum dynamics of impurities coupled to a Fermi sea. *Phys. Rev. B* **94**, 184303 (2016).
25. Wacker, L. et al. Tunable dual-species Bose–Einstein condensates of ^{39}K and ^{87}Rb. *Phys. Rev. A* **92**, 053602 (2015).
26. Lysebo, M. & Veseth, L. Feshbach resonances and transition rates for cold homonuclear collisions between ^{39}K and ^{41}K atoms. *Phys. Rev. A* **81**, 032702 (2010).
27. Tanzi, L. et al. Feshbach resonances in potassium Bose–Bose mixtures. *Phys. Rev. A* **98**, 062712 (2018).

28. Cetina, M. et al. Decoherence of impurities in a Fermi sea of ultracold atoms. *Phys. Rev. Lett.* **115**, 135302 (2015).
29. Fletcher, R. J. et al. Two- and three-body contacts in the unitary Bose gas. *Science* **355**, 377–380 (2017).
30. Braaten, E., Kang, D. & Platter, L. Short-time operator product expansion for rf spectroscopy of a strongly interacting Fermi gas. *Phys. Rev. Lett.* **104**, 223004 (2010).
31. Rath, S. P. & Schmidt, R. Field-theoretical study of the Bose polaron. *Phys. Rev. A* **88**, 053632 (2013).
32. Knap, M. et al. Time-dependent impurity in ultracold fermions: orthogonality catastrophe and beyond. *Phys. Rev. X* **2**, 041020 (2012).
33. Sommer, A., Ku, M. & Zwierlein, M. W. Spin transport in polaronic and superfluid Fermi gases. *New J. Phys.* **13**, 055009 (2011).
34. Bardon, A. B. et al. Transverse demagnetization dynamics of a unitary Fermi gas. *Science* **344**, 722–724 (2014).
35. Camacho-Guardian, A. & Bruun, G. M. Landau effective interaction between quasiparticles in a Bose–Einstein condensate. *Phys. Rev. X* **8**, 031042 (2018).
36. Alexandrov, A. S. & Devreese, J. T. *Advances in Polaron Physics* Vol. 159 (Springer, 2010).
37. Camacho-Guardian, A., Peña Ardila, L. A., Pohl, T. & Bruun, G. M. Bipolarons in a Bose–Einstein condensate. *Phys. Rev. Lett.* **121**, 013401 (2018).

Methods

Experimental preparation. To study the impurity dynamics, a Bose–Einstein condensate of ^{39}K atoms in the $|F=1, m_F=-1\rangle$ state was prepared in an optical dipole potential[25]. The evaporation was performed near a Feshbach resonance at 33.6 G before ramping the magnetic field to a desired valued close to the interstate Feshbach resonance at 113.8 G. The cloud temperature was kept constant at 50 nK throughout the measurements and the mean geometrical trap frequency was $2\pi \times 65$ Hz, ensuring an average condensate density of $n_B = 0.7 \times 10^{14}\,\text{cm}^{-3}$.

Decoherence. Three additional experimental decoherence processes are included in the theoretical description of the coherence. To account for processes due to trap inhomogeneity, the coherence amplitude and phase were integrated over the cloud density. The effects of finite lifetime were included by multiplying the theoretical coherence amplitude with an exponential function based on an independently measured loss rate Γ_{loss}. The magnetic field noise was included similarly by multiplying the theoretical coherence amplitude with a decay due to shot-to-shot fluctuations, which was measured independently (Supplementary Information).

Data availability

The data that support the findings of this study are available from the corresponding author upon reasonable request.

Code availability

The code that supports the findings of this study is available from the corresponding author upon reasonable request.

Acknowledgements

We thank L. A. Peña Ardila for helpful discussions. This work was supported by the Villum Foundation, the Carlsberg Foundation, the Danish Council for Independent Research, the Danish National Research Foundation through the Center of Excellence 'CCQ' (grant no. DNRF156) and T.P. acknowledges support through a Niels Bohr Professorship.

Author contributions

M.G.S., T.G.S., N.B.J. and J.J.A. designed and carried out the experiment. M.G.S. performed the data analysis. K.K.N., A.C.-G., T.P. and G.M.B. provided the theoretical predictions. All authors contributed to writing the manuscript.

Competing interests

The authors declare no competing interests.

Additional information

Supplementary information The online version contains supplementary material available at https://doi.org/10.1038/s41567-021-01184-5.

Correspondence and requests for materials should be addressed to M.G.S.

Peer review information *Nature Physics* thanks Francesco Scazza and the other, anonymous, reviewer(s) for their contribution to the peer review of this work.

Supplementary Information for "Non-equilibrium quantum dynamics and formation of the Bose polaron"

Magnus G. Skou,[1] Thomas G. Skov,[1] Nils B. Jørgensen,[1] Kristian K. Nielsen,[1]
Arturo Camacho-Guardian,[1] Thomas Pohl,[1] Georg M. Bruun,[1,2] and Jan J. Arlt[1]

[1]*Center for Complex Quantum Systems, Department of Physics and Astronomy,*
Aarhus University, Ny Munkegade 120, DK-8000 Aarhus C, Denmark.
[2]*Shenzhen Institute for Quantum Science and Engineering and Department of Physics,*
Southern University of Science and Technology, Shenzhen 518055, China.

(Dated: January 11, 2021)

SI. RAMSEY INTERFEROMETRY

The customized Ramsey method employed in the experiment maps the impurity coherence to the final number of atoms in the sample. We first analyze the homogeneous case and then perform a local density approximation (LDA) to analyze the experimentally relevant inhomogeneous gas. To generate impurities, a radio frequency (rf) field

$$H_{\mathrm{rf}}(\varphi) = \hbar\Omega \sum_{\mathbf{k}} \left[\mathrm{e}^{+i\varphi} c^\dagger_{\mathbf{k}} b_{\mathbf{k}} + \mathrm{e}^{-i\varphi} b^\dagger_{\mathbf{k}} c_{\mathbf{k}} \right] \tag{S1}$$

drives transitions between two magnetic states, transferring atoms from the medium $|b\rangle$ state to the impurity $|c\rangle$ state. The operators $b^\dagger_{\mathbf{k}}, c^\dagger_{\mathbf{k}}$ create an atom in the medium and impurity states with momentum **k**, respectively, and H_{rf} is given in the rotating frame with the Rabi frequency Ω and phase φ. The system Hamiltonian for resonant transfer – in the rotating frame – is given by

$$H = \sum_{\mathbf{k}} \varepsilon_{\mathbf{k}} \left(c^\dagger_{\mathbf{k}} c_{\mathbf{k}} + b^\dagger_{\mathbf{k}} b_{\mathbf{k}} \right) + \frac{\mathcal{T}_{\mathrm{B}}}{2V} \sum_{\mathbf{k},\mathbf{q},\mathbf{p}} b^\dagger_{\mathbf{k}+\mathbf{p}} b^\dagger_{\mathbf{q}-\mathbf{p}} b_{\mathbf{q}} b_{\mathbf{k}} + \frac{\mathcal{T}}{V} \sum_{\mathbf{k},\mathbf{q},\mathbf{p}} b^\dagger_{\mathbf{k}+\mathbf{p}} c^\dagger_{\mathbf{q}-\mathbf{p}} c_{\mathbf{q}} b_{\mathbf{k}}, \tag{S2}$$

with $\varepsilon_{\mathbf{k}} = \hbar^2 \mathbf{k}^2/2m$, system volume V, and $\mathcal{T} = 4\pi\hbar^2 a/m$, $\mathcal{T}_{\mathrm{B}} = 4\pi\hbar^2 a_{\mathrm{B}}/m$ the zero energy scattering matrices for the impurity-boson and boson-boson interactions respectively. Here we assume that only a single impurity is present, neglecting any impurity-impurity interactions. The Ramsey sequence consists of two short rf-pulses as described in the main text. Since the duration of these pulses is much shorter than the impurity dynamics investigated, we can safely split the time evolution operator into three separate parts $\mathcal{U}_{\mathrm{tot}}(t) = \mathcal{U}_{\mathrm{rf}}(\varphi, \delta t) \mathcal{U} \mathcal{U}_{\mathrm{rf}}(0, \delta t)$. Here $\mathcal{U}_{\mathrm{rf}}(\varphi, t) = \mathrm{e}^{-iH_{\mathrm{rf}}(\varphi)t}$

and $\mathscr{U} = \mathrm{e}^{-iHt}$. In the first pulse we drive at zero phase, in the second at some variable *probe* phase, φ. To stay in the single impurity limit we require $\Omega\delta t \ll 1$, which in turn means that we can expand the rf evolution operator

$$\mathscr{U}_{\mathrm{rf}}(\varphi, \delta t) \simeq 1 - iH_{\mathrm{rf}}(\varphi)\delta t - \frac{(H_{\mathrm{rf}}(\varphi)\delta t)^2}{2}, \tag{S3}$$

to second order in $\Omega\delta t$. The initial state of the system is the ground state $|\mathrm{BEC}\rangle$ of H with no impurities present. Using the time evolution operator $\mathscr{U}_{\mathrm{tot}}(t)$ together with the expansion (S3), we obtain the mean number of atoms in the impurity state after the two rf-pulses

$$N_{\mathrm{c}}(t) = \langle\mathrm{BEC}|\,\mathscr{U}^{\dagger}_{\mathrm{tot}}(t)\sum_{\mathbf{k}} c^{\dagger}_{\mathbf{k}}c_{\mathbf{k}}\mathscr{U}_{\mathrm{tot}}(t)\,|\mathrm{BEC}\rangle = N_{\mathrm{B}}\cdot 2(\Omega\delta t)^2\mathrm{Re}\left[1 + \mathrm{e}^{-i\varphi}\cdot iG_{\mathrm{bc}}(t)\right], \tag{S4}$$

which is *exact* to second order in $\Omega\delta t$. Here N_{B} is the initial total number of atoms in the $|b\rangle$ state, and

$$G_{\mathrm{bc}}(t) = -\frac{i}{N_{\mathrm{B}}}\sum_{\mathbf{k},\mathbf{q}}\langle\mathrm{BEC}|\,b^{\dagger}_{\mathbf{k}}(t)c_{\mathbf{k}}(t)c^{\dagger}_{\mathbf{q}}(0)b_{\mathbf{q}}(0)\,|\mathrm{BEC}\rangle$$

is an impurity-boson Green's function with $c_{\mathbf{k}}(t) = \mathscr{U}^{\dagger}(t)c_{\mathbf{k}}(0)\mathscr{U}(t)$ the time evolved annihilation operator for the impurity – likewise for $b_{\mathbf{k}}(t)$. Since the medium atoms are condensed in the zero momentum mode, the dominant contribution to G_{bc} comes from $k = q = 0$. Additional contributions are suppressed by at least a factor of $1/\sqrt{N_{\mathrm{B}}}$.

We therefore find

$$G_{\mathrm{bc}}(t) \simeq -\frac{i}{N_{\mathrm{B}}}\langle\mathrm{BEC}|\,b^{\dagger}_0(t)c_0(t)c^{\dagger}_0(0)b_0(0)\,|\mathrm{BEC}\rangle \simeq -i\,\langle\mathrm{BEC}|\,c_0(t)c^{\dagger}_0(0)\,|\mathrm{BEC}\rangle = G_0(t), \tag{S5}$$

using $b_0\,|\mathrm{BEC}\rangle \simeq \sqrt{N_{\mathrm{B}}}\,|\mathrm{BEC}\rangle$. We also use $\langle\mathrm{BEC}|\,b^{\dagger}_0(t) \simeq \langle\mathrm{BEC}|\,b^{\dagger}_0(0) \simeq \sqrt{N_{\mathrm{B}}}\cdot\langle\mathrm{BEC}|$. This assumes that the impurity dynamics has little effect on the condensate reservoir. This is well justified for a small fraction of impurities, where corrections are again expected to scale as $1/\sqrt{N_{\mathrm{B}}}$. Finally, using that $iG_0(t) = C(t)/C(0)$ [1], we obtain a mapping between the impurity density and coherence $C(t)$

$$n_{\mathrm{c}}(t) = n_{\mathrm{B}}\cdot 2(\Omega\delta t)^2\mathrm{Re}\left[1 + \mathrm{e}^{-i\varphi}\cdot C(t)\right], \tag{S6}$$

by dividing out the system volume, V, setting $C(0) = 1$, and defining the initial atom density $n_{\mathrm{B}} = N_{\mathrm{B}}/V$.

In the experiment, the atomic gas is held in a harmonic trap $V(\mathbf{r}) = m(\omega_x^2 x^2 + \omega_y^2 y^2 + \omega_z^2 z^2)/2$. As a result the atomic density is spatially dependent and we adjust the analysis above by using LDA. In a standard Thomas-Fermi approximation this leads to the density $n_{\mathrm{B}}(\mathbf{r}) = (\mu - V(\mathbf{r}))/\mathscr{T}_{\mathrm{B}}$, where μ is the chemical potential of the condensate. In the local density approximation, Eq. (S6) is replaced by the local equation $n_{\mathrm{c}}(\mathbf{r},t) = n_{\mathrm{B}}(\mathbf{r}) \cdot 2(\Omega\delta t)^2 \mathrm{Re}[1 + \mathrm{e}^{-i\varphi} \cdot C(\mathbf{r},t)]$, where $C(\mathbf{r},t)$ is the local coherence. The number of impurities after the two rf-pulses is then

$$N_{\mathrm{c}}(t) = \int \mathrm{d}^3 r \, n_{\mathrm{c}}(\mathbf{r},t) = N_{\mathrm{B}} \cdot 2(\Omega\delta t)^2 \mathrm{Re}\left[1 + \mathrm{e}^{i\varphi} \cdot C(t)\right],$$

defining the trap averaged coherence $C(t) = \int \mathrm{d}^3 r \, n(\mathbf{r}) C(\mathbf{r},t)/N_{\mathrm{B}}$. Subsequent to the second rf-pulse the atoms are held in the trap, allowing three body recombination to take place, eventually resulting in the loss of two medium atoms for every impurity. The final remaining number of atoms in the system is thus

$$\begin{aligned} N &= N_{\mathrm{B}} - 3N_{\mathrm{c}} = N_{\mathrm{B}}\left(1 - 6(\Omega\delta t)^2 \mathrm{Re}\left[1 + \mathrm{e}^{-i\varphi} \cdot C(t)\right]\right) \\ &= N_0 - 6N_{\mathrm{B}}(\Omega\delta t)^2 |C(t)| \cos(\varphi - \varphi_C(t)), \end{aligned} \tag{S7}$$

with $N_0 = N_{\mathrm{B}}(1 - 6(\Omega\delta t)^2)$ the average number of atoms measured as a function of the probe phase φ for every evolution time t. To enable the experimental analysis the coherence is expressed in terms of its amplitude and phase: $C(t) = |C(t)|\mathrm{e}^{i\varphi_C(t)}$. By performing a fit $N(\varphi) = N_0 - \mathscr{A}\cos(\varphi - \varphi_C)$ to the measured data, we thus extract the phase and the normalized coherence amplitude $|C(t)| = |\mathscr{A}(t)/\mathscr{A}(0)|$ simultaneously.

SII. THEORETICAL DESCRIPTION OF IMPURITY DYNAMICS

The impurity coherence is in general equal to the Fourier transform of the impurity spectral function $A(\omega)$ at zero momentum

$$C(t) = \int_{-\infty}^{+\infty} \frac{\mathrm{d}\omega}{2\pi} \mathrm{e}^{-i\omega t} A(\omega). \tag{S8}$$

Our approach to predict impurity dynamics is to calculate the spectral function $A(\omega)$ and then determine the dynamics of the coherence. In this section, we present the theoretical description of different regimes of impurity dynamics, from universal short-time behaviour to the non-perturbative treatment of a polaron formation.

A. Initial two-body dynamics

We start by analysing the short-time behaviour of the coherence. The integral in Eq. (S8) is split as follows

$$C(t)=\int_{-\infty}^{\infty}\frac{\mathrm{d}\omega}{2\pi}(1-i\omega t)A(\omega)+\int_{-\infty}^{\infty}\frac{\mathrm{d}\omega}{2\pi}\left(\mathrm{e}^{-i\omega t}-(1-i\omega t)\right)A(\omega). \tag{S9}$$

It is then apparent that we can use the so-called sum rules [2]

$$\int_{-\infty}^{\infty}\frac{\mathrm{d}\omega}{2\pi}A(\omega)=1,\qquad \int_{-\infty}^{\infty}\frac{\mathrm{d}\omega}{2\pi}\,\omega A(\omega)=\frac{a_{\mathrm{B}}^{-1}-a^{-1}}{4\pi m}\frac{\hbar C_2}{N_{\mathrm{B}}}, \tag{S10}$$

here appropriately rewritten in terms of the spectral function, to calculate the first term in Eq. (S9). The two-body contact of the BEC, $C_2=8\pi m a_{\mathrm{B}}^2/\hbar^2\cdot\mathrm{d}E_{\mathrm{BEC}}/\mathrm{d}a_{\mathrm{B}}=N_{\mathrm{B}}\cdot 16\pi^2 n_{\mathrm{B}}a_{\mathrm{B}}^2$, is obtained using Bogoliubov theory appropriate for weak interactions in the condensate, $n_{\mathrm{B}}{a_{\mathrm{B}}}^3\ll 1$. The second term in Eq. (S9) can be evaluated at short times, since the factor $\mathrm{e}^{-i\omega t}-(1-i\omega t)$ removes the low energy sector up to order $(\omega t)^2$. Therefore, at sufficiently short times, one can use the asymptotic behavior of the spectral function at large frequencies calculated in [2]

$$\lim_{\omega\to\infty}A(\omega)=\frac{1}{2\pi}\frac{C_2}{N_{\mathrm{B}}}\sqrt{\frac{\hbar}{m}}\frac{(a/a_{\mathrm{B}}-1)^2}{1+ma^2\,\omega/\hbar}\cdot\frac{1}{\omega^{3/2}}=\frac{K}{1+\omega t_a}\cdot\frac{1}{\omega^{3/2}}, \tag{S11}$$

with $K=4/3\pi\cdot(1-a_{\mathrm{B}}/a)^2(k_n|a|)^3/\sqrt{t_a}$, $k_n=(6\pi^2 n_{\mathrm{B}})^{1/3}$ and $t_a=ma^2/\hbar$. The $\omega<0$ part of the second term in Eq. (S9) is negligible for negative impurity-boson scattering lengths *and* close to unitarity. Essentially, the only important contribution in this region is due to the impurity-boson molecular state, which is absent for $a<0$ and has an energy $E=-\hbar^2/ma^2$ which goes to zero as we approach unitarity $a\to\infty$. We can thus write

$$\begin{aligned}C(t)&\simeq\int_{-\infty}^{\infty}\frac{\mathrm{d}\omega}{2\pi}(1-i\omega t)A(\omega)+\int_{0}^{\infty}\frac{\mathrm{d}\omega}{2\pi}\left(\mathrm{e}^{-i\omega t}-(1-i\omega t)\right)A(\omega)\\&\simeq 1-it\cdot\frac{n_{\mathrm{B}}\mathscr{T}_{\mathrm{B}}}{\hbar}\left(1-\frac{a_{\mathrm{B}}}{a}\right)+K\underbrace{\int_{0}^{\infty}\frac{\mathrm{d}\omega}{2\pi}\frac{\mathrm{e}^{-i\omega t}-(1-i\omega t)}{1+\omega t_a}\cdot\frac{1}{\omega^{3/2}}}_{I},\end{aligned} \tag{S12}$$

using $\hbar C_2/N_{\mathrm{B}}\cdot(a_{\mathrm{B}}^{-1}-a^{-1})/4\pi m=n_{\mathrm{B}}\mathscr{T}_{\mathrm{B}}(1-a_{\mathrm{B}}/a)/\hbar$. The integral I is evaluated using the dimensionless variables $\tilde{\omega}=\omega t_a$ and $\tilde{t}=t/t_a$

$$I=\frac{\sqrt{t_a}}{2}\left[1+i\frac{t}{t_a}-\frac{2}{\sqrt{\pi}}\mathrm{e}^{it/t_a}\Gamma\left(\frac{3}{2},i\frac{t}{t_a}\right)\right],$$

where Γ is the incomplete gamma function. Reinserting I into Eq. (S12) we obtain the short-time behavior of the impurity coherence for general interaction strengths

$$C(t) \simeq 1 - i\frac{E_{\mathrm{mf}}t}{\hbar} + \frac{2}{3\pi}(k_n|a|)^3\left[1 - \frac{2}{\sqrt{\pi}}\mathrm{e}^{it/t_a}\Gamma\left(\frac{3}{2}, i\frac{t}{t_a}\right)\right], \tag{S13}$$

defining the mean field energy $E_{\mathrm{mf}} = n_{\mathrm{B}}\mathscr{T}$ and neglecting a_{B}/a corrections. At very short times, $t \ll t_a = ma^2/\hbar$, the coherence dynamics has the universal behaviour

$$C(t) = 1 - (1-i)\frac{16}{9\pi^{3/2}}\left(\frac{t}{t_n}\right)^{3/2}. \tag{S14}$$

Since it is independent of the impurity-boson scattering length, a, this defines a unitarity limited dynamical regime.

For weak interactions, the impurity dynamics changes from this two-body unitary dynamics to two-body weak-coupling dynamics governed by

$$C(t) = 1 - iE_{\mathrm{mf}}t/\hbar - (1+i)\left(\frac{t}{t_{\mathrm{w}}}\right)^{1/2}, \tag{S15}$$

for $\hbar/E_{\mathrm{mf}} \gg t \gg ma^2/\hbar$, valid to second order in the impurity-boson scattering length. The third-order correction in the impurity-boson scattering length from Eq. (S13) leads to the following dynamics

$$C(t) = 1 - iE_{\mathrm{mf}}t/\hbar - (1+i)\left(\frac{t}{t_{\mathrm{w}}}\right)^{1/2} + \frac{2}{3\pi}(k_n|a|)^3, \tag{S16}$$

where the fourth term becomes relevant for $1/k_n|a| \approx (2/3\pi)^{1/3} \approx 0.59$ which determines the transition from weak to strong interactions.

B. Origin of the two-body power-laws

The exponent of the power-laws in Eq. (S14) and Eq. (S15) can be traced back to the cross section $\sigma(k) = 4\pi a^2/[1+(ka)^2]$ for s-wave scattering between the impurity and a boson from the condensate with relative momentum k. At time t, the characteristic collision energy giving rise to decoherence is $E \sim \hbar/t$ so that $k \sim \sqrt{m/\hbar t}$ and the typical velocity of the colliding particles is $v \sim \sqrt{\hbar/mt}$.

At short times $t \ll ma^2/\hbar$ these collisional energies are correspondingly high $E \gg \hbar^2/ma^2$ such that $ka \gg 1$ and the cross section is unitarity-limited $\sigma(k) \simeq 4\pi/k^2 \sim \hbar t/m$. Using that the decoherence rate is related to the collision rate $\dot{C}(t) \sim -n_B\sigma v$, we obtain $\dot{C}(t) \sim -n_B(\hbar/m)^{3/2}\sqrt{t}$ and integrating while setting $C(0) = 1$ yields precisely the $(t/t_n)^{3/2}$ power-law given in Eq. (S14). On the other hand, for longer times $t \gg ma^2/\hbar$ decoherence involves low energy collisions for which the cross section is $\sigma(k) \simeq 4\pi a^2$. The same line of reasoning then gives the $\sqrt{t/t_w}$ power law in Eq. (S15).

C. Many-body dynamics

To determine the impurity dynamics at arbitrary times, we employ a non-perturbative approach based on the so-called ladder approximation, which includes Feshbach physics via the scattering of one boson out of the condensate by the impurity [3]. For $k_n a_B \approx 0.01$, the relevant physics can be explained by assuming an ideal BEC, where the impurity self-energy is $\Sigma(\omega) = n_\mathrm{B}\mathscr{T}(\omega)$, with the scattering matrix $\mathscr{T}(\omega)$ in the ladder approximation and the density n_B of the BEC. This yields the spectral function

$$A(\omega) = Z_P 2\pi\delta(\omega-\omega_P) + 8\pi\frac{\hbar^{3/2}n_\mathrm{B}}{m^{3/2}\omega^{5/2}}\cdot\frac{\Theta(\omega)}{1+\frac{\hbar}{ma^2\omega}\left(1-\frac{4\pi\hbar n_\mathrm{B}a}{m\omega}\right)^2} \tag{S17}$$

for zero temperature. Here $\delta(x)$ is the Dirac delta function, $\Theta(\omega)$ is the Heaviside step function, $\hbar\omega_P$ is the polaron energy and Z_P is the polaron residue determined from $\omega_P = \Sigma(\omega_P)$ and $Z_P^{-1} = 1 - \partial_\omega\Sigma(\omega)|_{\omega_P}$. Equation (S17) recovers the exact result for large ω in Eq. (S11). In addition, it yields a prediction for the low-energy behaviour governed by many-body physics. Specifically, many-body corrections are given by the continuum of high-momentum impurity states and Bogoliubov excitations together with the polaron delta-function peak. The onset of the continuum of states described by the second term in Eq. (S17) starts above the polaron peak instead of at $\omega = 0$, since one can make states with arbitrarily small excitation energy, consisting of a moving polaron and a Bogoliubov mode with a total momentum of zero. In our predictions, we therefore employ a step in a self-consistent calculation which moves the continuum to start just above the polaron peak. In addition, we add a small imaginary width $i\eta = 0.05E_n$. Moreover, the theory is averaged over the trap to model the experiment. Finally, by Fourier transforming the result we obtain the prediction for the coherence which is shown in Fig. 2, 3 and 4 of the main manuscript.

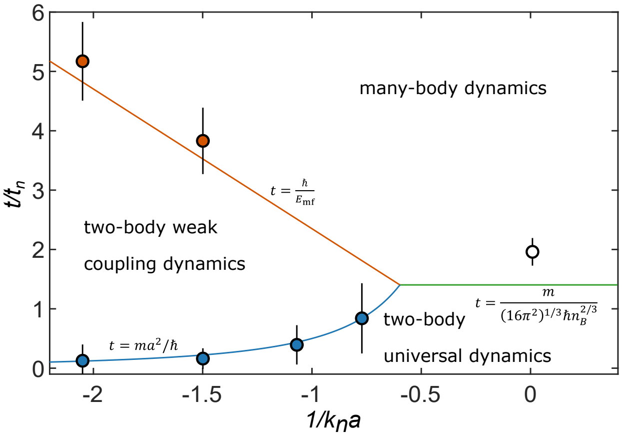

FIG. S1. Regimes of impurity dynamics as a function of inverse interaction strength $1/k_n a$ and evolution time t/t_n. The lines show the transition times separating the different dynamical regimes: The universal to weak-coupling transition is shown in blue, the weak-coupling to many-body transition is shown in orange, and the universal to many-body transition is shown in green. The points show the experimentally observed transition times and the error bars correspond to the 1σ confidence intervals of the fitted values (blue) and the data resolution (red and white) as described in Sec. SV C. We emphasize that although the transitions are shown as lines, they are in reality smooth as indicated in Fig. 1a in the main manuscript.

D. Dynamical regimes of impurity evolution

We can now identify various regimes of the impurity dynamics by comparing the relative magnitude of the terms in the denominator of Eq. (S17). The result is shown in Fig. S1 where the transitions between different regimes are smooth and should not be understood as sharp boundaries. For high energies, corresponding to short times, the spectral function scales as $\omega^{-5/2}$ giving the universal $t^{3/2}$ dynamics described by Eq. (S14). For weak interactions ($E_\mathrm{mf} \ll \hbar^2/ma^2$), there is a transition to the $t^{1/2}$ dynamics also described by Eq. (S15) for $t \gtrsim t_a = ma^2/\hbar$ and eventually many-body physics sets in at $t \gtrsim \hbar/E_\mathrm{mf}$. Since $ma^2/\hbar$ establishes the crossover between the different regimes of two-body impurity dynamics, the transition to Eq. (S15) is restricted to values of the interaction strengths such that $ma^2/\hbar$ remains the shortest time-scale of the system. Using the condition $t_a = \hbar/E_\mathrm{mf}$ this holds true for weak and intermediate interactions strength until $1/(k_n|a|) = (2/3\pi)^{1/3}$, in agreement with Eq. (S16). For strong interactions ($E_\mathrm{mf} \geq \hbar^2/ma^2$),

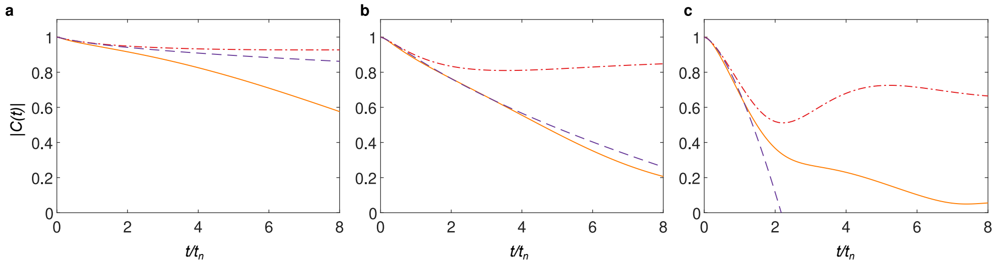

FIG. S2. Loss of coherence due to the harmonic trap potential. The coherence amplitude for (a) $1/k_n a = -2$, (b) $1/k_n a = -0.77$ and (c) $1/k_n a = 0.01$ are shown for the general two-body description Eq. (S13) as a dashed purple line and the diagrammatic prediction with and without trap dephasing as a solid orange and dash-dotted red line, respectively. No other technical decoherence sources are included for this comparison.

this is no longer the case and the crossover to the $t^{1/2}$ dynamics in Eq. (S15) is prevented. Here, the coherence transitions directly from the universal $t^{3/2}$ dynamics to the many-body dynamics at $t \gtrsim (16\pi^2)^{-1/3} m n_B^{-2/3}/\hbar = (3\pi/2)^{2/3}/2 \cdot t_n \simeq 1.4\, t_n$, as shown in Fig. S1.

SIII. DECOHERENCE EFFECTS

To accurately describe the evolution of the coherence, every prominent technical source of decoherence must be considered. This section accounts for three decoherence mechanisms which are included in our theoretical description of the data.

A. Decoherence from harmonic trap

The harmonic potential provided by the optical dipole trap results in an inhomogeneous density distribution of the atoms. Since the impurity population is created evenly across the condensate, the density dependent interaction strength results in dephasing of the system. We therefore have to integrate over the spatially dependent terms of the coherence weighted by the density distribution. For the short-time two-body theoretical predictions in Sec. SII A, this simply corresponds to replacing the density distribution with its average value, since all terms are linear in density. For the dynamics occurring at longer times, the density dependence becomes non-linear and the averaging induces a more subtle decoherence process of the impurity dynamics. For weak interactions, the trap-averaged dynamics and the homogeneous dynamics both signal the onset of many-body physics as they deviate from the two-body prediction at similar times, as shown in Fig. S2a. For intermediate interaction strengths, dephasing suppresses the trap-averaged prediction and it deviates faster from the homogeneous dynamics than from the two-body theory. Subsequently, the trap-averaged many-body and the two-body theory agree for longer times than the transition time predicted by the homogeneous dynamics, as illustrated in Fig. S2b. For strong interactions, the dephasing only affects impurity dynamics at times larger than the transition time from universal to many-body dynamics, and therefore, it is possible to extract the transition from the trap-averaged data, as shown in Fig. S2c.

B. Decoherence from finite impurity lifetime

Strongly interacting Bose gases are typically subject to rapid loss from inelastic three-body decay. In Ramsey interferometry, such decay processes result in a loss of contrast and must therefore be taken into account. In our experimental system the impurity lifetime is typically shorter than the time of flight and all impurity population is lost before it can be observed using absorption imaging after expansion.

We therefore employ a more sophisticated strategy to measure the impurity loss rate: A BEC is prepared in the $|F=1, m_F=-1\rangle$ state under conditions similar to those presented in the main text. To initialize a loss measurement, a rf-pulse transfers approximately 10% of the population to the impurity state $|F=1, m_F=0\rangle$. The sample is then held for a variable time during which three-body recombination processes take place. Subsequently, any remaining population in the impurity state is transferred to the $|F=1, m_F=1\rangle$ state by a π-pulse. The population in this state undergoes two-body spin-changing collisions with the population in the $|F=1, m_F=-1\rangle$ state and is rapidly lost. Thus, the transferred fraction is always lost, but through different processes depending on the state in which the loss takes place. Finally, the remaining number of BEC atoms is recorded by absorption imaging after expansion.

Examples of the recorded normalized atom number are shown in the inset of Fig. S3 for selected interaction strengths $1/k_n a$. For each interaction, we perform an exponential fit $\sim \exp(-\Gamma_{\text{loss}} t)$, with Γ_{loss} being the loss rate of the impurity state. The obtained loss rates are shown in Fig. S3, and as expected, the loss rate increases with the interaction strength.

These observations are relevant in relation to recent Bose polaron observations [4, 5]. Importantly, the observed loss rate $\hbar\Gamma_{\text{loss}}$ is smaller than the Bose polaron energies observed in the same

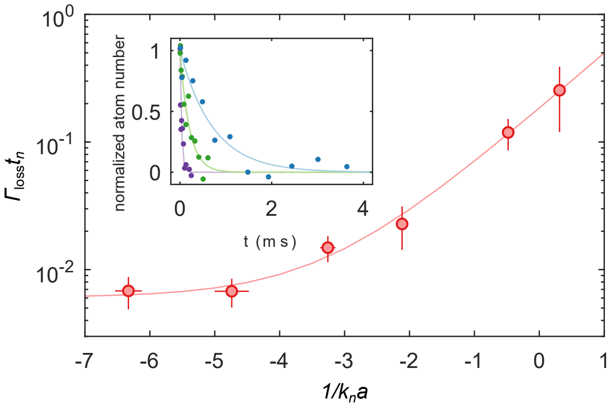

FIG. S3. Loss rate of the impurity state as a function of inverse interaction strength. The inset shows selected data and fits for $1/k_n a = -4.7$ (blue), -2.1 (green), and -0.48 (purple). The data have been scaled with the initial and final atom numbers. The main panel shows the obtained loss rates and an empirical fit. The horizontal error bars are due to statistical uncertainty of the atom number and fitting errors from trap frequency measurements. The vertical error bars additionally contain propagated fitting errors from impurity lifetime measurements.

system [4, 6]. At unitarity, the loss rate is comparable to loss rates observed for Bose polarons in a ^{40}K^{87}Rb mixture. However, at intermediate interactions, it is interesting to note that the rate is significantly larger in the ^{39}K system. This difference in loss rates in the two different atomic systems is also found when comparing three-body loss rates of thermal KRb mixtures [7, 8] to single-component thermal ^{39}K [9–11]. We therefore conclude that this difference is primarily a consequence of the three-body loss rates of the individual atomic systems.

To model the influence of the observed loss rate on the impurity coherence, we perform an empirical fit $\beta_1 + \beta_2 \exp(\beta_3/k_n a)$, with fitting parameters β_i, which is shown in Fig. S3. The fit follows the experimental data well, and we therefore employ this function to calculate Γ_{loss} for arbitrary interactions. To compare with experimental results this loss is included in the theoretically calculated coherence as $C(t) \to C(t)\exp(-\Gamma_{\text{loss}}t)$.

C. Decoherence from magnetic field fluctuations

Experimentally shot-to-shot fluctuations of the magnetic field lead to a further decoherence mechanism. The effect only provides significant decoherence at long times compared to t_n and is therefore mainly relevant for data acquired at weak interactions.

The central part of the experimental procedure is the Ramsey interferometry sequence which is repeated multiple times for each set of experimental parameters. For each repetition, however, the interferometry pulse has a different detuning Δ compared to the bare transition, due to shot-to-shot fluctuations of the magnetic field. This detuning thus provides an additional phase shift $2\pi\Delta \cdot t$, and when the Ramsey interferometry sequence is repeated several times, these varying phase shifts lead to additional decay of the coherence function.

To quantify this effect, we assume that Δ follows a normal distribution, which results in a phase distribution given by $1/\sqrt{2\pi\sigma_{\text{noise}}^2(t)}\exp[-\phi^2/2\sigma_{\text{noise}}^2(t)]$, where $\sigma_{\text{noise}}(t) = 2\pi\Delta_{\text{noise}}t$ and ϕ is the additional phase. The effect of magnetic field fluctuations on the coherence is then obtained by integrating the phase distribution

$$C(t) \rightarrow \frac{C(t)}{\sqrt{2\pi\sigma_{\text{noise}}^2(t)}} \int_{-\infty}^{\infty} \exp(-i\phi)\exp[-\phi^2/2\sigma_{\text{noise}}^2(t)]d\phi. \qquad \text{(S18)}$$

To obtain the magnitude of Δ_{noise}, we have performed Ramsey interferometry measurements at weak interactions $1/k_n a = -5$. Here, decoherence from higher-order impurity dynamics is negligible, and the loss of coherence is thus determined by the inhomogeneous density distribution in the trap, finite impurity lifetime, and decoherence due to magnetic field fluctuations. The observed coherence amplitude is shown in Fig. S4. We perform a fit according to Eq. (S18) with Δ_{noise} as a fitting parameter and obtain $\Delta_{\text{noise}} = 1.8(1)\,\text{kHz}$. This effects is included in the theoretical results at all interaction strengths.

SIV. IMPURITY FRACTION

The experiment is based on interferometric measurements using a Ramsey-type sequence. To obtain a low population of the impurity state we retain the Bloch vector close to the north pole. The impurity fraction is calibrated through initial Rabi measurements using thermal atoms. A $\pi/7$ pulse is chosen, corresponding to $\sim 5\%$ population in the impurity state. Even though this fraction is low the finite amount of impurities may give rise to interactions between them. It is therefore

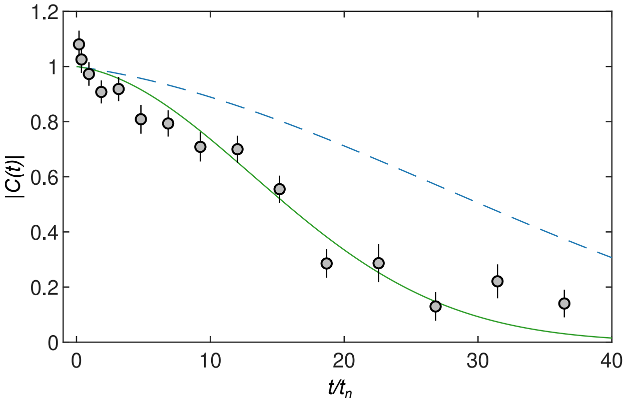

FIG. S4. Coherence amplitude at inverse interaction strength $1/k_n a = -5$. The dashed blue line shows the expected amplitude due to the inhomogeneous density distribution and the effect of finite impurity lifetime. The green line is a fit including shot-to-shot fluctuations in the magnetic field yielding $\Delta_{\mathrm{noise}} = 1.8(1)\,\mathrm{kHz}$. The error bars are 1σ confidence intervals of the fitted values.

important to examine if such impurity-impurity interactions influence the experiment.

To investigate this, additional measurements of the coherence were performed at $1/k_n a = -1$ for 5%, 15% and 20% impurity fraction of the total atom number. However, no significant change in coherence amplitude or phase was observed and therefore a fraction of 5% was chosen for the experiments presented in the main manuscript. A similar investigation of the impurity fraction for the spectral response of the Bose polaron was previously performed in this system [4]. In that case, no significant effect was observed up to 25% impurity fraction and 10% were chosen for those spectroscopic measurements.

SV. EXPERIMENTAL DATA ANALYSIS

In this section the main elements of the data analysis are presented. They consist of the normalization of the coherence amplitude, a discussion of the coherence amplitude and phase evolution, the extraction of the boundaries between the dynamical regimes of impurity dynamics, and the calculation of the instantaneous energy.

A. Experimental normalization of coherence amplitude

At weak interactions, we observe that the atom number loss from the BEC is consistent with three-body recombination between one impurity atom and two medium atoms. However, towards stronger interactions, we observe an increased loss, which is likely due to higher-order losses under these conditions. This hinders a simple conversion between the amplitude of the BEC atom number oscillations and the coherence amplitude, since a new proportionality factor is required at each interactions strength.

Instead, we employ the general short-time model of Eq. (S13). For each data set, we fit the measured coherence amplitude with Eq. (S13) within $\sim 10\,\mu\mathrm{s}$ and obtain the initial amplitude $\mathscr{A}(0)$, which is used to scale the measured coherence amplitude. Note that this normalization procedure does not influence the coherence phase φ_C or relative amplitudes $|C(t')/C(t)|$.

B. Coherence amplitude and phase evolution

The three data sets presented in the main manuscript exhibit vastly different dynamical behavior. Here, we elaborate these differences and present the data side by side for a more direct comparison.

In Fig. S5 the coherence amplitude (top row) and phase evolution (bottom row) for the three interaction strengths discussed in the main manuscript are shown on logarithmic axes. For weak interactions (a-b) the transition from two-body universal to weak coupling dynamics occurs at very short times causing the data to exhibit weak coupling dynamics for a long interval of evolution times until the transition to many-body dynamics. Beyond this transition the coherence continues agreeing with the diagrammatic description, exhibiting many-body behavior which is most pronounced for the coherence amplitude. At intermediate interactions (c-d) the data initially displays clear signs of universal dynamics. Subsequently, the evolution slows down and the data connects with the weak coupling dynamics. However, this behavior coincides with the transition to the many-body regime, indicating that the smooth transitions between regimes cannot be distinguished when they occur at similar evolution times. Finally, the data at unitarity (e-f) shows clear agreement with the universal prediction before the transition to the regime of many-body dynamics. Subsequently, it continues to follow the diagrammatic description, showing clear many-body behavior which is again most visible for the coherence amplitude.

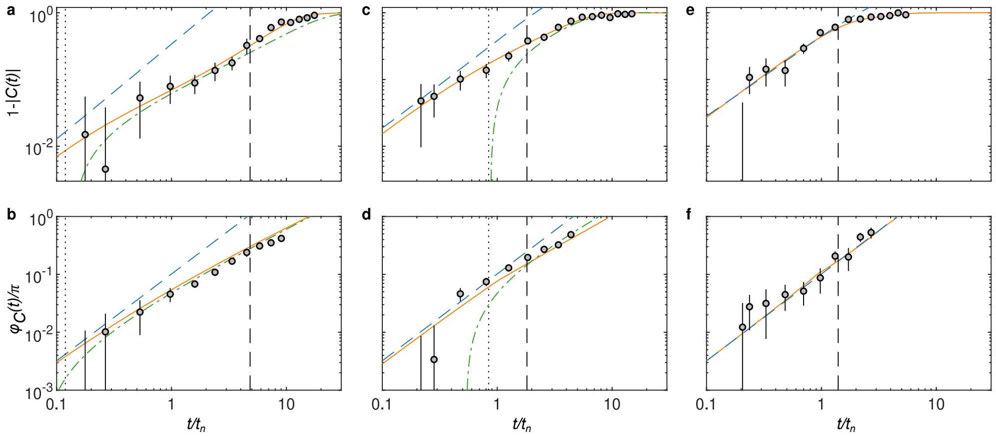

FIG. S5. Coherence amplitude and phase evolution at various interaction strengths. Dynamical evolution at (a-b) $1/k_na = -2$, (c-d) $1/k_na = -0.77$, and (e-f) $1/k_na = 0.01$. The theoretical prediction for two-body universal and two-body weak coupling dynamics are shown as a dashed blue and dash-dotted green line, respectively, and the diagrammatic description is given as a solid orange line. A dotted black line indicates the transition between the two-body regimes and a dashed black line indicates the transition to the many-body regime. The error bars are 1σ confidence intervals of the fitted values.

Generally, the amplitudes can be extracted more reliably even at small signal-to-noise ratio when the phase determination fails.

C. Experimental determination of the dynamical transitions

In Fig. 1 (main manuscript) three distinct regions of dynamical impurity behavior are identified and the boundaries between these regions are shown to agree with the experiment. Here we describe how the displayed data points are obtained experimentally.

The two-body universal and weak-coupling regions can be described by the general two-body short-time equation (S13), while the third region is dominated by many-body physics. For the data at $|1/k_na| \geq 1.5$ the general two-body expression Eq. (S13) fails to agree with the data for times $t \geq 4t_n$, which indicates that many-body physics starts to dominate the evolution of the coherence. This motivates the following criterion, which is applied to the data sets with $|1/k_na| \geq 1.5$: The data point at the shortest time which is more than 2 standard errors away from the result of Eq. (S13) is identified. The onset of many-body physics then corresponds to the time between this and the previous data point as shown in Fig. S1 (orange points). Due to this procedure, the onset and its uncertainty is limited by the experimental resolution.

At unitarity, we investigate when the general two-body expression fails to reproduce the data in a similar manner. We apply the same criterion to the data shown in Fig. 4 of the main manuscript and obtain the data point shown in Fig. S1 (white point).

Finally, we analyse the crossover from two-body universal to two-body weak coupling behavior for all data sets with $|1/k_n a| > 0.5$. To this end, Eq. (S13) is fitted to the measured coherence amplitude and phase evolution for the initial dynamics with the transition time $\tilde{t}_a$ as the only free parameter. The fitted values and their errors are also shown in Fig. S1 (blue points). Note that some of the data sets do not include data points below the extracted value $\tilde{t}_a$. The term dependent on t_a in Eq. (S13), however, modifies the shape of the curve for times far beyond the time t_a itself, allowing an extraction of this time.

D. Instantaneous energy

Based on the measured phase of the coherence function, the instantaneous energy of the impurity can be calculated as $E(t) = -\hbar d\varphi_C/dt$. In the mean-field regime, the system equilibrates fast, causing the observed phase evolution to be linear, thus reproducing the constant mean-field energy. For strong interactions, however, the equilibration of the system can be resolved while the impurity state evolves dynamically. The slope of the phase evolution is extracted by piecewise linear fitting to the data in overlapping bins of 4 points, which yields the instantaneous energy and its error. This is shown in Fig. 4b (main manuscript) for the data set obtained at unitarity in good agreement with the time derivative of the ladder approximation theory. Furthermore, the expected polaron energy is plotted based on previously reported experimental results [6].

---

[1] Nielsen, K. K., Ardila, L. A. P., Bruun, G. M. & Pohl, T. Critical slowdown of non-equilibrium polaron dynamics. *New Journal of Physics* **21**, 043014 (2019).

[2] Braaten, E., Kang, D. & Platter, L. Short-time operator product expansion for rf spectroscopy of a strongly interacting Fermi gas. *Phys. Rev. Lett.* **104**, 223004 (2010).

[3] Rath, S. P. & Schmidt, R. Field-theoretical study of the Bose polaron. *Phys. Rev. A* **88**, 053632 (2013).

[4] Jørgensen, N. B. *et al.* Observation of attractive and repulsive polarons in a Bose-Einstein condensate. *Phys. Rev. Lett.* **117**, 055302 (2016).

[5] Hu, M.-G. *et al.* Bose polarons in the strongly interacting regime. *Phys. Rev. Lett.* **117**, 055301 (2016).

[6] Peña Ardila, L. A. *et al.* Analyzing a Bose polaron across resonant interactions. *Phys. Rev. A* **99**, 063607 (2019).

[7] Bloom, R. S., Hu, M.-G., Cumby, T. D. & Jin, D. S. Tests of universal three-body physics in an ultracold Bose-Fermi mixture. *Phys. Rev. Lett.* **111**, 105301 (2013).

[8] Wacker, L. J. *et al.* Universal three-body physics in ultracold KRb mixtures. *Phys. Rev. Lett.* **117**, 163201 (2016).

[9] Zaccanti, M. *et al.* Observation of an Efimov spectrum in an atomic system. *Nat. Phys.* **5**, 586–591 (2009).

[10] Roy, S. *et al.* Test of the universality of the three-body Efimov parameter at narrow Feshbach resonances. *Phys. Rev. Lett.* **111**, 053202 (2013).

[11] Wacker, L. J. *et al.* Temperature dependence of an Efimov resonance in ^{39}K. *Phys. Rev. A* **98**, 052706 (2018).

3.6 Initial dynamics of quantum impurities in a Bose-Einstein condensate

In the previous section, a publication was presented entailing the first experimental evidence of impurity dynamics in a Bose-Einstein condensate [84]. Intriguingly, the dynamical evolution was observed to exhibit three distinct regimes depending on the evolution time and the interaction strength between the impurity state and the medium state. The following paper [85] expands this work with additional analyses of the initial two-body dynamics using the same data sets. Due to an improved calibration of the imaging system, slight differences appear between the data shown in Ref. [84] and Ref. [85].

3.6.1 Results

The initial dynamics of the impurity evolution is governed by two-body scattering between the impurity state and the medium state. Though no exact solution exists for all evolution times, the short-time dynamical behavior can be described analytically with a single equation. This is possible using the Fourier transform of the high-frequency tail of the spectral function, as discussed in Sec. 3.4. In the following paper [85], this general two-body model is compared with initial observations at weak and unitary interaction strengths. Excellent agreement is obtained between theory and experimental data, which provides a benchmark of the theoretical model. Furthermore, the clear agreement consolidates using the two limits of the general two-body prediction to identify the regimes of universal and weak coupling dynamics in the observed evolution of the impurity state.

The transition from the two-body universal to the two-body weak coupling regime is moreover investigated. The transition time is obtained using a model-dependent fit in good agreement with the predicted value.

Importantly, this fit is shown to be capable of extracting a value and an error, even when they are small compared to the relevant dynamical timescale t_n.

Finally, the functional behavior of the two regimes is investigated by fitting a power law to the observed coherence amplitude which allows extracting a characteristic exponent and timescale. At weak interaction strengths, these agree with predicted values of weak coupling dynamics. For increasing interaction strength, the fitted exponent and timescale gradually transform and eventually connect with the values of universal dynamics at unitarity.

3.6.2 Outlook

The following publication [85] uses an exact description of the high-frequency part of the impurity spectral function to predict short-time dynamics. This model is an effective tool for characterizing the continuum of excited states, which has recently been employed in similar theoretical and experimental investigations in ultracold gases.

The analytic description of the high-frequency tail was first presented in the context of rf spectroscopy in a Fermi gas [87]. Here, it was used to link the rf response to a quantity known as the two-body contact [88], which qualitatively characterizes the probability of fermions with different spins to be very close together. Subsequently, two experimental studies measured this two-body contact in a Fermi gas [89, 90].

The two-body contact was modelled for bosonic gases in Ref. [91], which additionally predicted the existence of a three-body contact for bosons. The bosonic two-body contact has been measured using rf spectroscopy in a Bose-Einstein condensate [92] and interferometrically in a thermal Bose gas [86], which also observed the dynamical evolution of the three-body contact. Recently, the two-body contact of the Bose polaron was measured using rf spectroscopy [70]. An interferometric study of the polaronic contact therefore constitutes an exciting investigation and may even allow the dynamical evolution of the contact to be resolved [93].

3.6.3 Publication

The data sets analyzed in the following publication [85] are the same sets reported in the previous paper [84]. Here, I was part of designing the experiment and acquiring the data. For the results presented in this publication, I furthermore performed the data analysis, created all figures and wrote first drafts of the manuscript.

atoms

MDPI

Article

Initial Dynamics of Quantum Impurities in a Bose–Einstein Condensate

Magnus G. Skou *, Thomas G. Skov, Nils B. Jørgensen and Jan J. Arlt

Center for Complex Quantum Systems, Department of Physics and Astronomy, Aarhus University,
Ny Munkegade 120, DK-8000 Aarhus, Denmark; tg.skov@phys.au.dk (T.G.S.); nilsbyg@hotmail.com (N.B.J.);
arlt@phys.au.dk (J.J.A.)
* Correspondence: magnus.skou@phys.au.dk

Abstract: An impurity immersed in a medium constitutes a canonical scenario applicable in a wide range of fields in physics. Though our understanding has advanced significantly in the past decades, quantum impurities in a bosonic environment are still of considerable theoretical and experimental interest. Here, we discuss the initial dynamics of such impurities, which was recently observed in interferometric experiments. Experimental observations from weak to unitary interactions are presented and compared to a theoretical description. In particular, the transition between two initial dynamical regimes dominated by two-body interactions is analyzed, yielding transition times in clear agreement with the theoretical prediction. Additionally, the distinct time dependence of the coherence amplitude in these regimes is obtained by extracting its power-law exponents. This benchmarks our understanding and suggests new ways of probing dynamical properties of quantum impurities.

Keywords: Bose–Einstein condensates; impurity dynamics; ramsey interferometry; polarons

check for updates

Citation: Skou, M.G.; Skov. T.G.; Jørgensen, N.B.; Arlt, J.J. Initial Dynamics of Quantum Impurities in a Bose–Einstein Condensate. *Atoms* **2021**, *9*, 22. https://doi.org/10.3390/atoms9020022

Academic Editors: Mistakidis Simeon and Artem Volosniev

Received: 26 February 2021
Accepted: 23 March 2021
Published: 27 March 2021

1. Introduction

The behavior of interacting quantum impurities is a problem of significant scientific and technological importance. Initial theoretical studies by Landau and Pekar [1] showed that a crystal lattice dresses electrons to form quasiparticles coined polarons. This intuitive model is highly successful and now serves as a basis for understanding complex condensed matter systems [2]. The concept of polarons is thus central for important technologies such as organic semiconductors [3] and high-temperature superconductors [4].

The initial dynamics of an impurity is especially intriguing. It sheds light on the intrinsic link between two-body and many-body correlations, and is key to understanding the eventual formation of a polaron. Due to the fast evolution times in most materials, this evolution has eluded observation until recently. With the advent of quantum gases, this is no longer the case since their low densities allow for long interrogation times in pure and controllable environments. Based on these systems, the spectral response and dynamical evolution of an impurity in a Fermi gas have been explored in great theoretical and experimental detail [5–13]. The mobile Bose polaron, which resembles the solid-state problem closely, has been studied spectroscopically [14–17] and its behavior has been investigated in a one-dimensional Bose gas [18,19]. However, the formation dynamics of the Bose polaron in a three-dimensional gas has remained unclear.

Here we present recent experiments, which succeed in investigating the dynamics of impurities in a Bose–Einstein condensate (BEC). This evolution of the impurities can be resolved using an interferometric sequence. The first pulse in this sequence creates an imbalanced superposition state, which evolves under the influence of interactions in the system. The second pulse then allows a measurement of the coherence between the initial state and the evolved impurity state [20]. The dynamics of the impurity can be separated into three regimes, as illustrated in Figure 1, depending on the interaction strength and the evolution time. The initial dynamics at all interaction strengths is governed by two-body scattering between the impurity and the condensate. For short times, the two-body scattering is unitarity-limited causing the coherence to evolve universally [21]. For weak interactions, this is followed by a regime of two-body weak coupling dynamics which depends on the scattering length between the impurity state and medium state. For longer times, the dynamical behavior transitions into a regime where many-body correlations govern the evolution. For strong interactions, this regime is entered directly from universal dynamics.

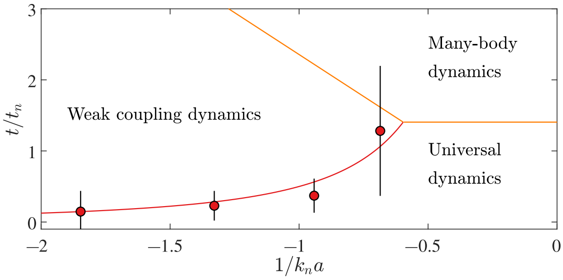

Figure 1. Regimes of impurity dynamics. Characteristic regimes of impurity dynamics as a function of the inverse interaction strength $1/k_n a$ (see text) and the evolution time t/t_n (see text). Solid lines indicate predicted transitions between the dynamical regimes. Red data points are experimentally extracted transition times and errors correspond to fit uncertainties. A similar figure was presented in Ref. [20].

This dynamical evolution was initially investigated in Ref. [20] where all three regimes were observed. Furthermore, the transition times between the regimes were obtained showing clear agreement with theoretical predictions. In this paper, we extend the analysis of the experimental observations to provide a deeper understanding of the two regimes of universal and weak coupling dynamics illustrated in Figure 1. Specifically, we discuss the transition time between them and consider the functional behavior of the coherence in the two regimes.

The paper is structured as follows. In Section 2, the experiment is briefly presented including the interferometric sequence. This is followed by the discussion of a theoretical model in Section 3. In Section 4, this model is compared with experimental observations of the coherence amplitude and phase evolution for weak and unitary interactions. The transition between the two regimes is discussed in Section 5. Finally, in Section 6 the dependence of the dynamical evolution on interaction strength is presented.

2. Experimental Details

The experiment was performed using a quantum gas of ^{39}K. The production of ^{39}K BECs has been presented in detail in Refs. [14,22] and only the relevant steps for investigating impurity dynamics are outlined here.

The experiments are based on a ^{39}K BEC in the hyperfine state $|F=1, m_F=-1\rangle$ held in an optical dipole potential with an average condensate density of $n_\mathrm{B} = 0.9 \times 10^{14}\ \mathrm{cm}^{-3}$. This determines the system energy scale $E_n = \hbar^2 k_n^2/2m$ through the wave number $k_n = (6\pi^2 n_B)^{1/3}$ and importantly sets the relevant timescale $t_n = \hbar/E_n = 4\,\mu\mathrm{s}$. We employ a second hyperfine state $|F=1, m_F=0\rangle$ as the impurity state. The interaction strength between the two states is characterized by the dimensionless parameter $1/k_n a$, where a is the interstate scattering length. This scattering length can be tuned by the magnetic field via a Feshbach resonance located at 113.8 G [23,24]. The medium scattering length is $a_B \approx 9a_0$, where a_0 is the Bohr radius, and is approximately constant for the applied magnetic fields

An interferometric sequence consisting of two radio-frequency (rf) pulses is employed, which allows us to populate an impurity state and probe the subsequent dynamics. Similar interferometric investigations have previously explored impurity dynamics in a Fermi gas [8,9] and motional coherence of fixed impurities in a BEC [25,26]. The rf pulses are resonant with the atomic transition and their short duration of 0.5 µs allows the dynamics to be well resolved. The first rf pulse quenches the system into a superposition of the impurity state and the medium state corresponding to a ∼5% population in the former, which ensures vanishing interaction between the impurites [20]. The system then evolves for a variable time t, in which the phase of the coherence advances and the coherence amplitude decays due to interactions between the two states. Finally, a second rf pulse probes the system with a variable phase φ. Subsequently, the atoms are held in the dipole trap for an additional 2 ms where three-body losses remove two medium atoms for each impurity. Thus, only medium atoms remain whose number is inversely proportional to the number of impurity atoms after the second rf pulse. After free expansion the remaining number of the medium state atoms is measured through absorption imaging.

This resulting atom number depends sinusoidally on the probe phase and for each evolution time t we perform a fit $N(\varphi) = N_0 - \mathcal{A}\cos(\varphi - \varphi_C)$. Here, the amplitude $\mathcal{A}$ corresponds to the extent to which the coherence is preserved and φ_C corresponds to the phase acquired during the evolution time t. Thus, we obtain the amplitude $|C(t)| = |\mathcal{A}(t)/\mathcal{A}(0)|$ and the phase φ_C of the coherence for each chosen interaction strength and evolution time. Example measurements of the coherence amplitude and phase are shown in Figure 2 for weak and unitary interactions (Slight differences in the data with respect to Ref. [20] arise due to an improved calibration of the imaging system.). These measurements clearly display how the coherence of the system evolves as time progresses between the two rf pulses.

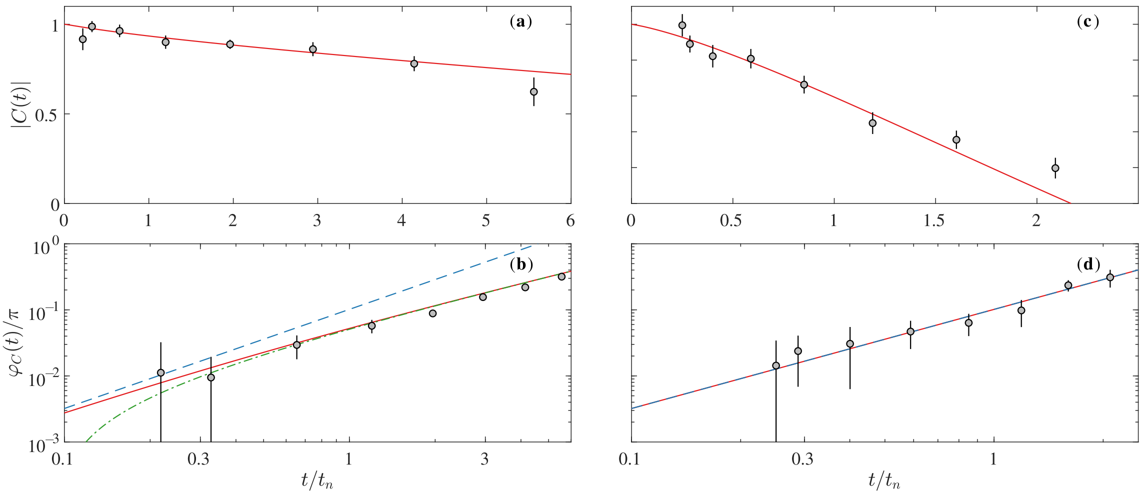

Figure 2. Two-body dynamics at weak and unitary interaction strengths. The coherence amplitude (top row) and phase evolution (bottom row) at $1/k_n a = -1.8$ (**a**,**b**) and $1/k_n a = 0.01$ (**c**,**d**). The corresponding data were previously presented in Ref. [20]. Equation (1) is shown as a solid red line and the two limits in Equation (2) are shown as a dashed blue line and a dash-dotted green line for the universal and the weak coupling dynamics, respectively. Note that the universal description coincides with the general two-body model in panel (**d**). The errors correspond to fit uncertainties.

3. Two-Body Regimes of Dynamical Evolution

In the following section we briefly outline the theoretical description of the dynamical regimes which we compare with our experimental results. A short-time theoretical prediction can be obtained from the spectral function of the impurity. This describes the impurity in the frequency-domain and generally contains a polaron ground state and a continuum of excited states. Though the exact spectral function at arbitrary interaction strength has no general solution, the tail of excited states at high frequencies has previously been investigated in detail [27]. Due to the intrinsic link between frequency-domain and time-domain behavior, the Fourier transform of this high-frequency solution yields the coherence for the initial two-body dynamics. For low medium-medium scattering length, it can be expressed as [20]

$$C(t) \simeq 1 - i\frac{E_{\mathrm{mf}}t}{\hbar} + \frac{2}{3\pi}(k_n|a|)^3\left[1 - \frac{2}{\sqrt{\pi}}\mathrm{e}^{it/t_a}\Gamma\left(\frac{3}{2}, i\frac{t}{t_a}\right)\right], \tag{1}$$

where Γ is the incomplete gamma function, $E_{\mathrm{mf}} = 4\pi\hbar^2 n_{\mathrm{B}} a/m$ is the mean-field energy and $t_a = ma^2/\hbar$ is the timescale set by the medium-impurity scattering length a. The coherence amplitude and phase can be examined using the coherence in the small-angle approximation. Thus, to the lowest order, the experimentally measured amplitude and phase correspond to the real and imaginary part of Equation (1).

Remarkably, this two-body prediction is exact for any interaction strength from weak to strong interactions [20]. Furthermore, it is possible to simplify Equation (1) in the following limits

$$C(t) = \begin{cases} 1 - (1-i)\frac{16}{9\pi^{3/2}}\left(\frac{t}{t_n}\right)^{3/2} & t \ll t_a \\ 1 - iE_{\mathrm{mf}}t/\hbar - (1+i)\left(\frac{t}{t_{\mathrm{w}}}\right)^{1/2} & t \gg t_a \end{cases} \tag{2}$$

where $t_{\mathrm{w}} = m/32\pi\hbar n_{\mathrm{B}}^2 a^4$. The long-time limit of the equation is valid to second order in the impurity-medium scattering length a, and it can be extended to include a third-order correction [20]. Furthermore, it clearly demonstrates two distinct regimes. At short times $t \ll t_a$ the high-frequency scattering is limited by the density and the coherence evolves with an interaction independent timescale t_n and an exponent of $3/2$. For longer times $t \gg t_a$, this transitions into weak coupling dynamics marked by the appearance of the mean-field energy, the interaction dependent timescale t_{w}, and the exponent $1/2$.

These power laws reflect the behavior of the scattering cross section $\sigma(k) = 4\pi a^2/[1 + (ka)^2]$ in the two regimes [20]. In a simple picture, it governs the collision rate, which we assume to equal the rate of decoherence $\dot{C}(t) \sim -n_{\mathrm{B}}\sigma v$. At a given time t during the evolution after the first rf pulse, the characteristic energy associated with decoherence is $E \sim \hbar/t$, which sets the wave number $k \sim \sqrt{m/\hbar t}$ and collisional velocity $v \sim \sqrt{\hbar/mt}$. For short times $t \ll t_a$, the cross section is unitary-limited $\sigma \sim 1/k^2 \sim \hbar t/m$. By integrating the corresponding rate of decoherence we obtain $C(t) \sim (t/t_n)^{3/2}$, which precisely reflects the universal limit of Equation (2). In contrast, for longer times $t \gg t_a$ the cross section is dominated by the scattering length as $\sigma \sim a^2$. Integrating the decoherence rate here yields the weak coupling limit $C(t) \sim (t/t_{\mathrm{w}})^{1/2}$. The timescale t_a is therefore key in describing which regime governs the dynamical evolution of the system.

4. Coherence Amplitude and Phase Evolution

Based on the experiment described in Section 2, it is possible to observe the evolution of an impurity state by monitoring the coherence amplitude $|C|$ and phase φ_C. Here we compare such measurements with the theoretical prediction from Section 3. Examples of measured coherence amplitude and phase are shown in Figure 2 for weak and resonant interactions with the general two-body description (Equation (1)) for all panels and with its limits (Equation (2)) for the phase.

For both data sets, the coherence amplitude decreases as function of evolution time, driven by the dynamical scattering events. This shows that the impurity state evolves and loses coherence with the initial state (To compare the experimental observations with this prediction, the coherence amplitude is normalized by fitting Equation (1) with an overall amplitude within t_n.) at a rate which increases for large interaction strengths as expected.

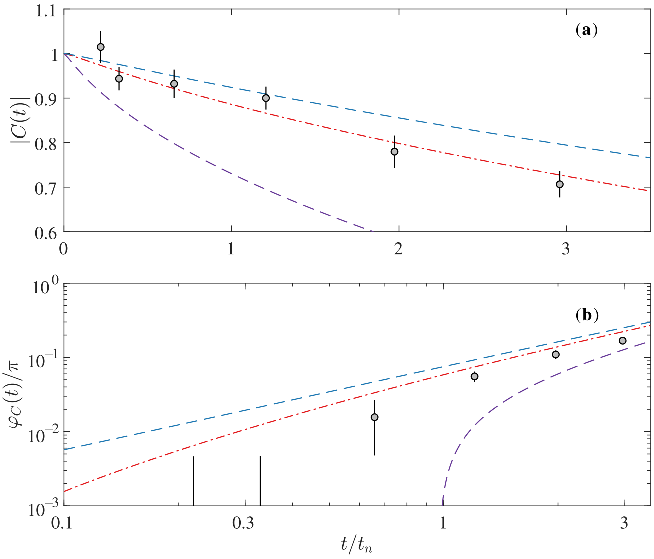

Figure 3. Transition from universal to weak coupling dynamics. (**a**) The coherence amplitude and (**b**) phase evolution at $1/k_n a = -1.3$ (circles) with Equation (1) as a dash-dotted line for its fitted value $t_a = 0.2t_n$ (red) and as dashed lines using two additional values $0.05t_n$ (purple) and $0.5t_n$ (blue). The errors correspond to fit uncertainties.

The coherence amplitude in the upper panels of Figure 2 is affected by additional decoherence processes which all contribute to its gradual decay. To accurately model the experiment, we therefore include effects stemming from the inhomogeneous density distribution, the lifetime of the impurity and shot-to-shot magnetic field fluctuations in our theoretical description. The dephasing due to the inhomogeneous density distribution is accounted for by integration of the coherence over the density distribution of the BEC. This is modeled in the Thomas–Fermi limit using a parabolic density profile. The lifetime of the impurity due to recombination was measured independently and included by multiplying the coherence with an exponential decay. The lifetime ranges from $\sim 7t_n$ at unitarity to $\sim 42t_n$ at weak interaction strengths. The shot-to-shot magnetic field fluctuations were also measured independently and incorporated in the theoretical description of the coherence. This was achieved by multiplying the coherence with the integrated distribution of phases caused by the slight differences in the magnetic field at each experimental repetition. Since the temperature of the cloud was $\sim 50\,\mathrm{nK}$, the corresponding thermal timescale $\hbar/k_\mathrm{B}T \sim 38t_n$ is beyond the accessible regime of impurity dynamics and thus thermal effects are negligible. The resulting two-body prediction is illustrated in Figure 2 and clearly agrees with the data for short times. Since no fitting parameters are employed, the excellent agreement of the prediction and observations highlights that the theory captures the dynamical behavior of the system exceedingly well.

The lower panels of Figure 2 show the evolution of the coherence phase as a function of time, where a faster evolution is observed for larger interaction strengths. Since the experimental decoherence mechanisms primarily influence the coherence amplitude, the phase is better suited to observe the power-law behavior of the coherence evolution. It is therefore plotted in a double logarithmic fashion (Note that the coherence phase cannot be reliably extracted for long evolution times due to the vanishing coherence amplitude.). The imaginary part of Equation (1) is also shown in the lower panels of Figure 2 in good agreement with the observations. To gain further insight, we show the limits of Equation (2) as well. For weak interactions (Figure 2b) the transition from two-body universal dynamics to weak coupling dynamics occurs almost immediately and the $\sim t^{1/2}$ limit of Equation (2) captures the entire observed phase evolution. At unitarity, the universal dynamics extends to much longer evolution times and thus the $\sim t^{3/2}$ limit of Equation (2) coincides with Equation (1) and agrees with the experimental observations.

In general, it is remarkable how well the measured coherence amplitude and phase at short times agree with Equation (1) considering the wide span of interaction strengths from weak to unitary. Moreover, our result shows that the limits of Equation (2) are valid and allow a clear distinction of the two regimes. This consolidates our understanding of the initial two-body dynamics and validates the theoretical prediction.

5. Transition from Universal to Weak Coupling Dynamics

Equation (2) shows that the transition between the universal and the weak coupling regime is given by t_a, which sets an important timescale of the dynamics and motivates its experimental investigation. In the following we show that the transition time can be extracted from the observations with a model-dependent fit and discuss the fitted results as function of interaction strength.

The transition time t_a appears in the general short-time prediction Equation (1) as an interaction dependent timescale. We therefore fit Equation (1) simultaneously to the coherence amplitude and phase evolution with t_a as the only free parameter to extract the transition between the two regimes. Importantly, we only fit the initial data of each set since Equation (1) is only valid in the limit of short times. The fitted timescales at four interaction strengths are shown in Figure 1a together with the predicted transition times between the dynamical regimes. The extracted transition time increases for stronger interactions indicating an extended evolution time of universal dynamics. Moreover, the timescale is in clear agreement with the predicted value of t_a.

Remarkably, the fitted value and its error are small compared with the dynamical timescale t_n. Since the duration of the probing pulses is $0.5\,\mu\text{s} \sim 0.1 t_n$, it is not immediately clear that such small timescales can be extracted experimentally. To illustrate the feasibility, a fit at $1/k_n a = -1.3$ is shown in Figure 3, which yields an extracted transition time of $0.2(2)t_n$ in agreement with the predicted value of $t_a = 0.3t_n$. Additionally, two lines are shown where $t_a = 0.05t_n$ and $0.5t_n$. This figure thus clarifies that t_a affects the functional shape of the coherence at times much larger than its own value. Therefore, even small differences in t_a cause large discrepancies when compared with the experimental observation, which is most pronounced for the coherence amplitude Figure 3a.

We thus demonstrate that a transition time can be extracted experimentally in agreement with theoretical predictions. For sufficiently large interaction strengths $|1/k_n a| \lesssim 0.5$, a transition to weak coupling dynamics is not observable, since the many-body regime is entered directly.

6. Two-Body Exponent and Time Constant

The limits given by Equation (2) show that the universal and weak coupling regime display distinctively different functional behavior corresponding to power-law exponents $3/2$ and $1/2$, respectively. We now turn our attention to the investigation of this functional difference by fitting such a power law to the coherence amplitude and observing its dependence on the interaction strength.

The two limits of the two-body prediction in Equation (2) are especially simple for the coherence amplitude and follow the form $1 - (t/t_c)^\beta$. For weak coupling dynamics $\beta = 1/2$ and t_c is interaction dependent whereas for universal dynamics $\beta = 3/2$ and t_c is constant. By fitting a power law to the coherence amplitude within the regimes of two-body dynamics, the fitted values of β and t_c can indicate the functional behavior at the chosen interaction strength.

The fitted exponents and time constants are shown in Figure 4 together with the weak coupling and universal values. For low interaction strengths β agrees with the prediction of weak coupling dynamics. At stronger interactions it slowly increases and reaches $3/2$ at unitarity in agreement with the universal prediction. The fitted time constant t_c initially decreases for increasing interaction strength and qualitatively follows the behavior of the predicted timescale t_w of weak coupling dynamics. However, for strong interaction strengths, where t_w diverges, t_c remains finite and connects with the universal value of $\sim 2.1 t_n$. The error bars correspond to symmetric fit uncertainties and the apparent asymmetry is due to the logarithmic scale.

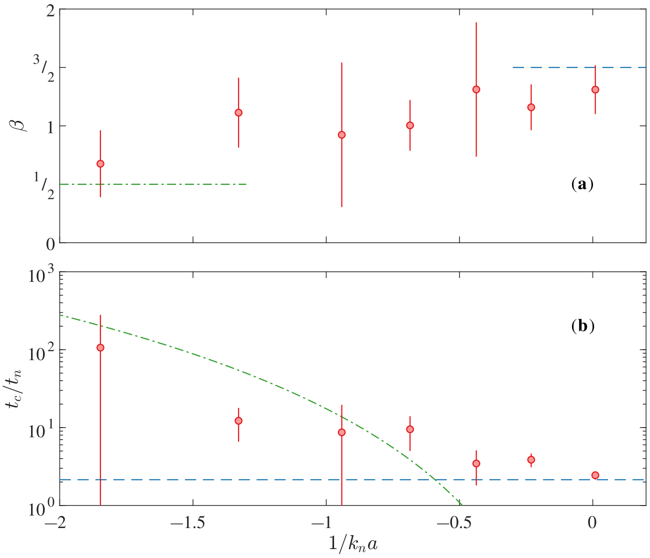

Figure 4. Characteristic exponent and time constant. By fitting a power law $1-(t/t_c)^\beta$ to the coherence amplitude, we obtain the characteristic exponent (**a**) and time constant (**b**) at various interaction strengths. The theoretically predicted exponent and time constants for universal and weak coupling dynamics are shown as a dashed blue line and a dash-dotted green line, respectively. The errors correspond to fit uncertainties.

The experimental observations in the transition region between weak and unitary interactions are influenced by the behavior of both two-body regimes. Therefore, the specific values of β and t_c bear no physical meaning and are a consequence of fitting a single time dependence to the data when both weak coupling and universal dynamics are present. Nonetheless, at weak and unitary interactions the fitted power law is dominated by either one of the two-body regimes and we observe a smooth connection between the two in the transition region.

7. Conclusions

The results presented here provide a detailed investigation of the initial two-body dynamics of a quantum impurity in a BEC. The impurity dynamics has previously been studied [20], and here we have extended the analysis of the initial universal and subsequent weak coupling dynamics and the transition between them.

An interferometric sequence was used to measure the coherence of the system quenched into a superposition of an impurity state and a medium state. The evolution of the coherence was predicted by a rigorous short-time model, which showed a universal and a weak coupling regime with distinct exponents and timescales. A direct comparison between the experimental observations and the two-body theoretical prediction confirmed the validity of the model.

The transition between the two regimes was analyzed at four interaction strengths yielding transition times in clear agreement with the theoretical prediction as shown in Figure 1. Additionally, the transition was investigated by fitting a power law to the coherence amplitude, revealing how the exponent and time constant change from weak coupling to universal dynamics for increasing interaction strength.

These investigations improve our understanding of the fundamental properties of quasiparticles. By comparing interferometic observations at long evolution times to earlier spectroscopic results [14–17] a complete model for the Bose polaron in both time and frequency-domain can be obtained. Furthermore, the experimental methods may be expanded to help elucidate exotic phenomena such as transport processes [28,29] or dynamical formation of bipolarons [30].

Author Contributions: Conceptualization, M.G.S., T.G.S., N.B.J. and J.J.A.; methodology, M.G.S.; software, M.G.S.; validation, M.G.S., T.G.S., N.B.J. and J.J.A.; formal analysis, M.G.S.; investigation, M.G.S., T.G.S., N.B.J. and J.J.A.; resources, J.J.A.; data curation, M.G.S.; writing—original draft preparation, M.G.S.; writing—review and editing, M.G.S., T.G.S., N.B.J. and J.J.A.; visualization, M.G.S.; supervision, J.J.A.; project administration, J.J.A.; funding acquisition, J.J.A. All authors have read and agreed to the published version of the manuscript.

Funding: This work has been supported by the Danish National Research Foundation through the Center of Excellence “CCQ” (Grant agreement no.: DNRF156).

Institutional Review Board Statement: Not applicable.

Informed Consent Statement: Not applicable.

Data Availability Statement: The data that support the findings of this study are available from the corresponding author upon reasonable request.

Acknowledgments: We thank K. K. Nielsen, A. Camacho-Guardian, T. Pohl, and G. M. Bruun for helpful discussions.

Conflicts of Interest: The authors declare no conflict of interest.

References

1. Landau, L.D.; Pekar, S.I. Effective mass of a polaron. *Zh. Eksp. Teor. Fiz.* **1948**, *18*, 419–423.
2. Devreese, J.T.; Alexandrov, A.S. Fröhlich polaron and bipolaron: Recent developments. *Rep. Prog. Phys.* **2009**, *72*, 066501. [CrossRef]
3. Gershenson, M.E.; Podzorov, V.; Morpurgo, A.F. *Colloquium*: Electron. Transp. Single-Cryst. *Org. Rev. Mod. Phys.* **2006**, *78*, 973–989. [CrossRef]
4. Dagotto, E. Correlated electrons in high-temperature superconductors. *Rev. Mod. Phys.* **1994**, *66*, 763–840. [CrossRef]
5. Schirotzek, A.; Wu, C.H.; Sommer, A.; Zwierlein, M.W. Observation of Fermi polarons in a tunable Fermi liquid of ultracold atoms. *Phys. Rev. Lett.* **2009**, *102*, 230402. [CrossRef] [PubMed]
6. Kohstall, C.; Zaccanti, M.; Jag, M.; Trenkwalder, A.; Massignan, P.; Bruun, G.M.; Schreck, F.; Grimm, R. Metastability and coherence of repulsive polarons in a strongly interacting Fermi mixture. *Nature* **2012**, *485*, 615–618. [CrossRef]
7. Koschorreck, M.; Pertot, D.; Vogt, E.; Fröhlich, B.; Feld, M.; Köhl, M. Attractive and repulsive Fermi polarons in two dimensions. *Nature* **2012**, *485*, 619–622. [CrossRef]
8. Cetina, M.; Jag, M.; Lous, R.S.; Walraven, J.T.M.; Grimm, R.; Christensen, R.S.; Bruun, G.M. Decoherence of Impurities in a Fermi Sea of Ultracold Atoms. *Phys. Rev. Lett.* **2015**, *115*, 135302. [CrossRef]
9. Cetina, M.; Jag, M.; Lous, R.S.; Fritsche, I.; Walraven, J.T.; Grimm, R.; Levinsen, J.; Parish, M.M.; Schmidt, R.; Knap, M.; et al. Ultrafast many-body interferometry of impurities coupled to a Fermi sea. *Science* **2016**, *354*, 96–99. [CrossRef] [PubMed]
10. Scazza, F.; Valtolina, G.; Massignan, P.; Recati, A.; Amico, A.; Burchianti, A.; Fort, C.; Inguscio, M.; Zaccanti, M.; Roati, G. Repulsive Fermi Polarons in a Resonant Mixture of Ultracold ^{6}Li Atoms. *Phys. Rev. Lett.* **2017**, *118*, 083602. [CrossRef]
11. Schmidt, R.; Knap, M.; Ivanov, D.A.; You, J.S.; Cetina, M.; Demler, E. Universal many-body response of heavy impurities coupled to a Fermi sea: A review of recent progress. *Rep. Prog. Phys.* **2018**, *81*, 024401. [CrossRef]
12. Yan, Z.; Patel, P.B.; Mukherjee, B.; Fletcher, R.J.; Struck, J.; Zwierlein, M.W. Boiling a Unitary Fermi Liquid. *Phys. Rev. Lett.* **2019**, *122*, 093401. [CrossRef]
13. Darkwah Oppong, N.; Riegger, L.; Bettermann, O.; Höfer, M.; Levinsen, J.; Parish, M.M.; Bloch, I.; Fölling, S. Observation of Coherent Multiorbital Polarons in a Two-Dimensional Fermi Gas. *Phys. Rev. Lett.* **2019**, *122*, 193604. [CrossRef]
14. Jørgensen, N.B.; Wacker, L.; Skalmstang, K.T.; Parish, M.M.; Levinsen, J.; Christensen, R.S.; Bruun, G.M.; Arlt, J.J. Observation of Attractive and Repulsive Polarons in a Bose-Einstein Condensate. *Phys. Rev. Lett.* **2016**, *117*, 055302. [CrossRef] [PubMed]
15. Hu, M.G.; Van de Graaff, M.J.; Kedar, D.; Corson, J.P.; Cornell, E.A.; Jin, D.S. Bose Polarons in the Strongly Interacting Regime. *Phys. Rev. Lett.* **2016**, *117*, 055301. [CrossRef]
16. Peña Ardila, L.A.; Jørgensen, N.B.; Pohl, T.; Giorgini, S.; Bruun, G.M.; Arlt, J.J. Analyzing a Bose polaron across resonant interactions. *Phys. Rev. A* **2019**, *99*, 063607. [CrossRef]

17. Yan, Z.Z.; Ni, Y.; Robens, C.; Zwierlein, M.W. Bose polarons near quantum criticality. *Science* **2020**, *368*, 190–194. [CrossRef] [PubMed]
18. Catani, J.; Lamporesi, G.; Naik, D.; Gring, M.; Inguscio, M.; Minardi, F.; Kantian, A.; Giamarchi, T. Quantum dynamics of impurities in a one-dimensional Bose gas. *Phys. Rev. A* **2012**, *85*, 023623. [CrossRef]
19. Meinert, F.; Knap, M.; Kirilov, E.; Jag-Lauber, K.; Zvonarev, M.B.; Demler, E.; Nägerl, H.C. Bloch oscillations in the absence of a lattice. *Science* **2017**, *356*, 945–948. [CrossRef]
20. Skou, M.G.; Skov, T.G.; Jørgensen, N.B.; Nielsen, K.K.; Camacho-Guardian, A.; Pohl, T.; Bruun, G.M.; Arlt, J.J. Non-equilibrium quantum dynamics and formation of the Bose polaron. *Nat. Phys.* **2021**. [CrossRef]
21. Parish, M.M.; Levinsen, J. Quantum dynamics of impurities coupled to a Fermi sea. *Phys. Rev. B* **2016**, *94*, 184303. [CrossRef]
22. Wacker, L.J.; Jørgensen, N.B.; Birkmose, D.; Winter, N.; Mikkelsen, M.; Sherson, J.; Zinner, N.; Arlt, J.J. Universal Three-Body Physics in Ultracold KRb Mixtures. *Phys. Rev. Lett.* **2016**, *117*, 163201. [CrossRef]
23. Lysebo, M.; Veseth, L. Feshbach resonances and transition rates for cold homonuclear collisions between ^{39}K and ^{41}K atoms. *Phys. Rev. A* **2010**, *81*, 032702. [CrossRef]
24. Tanzi, L.; Cabrera, C.R.; Sanz, J.; Cheiney, P.; Tomza, M.; Tarruell, L. Feshbach resonances in potassium Bose-Bose mixtures. *Phys. Rev. A* **2018**, *98*, 062712. [CrossRef]
25. Scelle, R.; Rentrop, T.; Trautmann, A.; Schuster, T.; Oberthaler, M.K. Motional Coherence of Fermions Immersed in a Bose Gas. *Phys. Rev. Lett.* **2013**, *111*, 070401. [CrossRef] [PubMed]
26. Rentrop, T.; Trautmann, A.; Olivares, F.A.; Jendrzejewski, F.; Komnik, A.; Oberthaler, M.K. Observation of the Phononic Lamb Shift with a Synthetic Vacuum. *Phys. Rev. X* **2016**, *6*, 041041. [CrossRef]
27. Braaten, E.; Kang, D.; Platter, L. Short-Time Operator Product Expansion for rf Spectroscopy of a Strongly Interacting Fermi Gas. *Phys. Rev. Lett.* **2010**, *104*, 223004. [CrossRef]
28. Sommer, A.; Ku, M.; Zwierlein, M.W. Spin transport in polaronic and superfluid Fermi gases. *New J. Phys.* **2011**, *13*, 055009. [CrossRef]
29. Bardon, A.B.; Beattie, S.; Luciuk, C.; Cairncross, W.; Fine, D.; Cheng, N.S.; Edge, G.J.A.; Taylor, E.; Zhang, S.; Trotzky, S.; et al. Transverse Demagnetization Dynamics of a Unitary Fermi Gas. *Science* **2014**, *344*, 722–724. [CrossRef] [PubMed]
30. Camacho-Guardian, A.; Peña Ardila, L.A.; Pohl, T.; Bruun, G.M. Bipolarons in a Bose-Einstein Condensate. *Phys. Rev. Lett.* **2018**, *121*, 013401. [CrossRef]

CHAPTER 4

ENERGY AND TIMESCALES OF THE POLARON

Important properties of the polaron include its energy and dynamical timescales. The shift in the energy of the impurity is caused by interactions with the medium and can be measured both spectroscopically and interferometrically. Interestingly, the interactions lead to the presence of two polaron branches with distinct energies at repulsive interaction strengths. Furthermore, the polaron is marked by the timescales of formation and lifetime of the impurity which, ideally, should be clearly separated to permit investigations of the polaron. To examine the energies and timescales involved in polaron physics, this chapter analyzes interferometric and spectroscopic observations of the Bose polaron.

The chapter is structured as follows. First, the spectroscopic and interferometric experimental approaches are introduced in Sec. 4.1. This is followed by a brief consideration of how impurity dynamics at repulsive interaction strengths is expected to behave in Sec. 4.2. The instantaneous energy of the impurity is then examined in Sec. 4.3, which may be used when comparing interferometrically and spectroscopically measured polaron results. In Sec. 4.4, the timescales of the polaron are introduced and their implications are discussed. Finally, in Sec. 4.2 a publication [94] is presented, which includes the first measurement of impurity dynamics at strong repulsive interactions, a comparison of observed impurity energies from recent investigations and an analysis of the dynamical timescales of the polaron.

4.1 Experimental approaches to study the polaron

The polaron may be investigated in both time- and frequency-domain. Where interferometric measurements reveal the dynamical formation of the polaron [35, 36, 84], spectroscopic observations extract its spectral response [30–33, 37, 38, 70]. Properties that influence the results of both approaches include the polaron energy, the quasiparticle residue [95, 96] and furthermore the timescales of polaron formation and loss. It is thus imperative to understand the experimental methods and how they differ in investigating polaronic physics.

The mobile polaron in a BEC was first observed using rf spectroscopy [37, 38]. As discussed in Sec. 2.4, these investigations measured how the resonance frequency between a non-interacting and an interacting impurity state changed as a function of the interaction strength between the impurity and the medium. Spectroscopic methods generally excel by using long pulses with a narrow frequency width to probe the spectral response of the impurity. Since the energy spectrum of the Bose polaron scales with E_n, previous investigations chose rf pulse lengths which yielded an experimental resolution of $\sim 0.1E_n$ [37, 38, 70]. Thus, the spectral response of the impurity was well-resolved, and an attractive and repulsive polaron branch were identified.

Measurements of impurity dynamics using an interferometric procedure were presented in Chap. 3. In these investigations, a Ramsey-like sequence was employed, consisting of two rf pulses with a variable evolution time in between. Compared to the relevant timescale t_n, the applied rf pulses had a short $\sim 0.1t_n$ duration and was thereby capable of resolving the evolution of the impurity state well. This allowed observations of a transition from initial two-body dynamics to a regime governed by many-body correlations wherein the polaron is formed.

The loss of the impurity through three-body collisions is also important to consider, since these losses may limit the equilibration of the polaron. To investigate this, lifetime measurements were conducted in Refs. [38, 84] by observing the population in the interacting impurity state either directly or indirectly as a function of time. The decay rate of the impurity was extracted from these measurement, which revealed fast losses in the unitary regime and lifetimes on the order of $10t_n$. These observations therefore permit a quantitative analysis of the timescales of polaron dynamics.

4.2 Impurity dynamics at repulsive interaction strengths

The Bose polaron has so far only been dynamically investigated at attractive interaction strengths. Here, the spectral function is composed of a peak marking the attractive polaron and a continuum of excited states. When crossing the resonance into repulsive interaction strengths, the spectral function becomes slightly more complicated, since a repulsive polaron peak emerges from the continuum. The two polaron branches have been observed spectroscopically [37, 38], but their influence on repulsive impurity dynamics in an ultracold Bose gas has until now remained elusive.

To understand how two polaron branches affect the dynamics, the scenario is now examined using a simple model. Naively, the spectral function at repulsive interaction strengths may be expressed as two well-defined narrow states at energies E_a and E_r for the attractive and repulsive polaron, respectively. By Fourier transforming this spectral function, the ensuing dynamics is expected to exhibit oscillations with a characteristic timescale $\sim h/|E_\mathrm{r} - E_\mathrm{a}|$, where h is Planck's constant, due to a quantum beat between the two states [97]. This is illustrated in Fig. 4.1 and close to unitarity, where the energies are $\sim E_n$, the beating correspondingly occurs on the timescale $\sim t_n$. This behavior is distinctively different than the power-law evolution of the initial impurity dynamics, which also occurs on the timescale $\sim t_n$ at large attractive interaction strength, as discussed in Chap. 3. The presence of two polaron branches at repulsive interaction strengths is therefore expected to be reflected by oscillations in the observed dynamics.

For the impurity in a Fermi gas such a quantum beat was observed in Ref. [36] at large interaction strengths. Furthermore, the Fourier transform of the Ramsey signal revealed a double-hump structure indicating two broadened polaron states in the spectral function. This result highlights the importance of including both branches when modelling the impurity dynamics.

In the following publication [94], a diagrammatic model [47, 56] is employed to analyze the data. The theoretical description includes both polaron branches in the spectral function and is thus capable of describing dynamics at both attractive and repulsive interaction strengths. First, the model is benchmarked to a measurement of impurity dynamics at large attractive interaction strengths. Subsequently, it is compared to a measurement at large repulsive interaction strengths to investigate how influential the emergence of the repulsive polaron branch is.

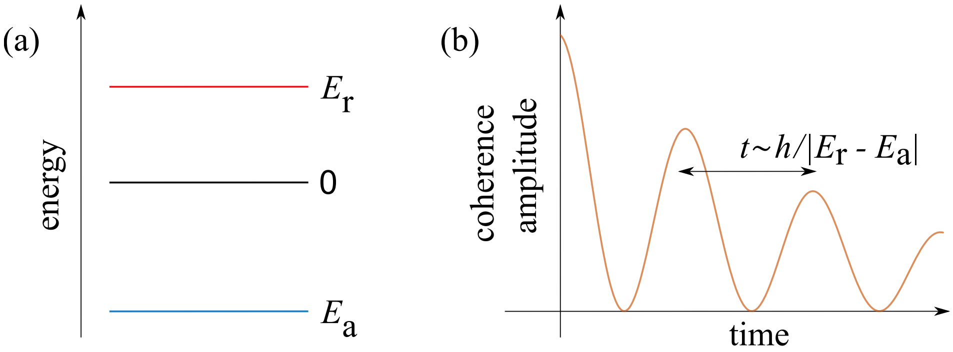

Figure 4.1: Illustration of a quantum beat. (a) Two polaron states are involved with energies E_a and E_r for the attractive and repulsive polaron branch, respectively. (b) The resulting dynamics exhibits a quantum beat between the two states. For the coherence amplitude this manifests as oscillations with a characteristic timescale $t \sim h/|E_\mathrm{r} - E_\mathrm{a}|$ [97].

4.3 Instantaneous energy of the impurity

The energy shift of the polaron is a signature property caused by interactions between the impurity and the medium. For the attractive polaron branch, the interactions lower the energy compared to that of a non-interacting impurity state, whereas interactions increase the energy for the repulsive branch, as discussed in Sec. 2.2. This energy shift was originally used to identify the Bose polaron using rf spectroscopy [37, 38]. However, it is also important for interferometric observations, since the polaron energy is expected to govern the phase evolution in the long-time limit.

The phase evolution φ_C of the impurity can be measured using the interferometric sequence discussed in Sec. 3.3. To investigate how the impurity equilibrates towards the polaron energy, the instantaneous energy is then defined as the slope of the phase evolution $E(t) = -\hbar d\varphi_C/dt$. A reliable method for extracting this slope is therefore required. In Ref. [84] this was achieved by fitting a linear function to the phase evolution in overlapping bins of 4 data points. Thus, the fits indicate the slope of the phase evolution in the center of each bin. However, to extract the instantaneous energy at *any* given time in the interval of the observed phase evolution, it is necessary to fit the data with a single function that captures the behavior of the data well.

Such a fitting function can be found by considering the initial impurity dynamics. As discussed in the previous chapter, this dynamical behavior may be described using power laws. Inspired by this, power-law functions can be used as a simple ansatz for fitting to the entire, observed phase evolution. In the following publication [94], a power-law fit At^{β} is therefore applied to the phase evolution of the impurity, with A and β as free parameters. Though this function does not necessarily reproduce the linear phase evolution that is expected for a well-defined polaron, it is a simple way of capturing the measured phase in a single, intuitive equation and investigating its slope. Thus, the instantaneous energy is extracted as $E(t) = -\hbar A\beta t^{\beta-1}$. Using the data sets reported in Ref. [84], the interferometrically measured energy of the impurity is then obtained. These energies can be compared with previous spectroscopic results [54] to investigate the link between the two experimental methods.

4.4 Polaron timescales

Generally, the life span of the polaron can be characterized by its initial formation and the eventual loss of the impurity. These two timescales need to be separated if the polaron as a well-defined quasiparticle is to be studied. Furthermore, the timescales involved in the measuring procedures require consideration. In this section, the ordering of these timescales for clear investigations of the Bose polaron is briefly discussed.

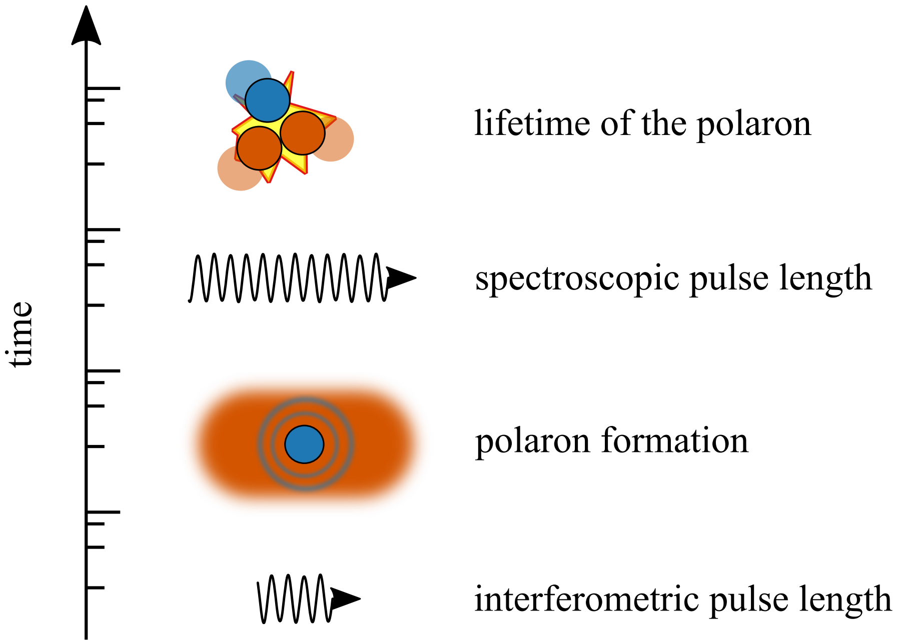

Figure 4.2: Illustration of the ideal ordering of timescales for investigation the polaron. The shortest timescale is that of an interferometric pulse length used to resolve impurity dynamics. This is followed by the timescale of polaron formation and subsequently the spectroscopic pulse length used to probe the equilibrium properties of the polaron in injection spectroscopy. Finally, the loss of the impurity through three-body collisions should occur on the longest timescale.

Interacting ultracold Bose gases inherently suffer from fast losses due to the possibility of three-body collisions. When investigating the polaron it is important to consider how influential such losses are. If the timescales of polaron formation and lifetime of the impurity are similar in size, it is not possible for a well-defined quasiparticle to be formed.

However, if formation time is shorter than the lifetime, the polaron may equilibrate before it is lost.

The ideal ordering of the dynamical and experimental timescales is illustrated in Fig. 4.2. To resolve the fast impurity evolution, interferometric pulses shorter than polaron formation are necessary, whereas spectroscopic pulses longer than formation but shorter than the lifetime are required in injection spectroscopy to probe the equilibrium properties of the polaron. Previous investigations [37, 84] have discussed how the formation and the lifetime influence their observations. However, a complete map of all timescales and their behavior for increasing interaction strengths have not yet been examined.

The paper presented in this chapter [94] contains a quantitative comparison of the timescales involved in polaron physics. It uses the transition time to the regime of many-body dynamics, investigated in Sec. 3.5, as a measure of initial polaron formation. Moreover, the lifetime is quantified using previously presented measurements [84]. The experimental timescales of spectroscopic and interferometric pulse lengths are chosen to be the values used in previous polaron studies in the same system [37, 84]. This comparison thus constitutes a transparent investigation of the relevant polaronic timescales and elucidate whether the experimental approaches are capable of probing the polaron before it is lost.

4.5 Life and death of the Bose polaron

The following paper [94] investigates repulsive impurity dynamics, the energy of the polaron and its timescales. The publication uses spectroscopic and interferometric measurements, which probe the polaron in the frequency- and time-domain, respectively. Thus, a systematic picture of the quasiparticle is developed. In the previous sections, the theoretical concepts and analytical tools have been outlined, and in this sections the main results are introduced and discussed.

4.5.1 Results

In the following paper [94] an analysis of the interferometrically measured impurity coherence is presented. For the coherence amplitude, this includes the first observation of impurity dynamics at strong repulsive interactions. These measurements display a coherence amplitude evolving faster than unitary dynamics and good agreement is obtained with a diagrammatic prediction. This reveals the emergence of the repulsive branch as the resonance is crossed into positive interaction strengths. A very small revival is visible in the data indicating a quantum beat between the two polaron branches. However, this feature is heavily suppressed by additional experimental decoherence sources.

For the analysis of the coherence phase, a fitting routine extracts a characteristic exponent for the dynamical behavior. This shows how universal effects increasingly influence the dynamics as the resonance is approached. Furthermore, the slope of the fit is used to extract the instantaneous energy. This is evaluated at the time of the last reliable phase data and compared with the diagrammatic predicted polaron energy and spectroscopic results. The high degree of agreement provides clear evidence that the two experimental approaches succeeded in creating and investigating different aspects of the same polaron.

Finally, the timescales of the polaron are investigated. This analysis reveals clear separation of initial polaron formation time and the lifetime of the impurity at all interaction strengths. The interferometric pulse length is always an order of magnitude below all other timescales, which indicates that it is well suited to investigate the polaron. The spectroscopic pulse length is in between polaron formation and its lifetime at weak interaction strengths. However, the analysis indicates that an adaptive pulse length could improve spectroscopic investigations at large and unitary interaction strengths.

4.5.2 Outlook

A related investigation using both rf spectroscopy and interferometric sequences was performed for the Fermi polaron in Ref. [36]. Here, a careful measurement of the spectral function was compared to the Fourier transform of the Ramsey signal at three interaction strengths. The clear agreement of the two experimental methods benchmarked the validity of the interferometric sequence. This analysis is similar to the one presented in the following paper [94]. However, here the focus is on the energetic location of the attractive polaron peak and not the full spectral function.

Furthermore, recent studies have investigated the effects of having a condensate with a finite temperature. Theoretically, the temperature has been predicted to influence the energy of the Bose polaron [55, 98] and a temperature dependence of the energy has also been measured experimentally [70]. However, no indications of such a dependence have been observed for the interferometric and spectroscopic studies discussed here. In particular, both results agree with a $T = 0$ diagrammatic calculation. For the interferometric observations, this can be explained by the thermal timescale $\tau \sim \hbar / k_\mathrm{B} T$ associated with decoherence. The temperature was $T \sim 50\,\mathrm{nK}$ in these experiments and correspondingly the thermal timescale was $\tau \sim 38 t_n$, which was beyond the accessible regime of impurity dynamics. In the spectroscopic investigations, the polaron energy was extracted from the center of the cloud. Here, the local condensate fraction is almost unity and thus the effective temperature is very close to zero [54]. Therefore, thermal effects are not expected to influence neither the interferometric nor the spectroscopic observations used in the following publication [94].

4.5.3 Publication

The investigation presented in Ref. [94] primarily reanalyzes data sets already reported in Refs. [37, 54, 84]. However, the measurement of impurity dynamics at repulsive interaction strengths constitute a new data set. These observations were acquired together with the data sets presented in Ref. [84], where I was a part of designing and performing the experiment. For this publication [94], I furthermore performed the data analysis, created all figures and wrote first drafts of the manuscript. The publication is currently in the stage of preparation before eventual submission.

Life and death of the Bose polaron

Magnus G. Skou[1], Thomas G. Skov[1], Nils B. Jørgensen[1], Kristian K. Nielsen[1],
Arturo Camacho-Guardian[1,2], Thomas Pohl[1], Georg M. Bruun[1,3], and Jan J. Arlt[1]
[1] *Center for Complex Quantum Systems, Department of Physics and Astronomy,*
Aarhus University, Ny Munkegade 120, DK-8000 Aarhus C, Denmark.
[2] *T.C.M. Group, Cavendish Laboratory, University of Cambridge,*
JJ Thomson Avenue, Cambridge, CB3 0HE, U.K. and
[3] *Shenzhen Institute for Quantum Science and Engineering and Department of Physics,*
Southern University of Science and Technology, Shenzhen 518055, China.
(Dated: March 31, 2021)

Probing a system spectroscopically or interferometrically complements each other in extracting its fundamental properties. While spectroscopy may provide precise measurements of equilibrated energies, interferometry can elucidate the dynamical evolution of the system. For an impurity immersed in a bosonic medium, both are equally important for understanding its inherent many-body nature. Here, we investigate and compare two recent experimental approaches in observing the Bose polaron [1, 2]. First, we show that an interferometric measurement of impurity dynamics at strong repulsive interactions indicates the emergence of the repulsive polaron branch. Secondly, an analysis of the interferometric measurements allows for an independent extraction of the impurity energy in good agreement with previous spectroscopic results. Finally, the dynamical timescales of formation and loss of the polaron are discussed, revealing a well-defined quasiparticle at all interaction strengths. This provides a complete picture of the many-body physics governing the polaron and thus validates the quasiparticle framework for further studies.

I. INTRODUCTION

The concept of quasiparticles is widely used in many areas of physics. It simplifies otherwise complex scenarios where interactions in a system can be described as emerging properties of quasiparticles instead. A canonical example is the polaron pioneered by Landau and Pekar [3]. Here, electrons are coupled to lattice vibrations giving rise to a quasiparticle they coined the polaron. However, these polarons have been difficult to observe in many materials due to high densities and fast evolution times or similar experimental challenges.

Quasiparticles have recently been experimentally realized using quantum gases. These serve as a powerful platform for simulating otherwise inaccessible regimes with high precision and have continuously advanced our understanding in the field [4]. The polaron in an ultracold quantum gas consists of an impurity and its excitations of the medium. This was initially studied in a Fermi gas using spectroscopic methods [5–10], which investigated the polaron energy and its quasiparticle residue. Subsequently, investigations of the dynamical evolution of the Fermi polaron were conducted [11, 12], which additionally provided evidence of a quantum beat between the two polaron branches. The challenging many-body nature of impurities in Bose gases inherently complicates experimental realizations. It is nonetheless essential for a comparison of the electron moving through a crystal lattice with bosonic excitations. Furthermore, it shows great potential for understanding some aspects of high-temperature superconductivity and colossal magnetoresistance [13]. The mobile Bose polaron was first observed spectroscopically [1, 14–16] where the attractive and repulsive polaron branches were identified. This provided a benchmark for our theoretical understanding of the polaron. Recently, a paper conducted the first investigation of the dynamical properties of the Bose polaron [2]. Here, different regimes of dynamical behavior were observed from initial two-body universal dynamics through two-body weak coupling and finally dynamics governed by many-body correlations.

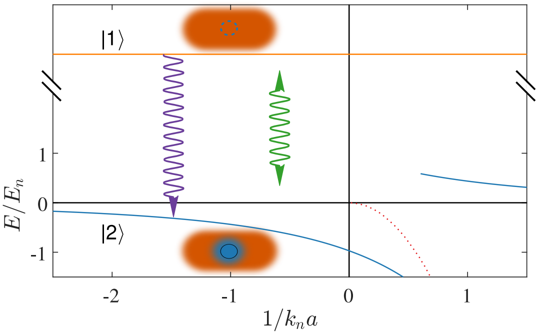

FIG. 1. Illustration of the polaron energy spectrum and experimental methods. A medium state $|1\rangle$ is shown as a solid orange line and an impurity state $|2\rangle$ as solid blue lines. The impurity state is shifted in energy due to interactions with the medium and features an attractive and a repulsive polaron branch. Spectroscopic methods use a single radio-frequency (rf) pulse, indicated with a single-headed purple arrow, to investigate the spectral response of the impurity by transferring a few atoms into the impurity state whereby polarons are formed. Interferometric sequences use two rf pulses, indicated with a double-headed green arrow, to measure the dynamical evolution of a superposition of the medium state and the impurity state. The dotted red line shows the molecular state at the repulsive side of the Feshbach resonance.

In this paper, we present a comparison of interferometric and spectroscopic observations of the Bose polaron. Both methods use the same two quantum states as medium and impurity, and their respective energy dependence are illustrated in Fig. 1. The spectroscopic approach investigates the spectral response of the polaron through a three-body loss signal, and the interferometric method employs a Ramsey-like sequence to extract the dynamics of an impurity state as it equilibrates. A measurement of impurity dynamics at strong repulsive interactions is presented, which infers the existence of both an attractive and a repulsive polaron state. Furthermore, a detailed analysis of the phase evolution allows us to extract the energy from weak attractive interactions to unitarity. This is compared with previous spectroscopic results obtaining good agreement. Finally, the dynamical timescales of the polaron are investigated. These timescales include the polaron formation time, the lifetime of the impurity and experimental pulse lengths, and comparing these reveals in which regime the interferometric and spectroscopic approaches are most ideally suited to study the polaron.

The paper is structured as follows. First, experimental details of the spectroscopic and interferometric observations and loss measurement of the polaron are discussed in Sec. II. Then, an analysis of the coherence amplitude based on the interferometric measurements is presented in Sec. III. This includes an observation of the impurity at large repulsive interaction strengths. Sec. IV provides an analysis of the phase evolution using a new fitting procedure. This allows the interferometrically measured impurity energy to be extracted from weak to strong attractive interactions and compared with previous spectroscopic results. Finally, the experimental timescales are discussed in Sec. V with a focus on the formation of the Bose polaron and the eventual loss of it.

II. EXPERIMENTAL DETAILS

The energy spectrum of the Bose polaron has previously been investigated spectroscopically [1], and interferometric observations of the polaron have measured its dynamical evolution [2]. Both approaches are equally important in characterizing the properties of the polaron and it is therefore important to discuss the similarities and differences of the two experimental procedures. In this section, we review the experimental details of these two approaches. Moreover, we discuss recent dynamical loss measurements of the polaron.

Both the spectroscopic and interferometric experiments were performed in the same system using ^{39}K BECs. These were produced in an optical dipole trap [17] in the $|F=1, m_F=-1\rangle \equiv |1\rangle$ hyperfine state. A second hyperfine state $|F=1, m_F=0\rangle \equiv |2\rangle$ served as the impurity state. The interaction between the two states is characterized by the dimensionless parameter $1/k_n a$, where the wave number $k_n = (6\pi^2 n_\mathrm{B})^{1/3}$ is set by the average condensate density n_B and a is the scattering length between the two states. Importantly, a can be controlled by magnetic fields through a Feshbach resonance located at 113.8 G [18, 19]. The scattering length between medium atoms is constant $a_\mathrm{B} \approx 9a_0$ for the applied magnetic fields, where a_0 is the Bohr radius. Furthermore, the impurity-impurity scattering length is $\approx -15a_0$ and is not relevant due to low impurity concentrations.

In a radio-frequency (rf) spectroscopic experiment, two states are coupled with a rf field. For the system at hand, these are the impurity and medium state with an approximate atomic transition frequency of 76 MHz. Interactions between the two states lead to an energy shift of the resonance frequency, which is measured by varying the frequency of the rf pulse. The experiment is then repeated for many values of $1/k_n a$ thus mapping out the complete spectral response of the impurity. Spectroscopic measurements generally require a long probe pulse of low power to resolve the spectrum. The spectrum scales with the relevant system energy $E_n = \hbar^2(6\pi^2 n_\mathrm{B})^{2/3}/2m$ and a square pulse of 100 µs duration was used in Ref. [1], achieving an experimental resolution of $0.15E_n$. If the frequency of the rf pulse matches the transition frequency from the medium state to the impurity state, atoms are transferred into this state and polarons are formed in the medium. The transition frequency is generally broadened due to the continuum of excited states and the inhomogeneous density of the medium. Following the formation of polarons, they are quickly lost through three-body recombination with two medium atoms. It is therefore not possible to obtain a direct measurement of the polarons. However, the loss mechanism can be utilized as the experimental signal. By varying the frequency of the rf pulse while measuring the number of medium atoms using absorption imaging, the spectral response of the polaron is thus extracted. This procedure is an example of injection spectroscopy and probes both the ground state of the polaron and the continuum of excited states. For the specific measurements in Ref. [1], the pulse power was chosen to transfer 10% into the impurity state.

To investigate the formation of the Bose polaron, a different technique is required to resolve the dynamical evolution. This can be achieved with an interferometric sequence, which produces a coherent superposition with a first rf pulse and probes the system with a second rf pulse following a variable evolution time. This scheme corresponds to a Ramsey sequence [11, 12, 20, 21]. However, instead of equal superpositions, a small initial rotation is employed. This allows the $|1\rangle$ state and the $|2\rangle$ state to be assigned as medium and impurity state, respectively. In the experimental system outlined above, this procedure can be realised with very short pulses of 0.5 µs duration resonant with the atomic transition. These pulses are well below the characteristic timescale $t_n = \hbar/E_n \sim 4.8$ µs and thus ideally suited to resolve the dynamics. Specifically, the pulses correspond to $\pi/7$ pulses and the first pulse creates a superposition of the $|1\rangle$ state and the $|2\rangle$ state with a $\sim 5\%$ population of the the latter. After the initial pulse, the system evolves toward the polaron state. Interactions cause the system to decohere characterized by $|C(t)|$ and to evolve with a certain phase $\varphi_\mathrm{C}(t)$. A second pulse is then used to probe the system. This pulse is applied with a variable phase between $[0, 2\pi]$. Depending on the phase of the second pulse, additional atoms are transferred to the impurity state or impurity atoms are transferred back to the medium state. This corresponds to a sinusoidal Ramsey signal. Following the interferometric sequence, absorption imaging is used to extract the spin population and by fitting to the measured Ramsey signal, the amplitude $|C(t)|$ and phase $\varphi_\mathrm{C}(t)$ are obtained. This provides the coherence $C(t) = |C(t)|e^{i\varphi_\mathrm{C}(t)}$ between the initial state and the time evolved impurity state.

Finally, the lifetime of the impurity state sets an important limit for both experiments. We refer to this as the death of the polaron. The lifetime of the impurity should ideally be longer than the dynamical evolution towards the polaron state. Such a separation of timescales leads to a well-defined polaron and enables its investigation. The lifetime of the impurity state is therefore investigated experimentally by using a third state as follows [2]. At a chosen interaction strength, a BEC is prepared in the $|1\rangle$ state. An initial rf pulse of $0.8\,\mu$s duration then creates a superposition of the $|1\rangle$ and $|2\rangle$ states corresponding to a 10% population in the latter. In a following evolution time t, some of these impurities are lost predominantly due to three-body collisions, where two medium atoms are lost for each impurity atom. Subsequently, a second rf pulse of $\sim 9\,\mu$s duration transfers the remaining impurity atoms to the hyperfine state $|F=1, m_F=+1\rangle \equiv |3\rangle$. The impurities in the $|3\rangle$ state can perform spin-flip collisions with the medium atoms in the $|1\rangle$ state, where both atoms obtain sufficient kinetic energy to leave the trap. This fast two-body mechanism removes a single medium atom for each impurity practically instantaneously. Since the two processes lead to a difference in the number of lost medium atoms, this sequence allows us to obtain the loss rate of impurities in the $|2\rangle$ state by measuring the number of medium atoms in the $|1\rangle$ state as a function of the evolution time t at different interaction strengths.

III. NEAR-UNITARY IMPURITY DYNAMICS

In this section, we analyze the interferometrically measured coherence amplitude $|C(t)|$ for two data sets at near-unitary interaction strengths. In Refs. [2, 22], the dynamics of the coherence was shown to exhibit three regimes depending on the interaction strength and the evolution time. Initially, two-body universal dynamics governs the evolution which is followed by a two-body weak coupling regime with an interaction dependent timescale. Finally, at long evolution times the impurity dynamics eventually transitions into a regime of many-body correlations.

At large interaction strengths, the scattering between the impurity state and the medium state is limited by the condensate density. Thus, the initial two-body universal dynamics transitions directly into a many-body regime in agreement with a diagrammatic prediction [2]. We therefore compare the observed amplitude with the universal description and this many-body prediction.

A. Strong attractive interactions

We begin by analyzing the interferometric results at large attractive interaction strengths $1/k_n a = -0.26$. Generally, the dynamics can be described as the Fourier transform of the spectral function [2, 22]. Thus, the initial behavior of the coherence can be obtained by Fourier transforming the tail of the spectral function for high frequencies [23]. For the coherence amplitude this yields the following universal behavior

$$|C(t)| = 1 - \frac{16}{9\pi^{3/2}} \left(\frac{t}{t_n}\right)^{3/2} \tag{1}$$

for $t \ll ma^2/\hbar$. This expression is a direct consequence of the high-frequency interaction independent scattering the impurity state undergoes for short times [24]. This was previously shown to capture the initial dynamics exceedingly well directly at unitarity [2].

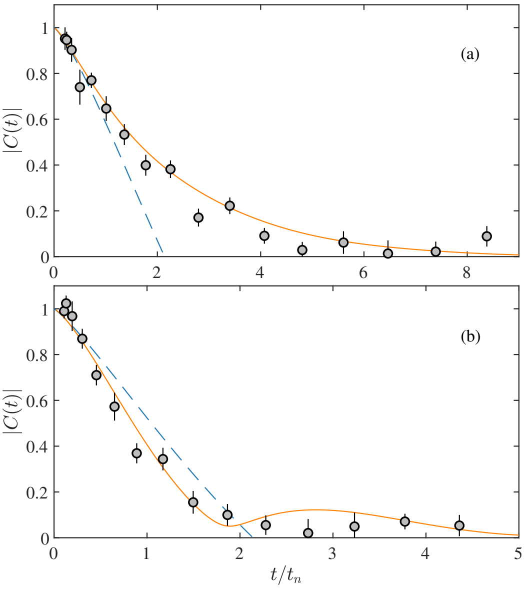

FIG. 2. Impurity dynamics at strong interactions. The coherence amplitude (a) at $1/k_n a = -0.26$ and (b) at $1/k_n a = +0.3$ is shown as grey circles. A two-body density-limited universal prediction is shown as a dashed blue line and a many-body prediction as a solid orange line.

For large interaction strengths $|1/k_n a| \lesssim (2/3\pi)^{1/3}$ [2], the universal behavior is followed by many-body dynamics. There exists no exact solution for the dynamical evolution at these strong interactions. Instead, theoretical approaches to obtain approximate solutions have included diagrammatic [25–27], variational [24, 28] and quantum Monte Carlo calculations [29, 30]. Here, we employ the former which uses a ladder approximation valid for all interaction strengths to derive a spectral function containing a polaron ground state and a continuum of excited states. It models the impurity dynamics by Fourier transforming this spectral function thus obtaining the impurity coherence function [2].

Figure 2(a) shows the coherence amplitude for $1/k_n a = -0.26$ together with the two-body universal and the diagrammatic description. The observed amplitude reveals a fast early decrease followed by a slower evolution for longer times. The initial dynamics is in clear agreement with both theoretical descriptions until the dynamics enters the many-body regime at $\sim 1.4t_n$ [2]. Here, the slower evolution of the observations is captured well by the diagrammatic description. This outstanding agreement of the experimental observations and the ladder approximation solidify our understanding of the many-body correlations.

B. Strong repulsive interactions

We now analyze the first interferometric measurement of the Bose polaron at large repulsive interaction strengths $1/k_na = +0.3$. Generally, at strong repulsive interactions two polaron branches are present as shown in Fig. 1. The attractive branch crosses the resonance approaching the molecular state and at higher energies a repulsive state emerges but is damped due to the possibility of decay into lower lying states. We therefore expect both branches to affect the ensuing impurity dynamics.

Directly at unitarity the scattering length diverges and the dynamics is set by the universal timescale t_n. One would intuitively presume this to be the fastest evolving decoherence for any interactions, since the only limiting factor is the density. However, when crossing the resonance into strongly repulsive interactions, we observe an even faster evolving system. This is shown in Fig. 2(b) for the coherence amplitude at $1/k_na = +0.3$ in comparison with the universal prediction. Here, the observed amplitude quickly decays and vanishes for the first time at $3t_n$. The amplitude clearly evolves faster than the two-body universal prediction which captured the initial dynamics at unitarity [2]. This discrepancy is attributed to the presence of two polaron branches at these repulsive interaction strengths, which is not included in the universal description.

A better model of the repulsive impurity dynamics is given by the ladder approximation since it contains both branches and is valid for attractive as well as repulsive interaction strengths. Importantly, it predicts a coherence amplitude evolving faster than universal dynamics. Moreover, it captures the initial behavior of the observations well, thus showing the necessity of including both polaron branches.

A special feature of impurity dynamics at repulsive interaction strengths is a quantum beat between the two polaron branches [12]. In the experimental realization such a revival is suppressed due to three-body losses. However, the data does display a minima followed by a small revival, which may indicate such a quantum beat. For the diagrammatic description the revival is more clearly seen.

These observations constitute the first measurement of impurity dynamics at repulsive interaction strengths in a BEC and indicate a complex situation with multiple states responsible for the effective dynamics. However, the high degree of consensus for both strongly attractive and repulsive interaction strengths consolidates the diagrammatic description as a good model for the system.

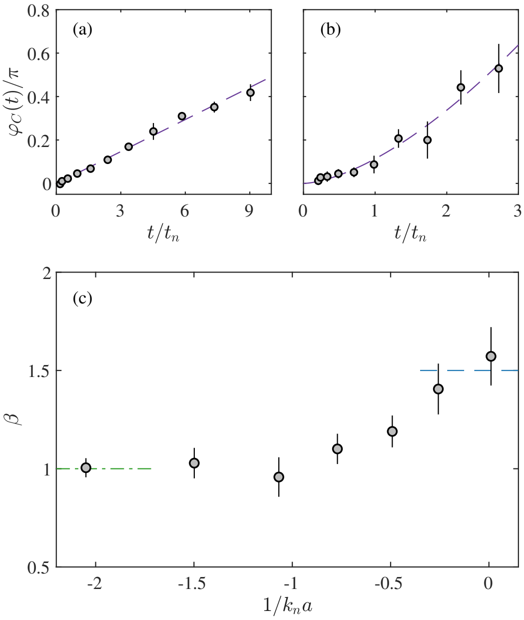

FIG. 3. Phase evolution and fitted exponent. The observed phase evolution and applied fit is shown for (a) $1/k_na = -2$ and (b) $1/k_na = 0.01$. (c) Characteristic exponent obtained by fitting a power law to the phase evolution. The dash-dotted green line indicates the mean-field exponent and the dashed blue line shows the two-body universal exponent.

IV. IMPURITY ENERGY

The phase evolution is generally a rich source for obtaining information of a given system. This has previously been used to measure the relative phase of a two-component BEC [31] and to obtain the two- and three-body contact in a unitary Bose gas [32]. In this section, we extract the energy of the impurity from the measured phase evolution. This permits a comparison between the interferometrically measured polaron energy and previous spectroscopic results.

A. Interferometric phase analysis

Similarly to the coherence amplitude, the phase evolution is also governed by different dynamical regimes [2, 22]. These include the two-body universal, the two-body weak coupling and the many-body regime as discussed in Sec. III. In the following, the transition between the universal and the weak coupling regime is investigated by applying a power-law fit to the observed phase evolution. This provides the exponent, which signals the functional behavior of the two regimes.

Generally, the initial two-body behavior of the phase evolution can be obtained by Fourier transforming the high-frequency tail of the spectral function similarly to the coherence amplitude [23]. Its behavior depends on both the medium density n_B and the scattering length a between impurity state and medium state. The corresponding phase evolution can be reduced to the following limits [2]

$$\varphi_\mathrm{C}(t) = \begin{cases} \frac{16}{9\pi^{3/2}} \left(\frac{t}{t_n}\right)^{3/2} & t \ll t_a \\ -E_\mathrm{mf} t/\hbar - \left(\frac{t}{t_\mathrm{w}}\right)^{1/2} & t \gg t_a. \end{cases} \tag{2}$$

Here $t_a = ma^2/\hbar$ is the transition time between initial universal and subsequent weak coupling dynamics, $E_\mathrm{mf} = 4\pi\hbar^2 n_\mathrm{B} a/m$ is the mean-field energy and $t_\mathrm{w} = m/32\pi\hbar n_\mathrm{B}^2 a^4$ is the interaction dependent timescale for weak coupling dynamics.

At strong and unitary interactions, t_a approaches infinity and the initial phase evolution is solely determined by the two-body universal regime, where the exponent is $\beta = 3/2$. This was the case treated in Sec. III. For weak interaction strengths, t_a is typically smaller than the experimental resolution and the dynamics quickly transitions into the two-body weak coupling regime. Here, the phase evolution is characterized by both a linear and a square-root time dependent term. However, the linear mean-field term with $\beta = 1$ dominates and governs the evolution when $t \gg 2ma^2/\pi\hbar \sim 0.64 t_a$ which is always fulfilled in this regime. At longer evolution times, the dynamics enters the regime of many-body correlations where no single power-law behavior is expected.

Inspired by this, we fit a power law to the observed phase evolution $\varphi_\mathrm{C}(t) = At^\beta$ to investigate how the exponent behaves for increasing interaction strength. Selected phase evolutions and applied fits are shown in Fig. 3(a-b). For a weak interaction strength, the phase evolves linearly, however, for a unitary interaction strength, the phase evolution is both faster and slightly non-linear. The power law fits the observations well indicating that the behavior of the data is clearly captured. A similar analysis has previously been employed for the coherence amplitude [22], where a power law was fitted to the data to characterize the same transition. However, since the phase is not directly affected by the same experimental decoherence processes, the analysis here is greatly simplified.

The fitted exponent is shown in Fig. 3(c) together with the mean-field and universal values. At weak interaction strengths, the fitted exponent clearly signals dynamics governed by mean-field effects and agrees with $\beta = 1$. For larger interaction strengths, it slowly increases before agreeing with the universal prediction $\beta = 3/2$ at unitarity. This indicates how beyond mean-field effects become increasingly important with increasing interaction strength as the observed phase evolution clearly separates from linearity for $1/k_n a \gtrsim -0.5$. Since the phase evolution at all interaction strengths is subject to more than one regime of impurity dynamics, the exponent is the result of the fit trying to accommodate different time dependencies in a single value. However, the fitted exponent does indicate which regime is dominant within the interval of reliable experimental data.

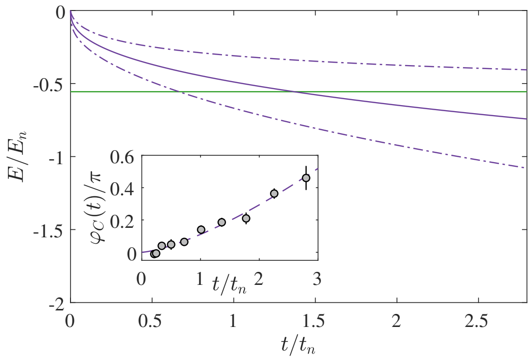

FIG. 4. Instantaneous energy at strong interactions. The instantaneous energy, obtained from fitting a power law to the phase evolution at $1/k_n a = -0.26$, is shown as a solid purple line and the dash-dotted purple lines reflect the propagated error from the 1σ confidence interval of the fitted values. A diagrammatic prediction of the polaron energy is shown as a solid green line. (inset) The phase evolution and the power-law fit at $1/k_n a = -0.26$ are shown.

B. Instantaneous energy

The fitting procedure discussed above allow us to investigate the instantaneous energy of the impurity from weak to large attractive interaction strengths. We furthermore use this for a direct comparison with previously reported spectroscopic results, which provides a clear benchmark of the two experimental approaches.

The phase evolution of the polaron state is for long times governed by its energy. For weak interaction strengths, the impurity exhibits a mean-field shift in energy and correspondingly the phase evolution is linear as shown in Fig. 3(a). However, this changes with increasing interaction strength as shown in Fig. 3(b). We therefore define the instantaneous energy as the slope of the phase evolution at any given time $E(t) = -\hbar d\varphi_C/dt$. With the fitted power-laws At^β this corresponds to $E(t) = -\hbar A\beta t^{\beta-1}$.

An example is shown in Fig. 4. Here the instantaneous energy at $1/k_n a = -0.26$ displays a fast initial decrease followed by a slower evolution as the impurity reaches its steady state. The inset of Fig. 4 consolidates the validity of the applied power-law fit. A theoretical description of the Bose polaron energy [15] is also included. The instantaneous energy reaches this value at $\sim 1.5 t_n$ showing that the impurity quickly evolves to a state with similar energy as the Bose polaron.

To compare the interferometrically measured energies with the spectroscopic result, we now extract the instantaneous energy evaluated at the time of the last reliable phase data. This represents the energy of the impurity state at the longest observable evolution time and its behavior for increasing interaction strength can thereby be investigated. Figure 5 shows the extracted energies together with previous experimental observations, a diagrammatic prediction and the mean-field energy [15]. The interferometrically measured energies de-

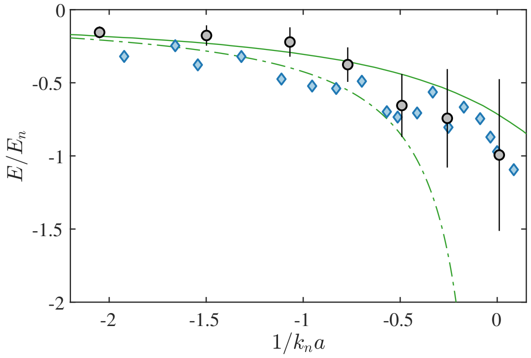

FIG. 5. Impurity energy at attractive interaction strengths. The impurity energies at the longest observable phase evolution are shown as grey circles together with the spectroscopically measured polaron energies as light blue diamonds and a diagrammatic prediction as a solid green line [15]. The mean-field energy is shown as a dash-dotted green line

creases with increasing interaction strength. For weak interaction strengths, they are in clear agreement with the diagrammatic predicted energy, whereas they only qualitatively agree with the spectroscopic result. However for large interaction strengths, excellent agreement is obtained between the interferometric and spectroscopic observed energies. This provides clear evidence that the interferometric and spectroscopic method inherently create and probe similar systems, though they differ in their experimental approach with pulse lengths separated by orders of magnitude.

V. IMPURITY TIMESCALES

To investigate the Bose polaron, it is crucial that experimental timescales and dynamical timescales of the polaron are clearly separated, which is investigated in this section. The inherent timescales of the polaron are associated with its formation and with its lifetime, which both depend on the interaction strength. Experimentally, we need a probing pulse for spectroscopic investigations that is long enough to allow formation but shorter than the lifetime of the impurity. For interferometric observations, we need pulses shorter than both formation time and lifetime in order to resolve the polaron dynamics.

Previous spectroscopic measurements [1] have shown that losses occur on a separate timescale compared to polaron dynamics, since the width of the spectrum agreed with theoretical predictions without the inclusion of three-body losses. Recently, interferometric observations were conducted [2] which resolved the initial impurity dynamics. Based on these experiments it is possible to investigate and resolve the timescales of the polaron.

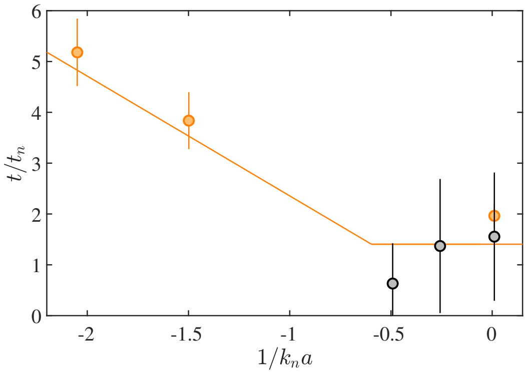

FIG. 6. Many-body transition and energetic polaron formation. The times at which the instantaneous energy equals the diagrammatic predicted polaron energy can be obtained for $1/k_n a \gtrsim -0.5$. These energetic polaron formation times are shown as grey circles. The many-body transition is shown as a solid orange line for the theoretical prediction and as orange circles for the experimental observations [2].

A. Polaron formation

The polaron generally consists of intricate many-body interactions between the impurity and the surrounding medium. When an impurity state is introduced in a medium, these interactions gradually lead to correlations forming over time. Theoretically, the formation timescale can be defined as the time when the impurity coherence amplitude is equilibrated at the quasiparticle residue [33, 34]. In experimental realizations, this equilibration is often masked by decoherence mechanisms such as dephasing from inhomogeneous density distributions, finite impurity lifetime and magnetic field fluctuations, prohibiting a direct observation of this equilibration timescale.

To quantify the time of initial polaron formation, an experimental accessible parameter is required, since the theoretically predicted formation time is not observable. However, the evolution of the impurity towards the polaron possesses a clear transition from initial two-body to many-body dynamics [2]. Since the polaron is embodied by these many-body correlations, we assign this transition to the early onset of polaron formation. Furthermore, it is possible to extract a timescale for the energetic polaron formation from the instantaneous energy. In the following, we therefore compare the many-body transition and the timescale of energetic formation to obtain a measure of initial polaron formation.

The timescale of energetic formation describes the evolution time required for the impurity to reach the Bose polaron energy. This time is obtained by comparing the instantaneous energy of Sec. IV with the diagrammatic predicted polaron energy. The time of energetic formation is then identified as the time when these two energies are equal. An example of this is shown in Fig. 4 where the energetic formation timescale is $1.4 t_n$.

Figure 6 shows the timescales of energetic formation and

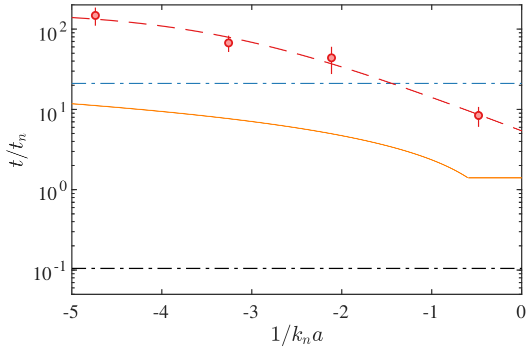

FIG. 7. Experimental and dynamical timescales of the Bose polaron. The dash-dotted black line shows the interferometric pulse length and the solid orange line shows the many-body transition time as a measure of initial polaron formation. The dash-dotted blue line shows the spectroscopy pulse length and the red circles are impurity lifetime measurements with a fit shown as a dashed red line [2].

the many-body transition. The three data points of energetic formation all indicate that the polaron energy is reached within $2t_n$. Furthermore, they agree well with the transition to the many-body regime at large interaction strengths. This method is only applicable when the exponent $\beta > 1$ which from Fig. 3(c) corresponds to $1/k_n a \gtrsim -0.5$. Nonetheless, this comparison consolidates that the many-body transition is a good indicator of initial polaron formation.

B. Experimental timescales

Based on the previous discussion of initial polaron formation, we may now compare the four relevant dynamical timescales. These include the interferometric pulse length, the initial formation time, the spectroscopic pulse length and, importantly, the lifetime of the polaron as discussed in Sec. II. Ideally, the timescales should be well separated and arranged in particular with the lifetime of the impurity longer than polaron formation to allow for the quasiparticle to be well-defined. Furthermore, the spectroscopic pulse length should be between the timescales of formation and lifetime, and the interferometric pulse length below all others in order to resolve the dynamics well.

Figure 7 shows these timescales as a function of the inverse interaction strength where all timescales have been scaled by $t_n = 4.8\,\mu\text{s}$. This reveals that initial polaron formation always precedes the loss of the impurity. Importantly, this permits investigations of the polaron. The free experimental parameters are then the length of the spectroscopic and interferometric pulses.

To investigate the polaron spectroscopically, ideally a pulse length longer than initial formation but shorter than the lifetime is required. However, a single pulse length may not necessarily fulfil this requirement at all interaction strengths and in Fig. 7 a compromise is therefore seen. For more precise measurements, an adaptive pulse length could be employed. Specifically, longer pulses are optimal for investigations at weak interaction strengths, whereas shorter pulses are well suited for measurements at strong interactions.

For all interaction strengths, the interferometric pulse is an order of magnitude below the other timescales. This supports that interferometric measurements clearly resolve the dynamics of the impurity even at the resonance, where the dynamics occur at the unitarity-limited timescale t_n.

VI. CONCLUSION

To summarize, we have here provided a detailed investigation of interferometric and spectroscopic measurements of the Bose polaron. The results include an observation of impurity dynamics at repulsive interaction strengths, an extraction of the instantaneous energy of the polaron in agreement with previous results, and a thorough analysis of the dynamical timescales of the polaron.

An interferometric measurement of the coherence amplitude at strong interactions revealed faster decoherence processes at large repulsive interaction strengths than at unitarity. Importantly, this indicates the presence of both an attractive and a repulsive polaron branch. Furthermore, the observations were in agreement with a many-body theoretical prediction which included both branches. This prompts the necessity for further investigations of impurity dynamics at repulsive interaction strengths.

Secondly, we obtained the instantaneous energy of the impurity from interferometric measurements. This impurity energy was compared with previous spectroscopic results from weak to strong attractive interactions obtaining clear agreement.

Finally, the timescales of the interferometric pulse length, the initial polaron formation time, the spectroscopic pulse length and the lifetime of the impurity were investigated. This showed a clear separation of formation time and lifetime at all interaction strengths. Furthermore, the comparison highlighted the capability of the interferometric approach to clearly resolve polaron dynamics and suggested new routes for spectroscopic measurements.

Based on this thorough discussion of the two experimental approaches employed so far, the stage is set for further investigation of the Bose polaron. While the size of the smallest Efimov trimer is much larger than the interparticle spacing, it has nonetheless been proposed to influence the energy of a resonantly interacting polaron [35]. Expanding investigations of the polaron energy at unitarity, by varying the density, may enable studying such a universal dependence on the Efimov three-body parameter. Another interesting aspect is the dynamics at higher impurity fractions, which may show mediated polaron interactions [26]. Such effective interactions are predicted to enable deeply bound states of bosonic bipolarons [36], which have so far been elusive to experimental observation. However, employing ejection spectroscopy [16] may enable measuring these exotic states.

VII. ACKNOWLEDGEMENTS

This work has been supported by the Danish National Research Foundation through the Center of Excellence CCQ (Grant agreement no.: DNRF156).

[1] N. B. Jørgensen, L. Wacker, K. T. Skalmstang, M. M. Parish, J. Levinsen, R. S. Christensen, G. M. Bruun, and J. J. Arlt, Phys. Rev. Lett. **117**, 055302 (2016).

[2] M. G. Skou, T. G. Skov, N. B. Jørgensen, K. K. Nielsen, A. Camacho-Guardian, T. Pohl, G. M. Bruun, and J. J. Arlt, Nat. Phys. (2021).

[3] L. D. Landau and S. I. Pekar, Zh. Eksp. Teor. Fiz. **18**, 419 (1948).

[4] I. Bloch, J. Dalibard, and S. Nascimbène, Nature Physics **8**, 267 (2012).

[5] A. Schirotzek, C.-H. Wu, A. Sommer, and M. W. Zwierlein, Phys. Rev. Lett. **102**, 230402 (2009).

[6] C. Kohstall, M. Zaccanti, M. Jag, A. Trenkwalder, P. Massignan, G. M. Bruun, F. Schreck, and R. Grimm, Nature **485**, 615 (2012).

[7] M. Koschorreck, D. Pertot, E. Vogt, B. Fröhlich, M. Feld, and M. Köhl, Nature (London) **485**, 619 (2012).

[8] F. Scazza, G. Valtolina, P. Massignan, A. Recati, A. Amico, A. Burchianti, C. Fort, M. Inguscio, M. Zaccanti, and G. Roati, Phys. Rev. Lett. **118**, 083602 (2017).

[9] Z. Yan, P. B. Patel, B. Mukherjee, R. J. Fletcher, J. Struck, and M. W. Zwierlein, Phys. Rev. Lett. **122**, 093401 (2019).

[10] N. Darkwah Oppong, L. Riegger, O. Bettermann, M. Höfer, J. Levinsen, M. M. Parish, I. Bloch, and S. Fölling, Phys. Rev. Lett. **122**, 193604 (2019).

[11] M. Cetina, M. Jag, R. S. Lous, J. T. M. Walraven, R. Grimm, R. S. Christensen, and G. M. Bruun, Phys. Rev. Lett. **115**, 135302 (2015).

[12] M. Cetina, M. Jag, R. S. Lous, I. Fritsche, J. T. Walraven, R. Grimm, J. Levinsen, M. M. Parish, R. Schmidt, M. Knap, *et al.*, Science **354**, 96 (2016).

[13] A. S. Alexandrov and J. T. Devreese, *Advances in Polaron Physics*, Vol. 159 (Springer-Verlag, Berlin, 2010).

[14] M.-G. Hu, M. J. Van de Graaff, D. Kedar, J. P. Corson, E. A. Cornell, and D. S. Jin, Phys. Rev. Lett. **117**, 055301 (2016).

[15] L. A. Peña Ardila, N. B. Jørgensen, T. Pohl, S. Giorgini, G. M. Bruun, and J. J. Arlt, Phys. Rev. A **99**, 063607 (2019).

[16] Z. Z. Yan, Y. Ni, C. Robens, and M. W. Zwierlein, Science **368**, 190 (2020).

[17] L. Wacker, N. B. Jørgensen, D. Birkmose, R. Horchani, W. Ertmer, C. Klempt, N. Winter, J. Sherson, and J. J. Arlt, Phys. Rev. A **92**, 053602 (2015).

[18] M. Lysebo and L. Veseth, Phys. Rev. A **81**, 032702 (2010).

[19] L. Tanzi, C. R. Cabrera, J. Sanz, P. Cheiney, M. Tomza, and L. Tarruell, Phys. Rev. A **98**, 062712 (2018).

[20] R. Scelle, T. Rentrop, A. Trautmann, T. Schuster, and M. K. Oberthaler, Phys. Rev. Lett. **111**, 070401 (2013).

[21] T. Rentrop, A. Trautmann, F. A. Olivares, F. Jendrzejewski, A. Komnik, and M. K. Oberthaler, Phys. Rev. X **6**, 041041 (2016).

[22] M. G. Skou, T. G. Skov, N. B. Jrgensen, and J. J. Arlt, Atoms **9**, 22 (2021).

[23] E. Braaten, D. Kang, and L. Platter, Phys. Rev. Lett. **104**, 223004 (2010).

[24] M. M. Parish and J. Levinsen, Phys. Rev. B **94**, 184303 (2016).

[25] S. P. Rath and R. Schmidt, Phys. Rev. A **88**, 053632 (2013).

[26] A. Camacho-Guardian and G. M. Bruun, Phys. Rev. X **8**, 031042 (2018).

[27] N.-E. Guenther, P. Massignan, M. Lewenstein, and G. M. Bruun, Phys. Rev. Lett. **120**, 050405 (2018).

[28] W. E. Liu, J. Levinsen, and M. M. Parish, Phys. Rev. Lett. **122**, 205301 (2019).

[29] L. A. P. Ardila and S. Giorgini, Phys. Rev. A **92**, 033612 (2015).

[30] L. A. P. Ardila and S. Giorgini, Phys. Rev. A **94**, 063640 (2016).

[31] R. P. Anderson, C. Ticknor, A. I. Sidorov, and B. V. Hall, Phys. Rev. A **80**, 023603 (2009).

[32] R. J. Fletcher, R. Lopes, J. Man, N. Navon, R. P. Smith, M. W. Zwierlein, and Z. Hadzibabic, Science **355**, 377 (2017).

[33] Y. E. Shchadilova, R. Schmidt, F. Grusdt, and E. Demler, Phys. Rev. Lett. **117**, 113002 (2016).

[34] K. K. Nielsen, L. A. P. Ardila, G. M. Bruun, and T. Pohl, New Journal of Physics **21**, 043014 (2019).

[35] S. M. Yoshida, S. Endo, J. Levinsen, and M. M. Parish, Phys. Rev. X **8**, 011024 (2018).

[36] A. Camacho-Guardian, L. A. Peña Ardila, T. Pohl, and G. M. Bruun, Phys. Rev. Lett. **121**, 013401 (2018).

CHAPTER 5

OBSERVATION OF BIPOLARONS

A polaron is composed of an impurity and its interactions with a surrounding medium. Interestingly, polarons are also capable of interacting with each other through the density of the medium. A recent theoretical study predicted that such induced interactions between two polarons in a Bose-Einstein condensate can lead to a bound state [57]. This state is known as a Bose bipolaron, and in this chapter the first experimental observations of such bipolarons are presented.

The chapter is structured as follows. First, the effective interactions between polarons and the formation of bipolarons are introduced in Sec. 5.1. Subsequently, in Sec. 5.2 the experimental procedure and the challenges in observing bipolarons are discussed. In Sec. 5.3, a line shape function used to model the spectral response of the system is introduced, and in Sec. 5.4 the first experimental evidence of dynamically forming bipolarons is presented and the effects of a finite impurity fraction are discussed. The observed bipolaron energy at strong attractive interactions is then shown in Sec. 5.5 and the experimental limitations are considered. This is followed by a presentation of the measured polaronic quasiparticle residue in Sec. 5.6 and a discussion of a similar measurement for the bipolaron. Finally, the results of this chapter are summarized in Sec. 5.7.

5.1 Effective interactions between polarons

Bipolarons are important examples of the scenario where induced interactions lead to the formation of bound states [57, 99]. Investigations of such intricate interactions between complex many-body quasiparticles are inherently challenging but exceedingly interesting, since they are significant for the comprehension of many fascinating materials. In particular, bipolarons have been used for a simplified model of quantum dots [100] and have also been proposed as a mechanism for organic magnetoresistance [101].

The induced interactions between polarons are not caused by direct impurity-impurity scattering. Instead, they are mediated by the exchange of Bogoliubov sound modes in the condensate. This can be modelled using the Landau effective interaction, which has successfully been employed to impurities interacting with a Bose-Einstein condensate. Importantly, the effective interaction is more pronounced for Bose polarons than Fermi polarons, since a BEC is more compressible than a Fermi gas. Besides the formation of bipolarons, the interaction has been predicted to cause a shift in the polaron energy [56].

The formation of a bipolaron is illustrated in Fig. 5.1 for two polarons in a homogeneous medium. For low interaction strengths between the impurity and the medium, the polarons have little interactions with each other. Larger impurity-medium interaction strengths increase the effective interaction between the polarons through the density fluctuations of the medium. At sufficiently large interaction strengths, the two polarons

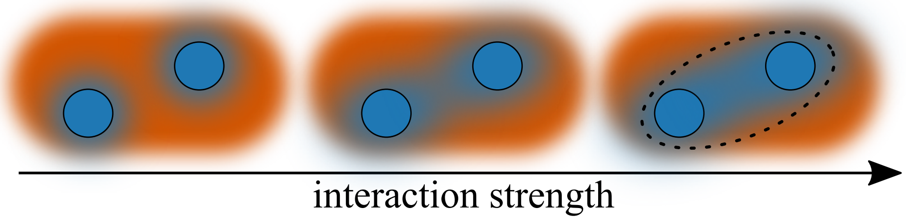

Figure 5.1: Illustration of induced interactions between two polarons at three impurity-medium interaction strengths. For increasing interaction strength, the interactions between the polarons mediated by the medium density become stronger as well. A bound state constituting the bipolaron is formed beyond a critical interaction strength.

form a bound state constituting the bipolaron.

This bound state will be the focus of the following sections. The energy of the bipolaron was calculated in Ref. [57] as a function of interaction strength using a diagrammatic approach. This revealed a significant shift away from the polaron energy for strong attractive interactions. The predicted bipolaron energy was moreover compared to quantum Monte Carlo simulations obtaining excellent agreement, thus benchmarking the diagrammatic description.

5.2 Experimental procedure

Injection and ejection spectroscopy are two effective ways of studying impurities, and they have both been employed to observe the Bose polaron. The first measurements of the Bose polaron indeed used rf injection spectroscopy to investigate the energy spectrum by injecting impurities into an interacting state using a pulse with a narrow frequency width, thus resolving the spectral response of the impurity [37, 38]. Recently, rf ejection spectroscopy was employed for a more precise measurement of the Bose polaron [70], where the spectrum was obtained by ejecting the impurities from the polaronic interacting state into a non-interacting state. The link between the two approaches has also been studied theoretically [102] and here, both methods are used to investigate the spectral response of polarons and bipolarons. This section therefore outlines experimental procedures for using injection and ejection spectroscopy.

Initially, a ^{39}K BEC in the hyperfine state $|F = 1, m_F = -1\rangle \equiv |1\rangle$ is held in an ODT. The experimental production of such a BEC is discussed in Sec. 3.2. For the following investigations, the mean geometric trap frequency was $2\pi \times 70\,\mathrm{Hz}$ and the temperature was $70\,\mathrm{nK}$. The resulting average density of the condensate was $n_\mathrm{B} = 0.6 \times 10^{14}\mathrm{cm}^{-3}$, which sets the interaction independent energy scale $E_n = \hbar^2 k_n^2/2m$ through the characteristic wavenumber $k_n = (6\pi^2 n_\mathrm{B})^{1/3}$. Furthermore, the relevant dynamical timescale was $t_n = \hbar/E_n \sim 5.5\,\mu\mathrm{s}$ for these experiments.

To initiate the experiment, the magnetic field is ramped to a target value near an interstate Feshbach resonance between the $|1\rangle$ state and the $|F = 1, m_F = 0\rangle \equiv |2\rangle$ state, where the latter is used as an interacting impurity state. The interaction strength between the two states is characterized by the dimensionless parameter $1/k_n a$. Here a is the interstate scattering length, which is tuned via a Feshbach resonance by the applied magnetic field. The employed resonance is located at $113.8\,\mathrm{G}$ and has previously been described in great detail both theoretically [41] and experimentally [42]. Importantly, the scattering length between medium atoms is approximately constant across the applied magnetic fields at $a_\mathrm{B} \approx 9a_0$, where a_0 is the Bohr radius.

Generally, interactions between the medium atoms and the impurity atoms result in an energy shift of the impurity state $|2\rangle$. In injection spectroscopy, this detuning is obtained by measuring the resonance frequency between the $|1\rangle$ state and the $|2\rangle$ state. This is illustrated in Fig. 5.2(a), where a long rf pulse is used to transfer a small fraction of the atoms to

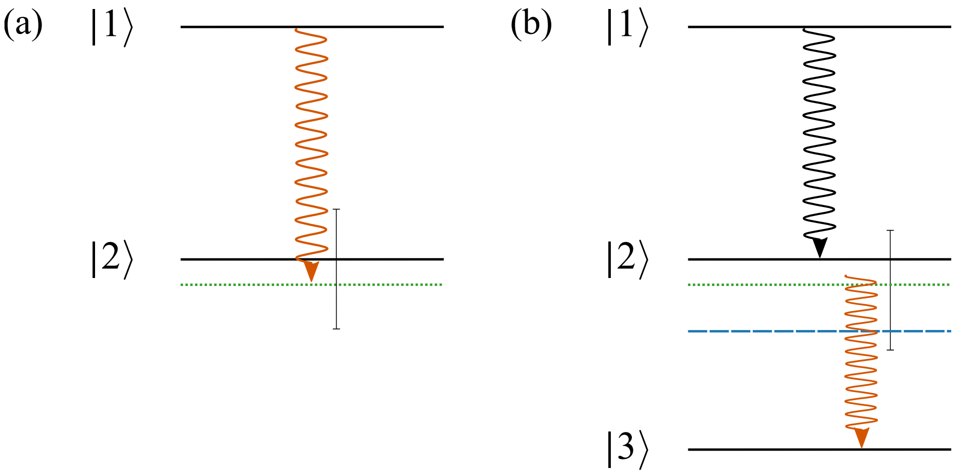

Figure 5.2: Overview of the employed injection and ejection spectroscopy methods. (a) In injection spectroscopy, the impurity is investigated by measuring the spectral response of transferring a few atoms from the medium state $|1\rangle$ to the interacting impurity state $|2\rangle$. (b) In ejection spectroscopy, an initial short pulse resonant with the atomic transition transfers a small fraction of the atoms into the interacting state $|2\rangle$. After a variable evolution time, the spectral response of transferring these impurities to a weakly-interacting state $|3\rangle$ is measured. The polaron and bipolaron energies are marked with a dotted green and dashed blue line, respectively, and the scan range is indicated by the thin vertical line.

the $|2\rangle$ state. In Ref. [37], the employed pulse length was $100\,\mu s$, which resolved the spectrum well. In the following, a pulse length of $20\,\mu s \sim 4t_n$ is used and the power of the pulse is chosen to produce a superposition corresponding to a $\sim 16\%$ population in the $|2\rangle$ state. During the extent of the pulse, the system quickly decoheres and polarons are formed. The minority population in the $|2\rangle$ state thus acts as an impurity interacting with the medium atoms in the $|1\rangle$ state. These impurities are eventually lost through three-body collisions, where each impurity removes two medium atoms. Consequently, a low final number of atoms in the medium state reflects a large number of impurities transferred into the $|2\rangle$ state. Experimentally, a shift in the transition frequency revealing the polaron energy is thus indicated by an increased loss of medium atoms.

The employed ejection spectroscopy uses a two-pulse scheme to measure the impurity spectral response as illustrated in Fig. 5.2(b). The first rf pulse creates a superposition of the $|1\rangle$ state and the $|2\rangle$ state corresponding to a $\sim 20\%$ population in the latter. The pulse length is short $1.2\,\mu\mathrm{s} \sim 0.2t_n$ and the pulse is therefore spectrally broad. In a following variable evolution time t, both polarons and bipolarons are formed. Then, a second rf pulse measures the spectral response of the impurities by ejecting them from the $|2\rangle$ state into the $|F=1, m_F=+1\rangle \equiv |3\rangle$ state. This rf pulse needs to be short compared to the dynamical formation of bipolarons but long enough to resolve the spectrum well. Consequently, the pulse length was experimentally optimized to a duration of $20\,\mu\mathrm{s} \sim 4t_n$, and the power of the rf pulse was chosen to yield π-pulses for thermal atoms. The interstate scattering length between the $|1\rangle$ state and the $|3\rangle$ state is moderate $\sim -147a_0$, and the $|3\rangle$ state therefore acts as a weakly-interacting impurity state.

Importantly, transferred impurities in the $|3\rangle$ state perform fast spin-flip collisions with the medium atoms in the $|1\rangle$ state. This only removes a single medium atom for each impurity, whereas two medium atoms are lost for each impurity that remains in the $|2\rangle$ state. The impurity atoms are thus always lost and the experimental signal corresponds to an increase in medium atoms when the second rf pulse resonantly transfers impurities into the $|3\rangle$ state. When showing the spectral response of the system in the following, the number of atoms in the medium state is furthermore normalized to an area of one.

It is noteworthy that the ejection spectroscopy sequence allows for a variable evolution time. This enables ejection spectroscopy to investigate the timescales of bipolaron formation, however, a two-pulse scheme also inherently complicates the experiment. The first rf pulse in the ejection spectroscopy sequence populates not only the polaron ground state but also a continuum of excited states. Besides probing the polaron peak, the second rf pulse may thus transfer impurities from this tail of excited states into the $|3\rangle$ state at higher frequencies compared to the polaron peak. Furthermore, this second rf pulse also populates a tail of scattering states above the $|3\rangle$ state, which was previously used to extract the contact of the Bose polaron [70]. These excited states are populated for lower frequencies of the second rf pulse. For the ejection spectroscopy scheme, a polaron peak with a tail stretching towards both lower and higher frequencies is therefore expected to be observed. A peak at lower frequencies on top of this tail then constitutes a telltale sign of bipolarons.

5.3 Modelling the spectral function

Generally, the spectral function of the impurity $A(\omega)$ can be written as $A(\omega) = A_{\mathrm{P}}(\omega) + A_{\mathrm{cont}}(\omega)$ and contains both a polaron peak $A_{\mathrm{P}}(\omega)$ and a continuum of excited states $A_{\mathrm{cont}}(\omega)$. In this section, a recent diagrammatic description of the spectral function in the investigated system [84] is used to construct a physically motivated line shape function that models the rf response. This line shape function is then compared to observed injection and ejection spectra.

5.3.1 Injection spectrum

A diagrammatic approach can be used to investigate the spectral function of the impurity at arbitrary interaction strength, as discussed in Sec. 3.4. For injection spectroscopy, the spectral function depends on the relative angular frequency $\omega = 2\pi(f_0 - f)$, where f_0 is the atomic transition frequency between the $|1\rangle$ state and the $|2\rangle$ state and f is the applied frequency of the probe pulse. Furthermore, the model assumes the medium to be an ideal BEC and approximates the interactions between the impurity and the medium using a T-matrix approach [47]. For a homogeneous medium, this results in the following spectral function

$$A(\omega) = Z_\mathrm{P} 2\pi\delta(\omega - \omega_\mathrm{P}) + 8\pi \frac{\hbar^{3/2} n_\mathrm{B}}{m^{3/2}\omega^{5/2}} \frac{\Theta(\omega)}{1 + \frac{\hbar}{ma^2\omega}\left(1 - \frac{4\pi\hbar n_\mathrm{B} a}{m\omega}\right)^2}, \tag{5.1}$$

where Z_P is the quasiparticle residue, $\delta(x)$ is the Dirac delta function, $\hbar\omega_\mathrm{P}$ is the polaron energy and $\Theta(\omega)$ is the Heaviside step function. Equation (5.1) describes a polaron peak at ω_P with a continuum of excited states for $\omega > 0$. In the following, the variable is changed and instead the energy $E = \hbar\omega$ is used. Furthermore, since it is possible to excite states of a moving polaron and a Bogoliubov mode with arbitrarily small energies, the continuum is moved to start just above the polaron peak. Thus in the second term of Eq. (5.1), $\omega \to (E - E_\mathrm{P})/\hbar$ is replaced and one obtains

$$\begin{aligned} A(E) &= Z_\mathrm{P} 2\pi\delta((E - E_\mathrm{P})/\hbar) \\ &+ 8\pi \frac{\hbar^{3/2} n_\mathrm{B}}{m^{3/2}((E - E_\mathrm{P})/\hbar)^{5/2}} \frac{\Theta((E - E_\mathrm{P})/\hbar)}{1 + \frac{\hbar}{ma^2((E-E_\mathrm{P})/\hbar)}\left(1 - \frac{4\pi\hbar n_\mathrm{B} a}{m((E-E_\mathrm{P})/\hbar)}\right)^2}. \end{aligned} \tag{5.2}$$

For simplicity, the factors of each term in Eq. (5.2) are grouped together and the equation is rewriting as

$$A(E) = A_\mathrm{P}(E - E_\mathrm{P}) + A_\mathrm{cont}(E - E_\mathrm{P}), \tag{5.3}$$

where the polaron peak is given by

$$A_\mathrm{P}(E - E_\mathrm{P}) = Z_\mathrm{P} 2\pi\delta((E - E_\mathrm{P})/\hbar) \tag{5.4}$$

and the continuum of scattering state is given by

$$A_\mathrm{cont}(E - E_\mathrm{P}) = 8\pi \frac{\hbar^{3/2} n_\mathrm{B}}{m^{3/2}((E - E_\mathrm{P})/\hbar)^{5/2}} \frac{\Theta((E - E_\mathrm{P})/\hbar)}{1 + \frac{\hbar}{ma^2((E-E_\mathrm{P})/\hbar)}\left(1 - \frac{4\pi\hbar n_\mathrm{B} a}{m((E-E_\mathrm{P})/\hbar)}\right)^2}. \tag{5.5}$$

To model the injection spectrum, Eq. (5.3) is employed as a line shape function for the spectral response. The function is furthermore integrated over the density weighted by the BEC density distribution to account for the effect of the harmonic trapping potential. Here, the distribution of the density $f_n(n_\mathrm{B})$ is modelled in the Thomas-Fermi limit as $f_n(n_\mathrm{B}) \sim n_\mathrm{B}/n_{\mathrm{B,\,max}}\sqrt{1-n_\mathrm{B}/n_{\mathrm{B,\,max}}}$, where $n_{\mathrm{B,\,max}}$ is the medium density in the center of the atomic cloud. It is assumed that $n_\mathrm{B}/n_{\mathrm{B,\,max}} = E/E_{\mathrm{P,\,max}}$, where $E_{\mathrm{P,\,max}}$ is equivalently the energy of the polaron at maximum density. A similar assumption was made in Ref. [54] to obtain an empirical expression for the line shape of the polaron. Thus, the term corresponding to the integrated polaron peak follows a similar distribution $\sim E/E_{\mathrm{P,\,max}}\sqrt{1-E/E_{\mathrm{P,\,max}}}$. The term corresponding to the integrated continuum cannot as easily be solved and is therefore integrated numerically. Additionally, the spectral function is convoluted with a sinc function due to the square probe pulse of 20 µs duration. Finally, to compare Eq. (5.3) with data, values are required for the polaron energy at highest density and the quasiparticle residue. These parameters are obtained from previous reported spectroscopic results [54] for $E_{\mathrm{P,\,max}}$ and from a diagrammatic calculation [55] for Z_P.

The line shape function at $1/k_n a = -0.17$ is shown in Fig. 5.3 as a function of the impurity energy. The model reveals a polaron peak and a small scattering tail at higher energies. A series of minor peaks are visible in the line shape function, which is a result of convolving with the sinc function of the probing pulse.

Figure 5.3 also shows a measured injection spectrum. The data indicates a polaron peak just below zero and a tail stretching towards higher energies similarly to the modelled spectrum. No signs of the bipolaron are present in the injection spectrum. This is possibly due to a very small overlap between the initial state and the bipolaron state. In addition, the data contains more spectral weight both below the theoretically predicted polaron peak and in the continuum of excited states. Such broadening effects have also previously been observed in this system for impurity

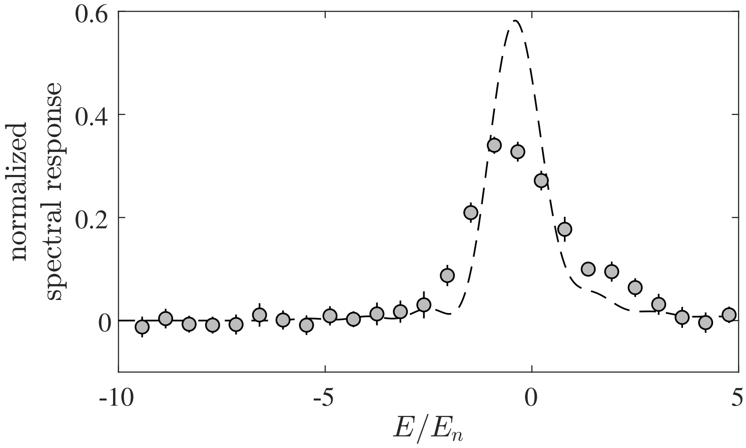

Figure 5.3: Injection spectrum at $1/k_n a = -0.17$. The measured normalized spectral response is shown as circles. The line shape function of Eq. (5.3), including experimental broadening from the density distribution and the Fourier width of the probing pulse, is shown as a dashed line.

fractions larger than 15% [37]. Nonetheless, the qualitative agreement between the data and the line shape function, where no free parameters have been included, does indicate that the model captures essential parts of the spectral response.

5.3.2 Ejection spectrum

The ejection spectroscopy sequence probes the rf response of the impurity by ejecting it into a weakly-interacting state using a second pulse. As discussed in Sec. 5.2, this complicates modelling the spectrum as an additional tail of excited states is expected to appear for lower energies. Moreover, a line shape function for the predicted bipolaron peak is required as well.

To model the full ejection spectrum of the polaron, one could ideally convolve the response of the first pulse with the response of the second pulse. However, the main concern is modelling the spectral response for negative energies, where the bipolaron peak is expected to be observed. At these energies, the two dominant contributions to the polaron spectrum are the polaron peak and the tail towards lower energies. For simplicity, the spectral function is therefore approximated with just the sum of these two. Specifically, the spectral function $A_\mathrm{P}(E-E_\mathrm{P})+A_\mathrm{cont}(-[E-E_\mathrm{P}])$ is used like that of Eq. (5.3), assuming that the scattering tail has a similar functional form but with a reversed direction. Here, the energy $E=h(\tilde{f}-\tilde{f}_0)$ is calculated using the frequency of the second pulse $\tilde{f}$ and the atomic transition frequency $\tilde{f}_0$ between the $|2\rangle$ state and the $|3\rangle$ state.

Finally, additional effects, such as a large impurity fraction, are considered. A simple solution to account for these is to include two free parameters in the form of amplitudes of the polaron peak $\mathscr{A}_\mathrm{P}$ and the continuum $\mathscr{A}_\mathrm{cont}$ as

$$A(E)=\mathscr{A}_\mathrm{P}A_\mathrm{P}(E-E_\mathrm{P})+\mathscr{A}_\mathrm{cont}A_\mathrm{cont}(-[E-E_\mathrm{P}]). \tag{5.6}$$

The distortion is thus modelled by a relative shift in spectral weight between the polaron peak and the excited states. Subsequently, the spectral line shape function is normalized to yield an integrated area of one.

To investigate this model, experimental observations are required for the fitting procedure. An ejection spectrum at $1/k_na=-0.17$ with evolution time $1\,\mu\mathrm{s}\sim0.2t_n$ is therefore shown in Fig. 5.4. The data displays a polaron peak and a tail of excited states towards lower energies. Observing a prominent polaron peak at so short evolution times indicates that polaron formation likely continues during the extent of the second rf

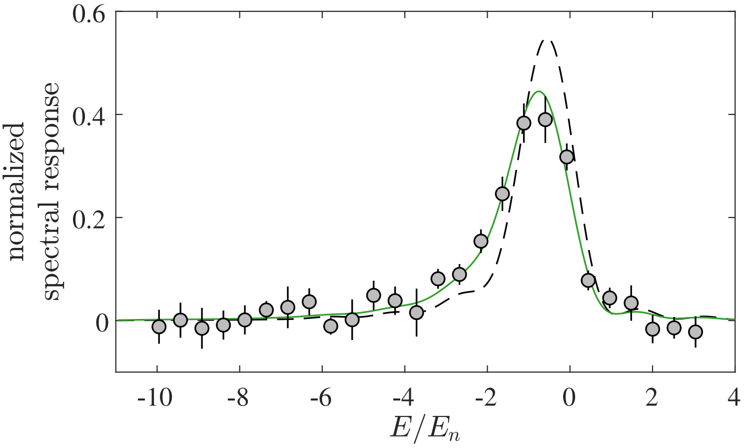

Figure 5.4: Ejection spectrum at $1/k_n a = -0.17$ with evolution time $1\,\mu s \sim 0.2 t_n$. The measured normalized spectral response is shown as circles. The line shape function function of Eq. (5.6) is fitted to the data and shown as a solid green line. The same function with no free parameters is shown as a dashed black line. Both models include experimental broadening from the density distribution and the Fourier width of the probing pulse.

pulse. However, no bipolaron peak is observed in the ejection spectrum, which permits using it to benchmark the polaronic spectral response.

Figure 5.4 also shows the line shape function of Eq. (5.6) without free parameters and fitted to the data for energies < 0. The model also includes experimental broadening effects due to the density distribution and the finite pulse length. A qualitative agreement is obtained between the plotted line shape function and the data, however, it is apparent that this model does not reproduce the observed spectral function completely. For the fitted line shape function, excellent agreement with the data is obtained even at positive energies. This benchmarks the fitted model, and the extracted amplitudes $\mathscr{A}_\mathrm{P}$ and $\mathscr{A}_\mathrm{cont}$ are subsequently fixed when analyzing ejection spectra at longer evolution times.

Finally, the spectral response of bipolarons is considered. This is expected to correspond to a small peak on top of the scattering tail of the polaron. Therefore, the bipolaronic rf response is simply modelled as a peak at its ground state energy [57] in the form of a Dirac delta function and the bipolaronic excitation spectrum is neglected. The line shape function is thus written as

$$A_\mathrm{BP}(E-E_\mathrm{BP}) = 2\pi\delta((E-E_\mathrm{BP})/\hbar), \tag{5.7}$$

where E_BP is the bipolaron energy. To obtain the spectral response at finite evolution time, Eq. (5.7) is added to Eq. (5.6) and relative amplitudes are included, since the spectral weight of the bipolaron peak is unknown. For a single density, this results in the following spectral function for energies $E < 0$

$$A(E) = \alpha\big(\mathscr{A}_\mathrm{P} A_\mathrm{P}(E-E_\mathrm{P}) + \mathscr{A}_\mathrm{cont} A_\mathrm{cont}(-[E-E_\mathrm{P}])\big) + \beta A_\mathrm{BP}(E-E_\mathrm{BP}). \tag{5.8}$$

Here α and β are free parameters which characterize the amplitude of the impurity and bipolaronic spectral response, respectively.

To accurately model the experiment, Eq. (5.8) is integrated over the density weighted by the density distribution of the condensate. For the integrated bipolaronic term, this yields a distribution of energies $\sim E/E_\mathrm{BP,\,max}\sqrt{1-E/E_\mathrm{BP,\,max}}$ similarly to that of the polaron peak, where $E_\mathrm{BP,\,max}$ is the bipolaron energy in the center of the atomic cloud. Furthermore, the model is convoluted with a sinc function due to the finite pulse length and normalized to an area of one. Importantly, the spectral response of bipolarons is thus described by only two parameters being its amplitude β and the energy of the deepest bound bipolaron $E_\mathrm{BP,\,max}$.

With Eq. (5.8), a physically motivated line shape function, containing a polaron peak, a continuum of excited states and a bipolaron peak, has now been constructed. The spectral contributions from the polaron and the scattering tail have been compared with an injection spectrum and an ejection spectrum at short evolution time. Clear agreement between a fit and the data was obtained when amplitudes for the polaron peak $\mathscr{A}_\mathrm{P}$ and the continuum $\mathscr{A}_\mathrm{cont}$ were included. In the following sections, these two amplitudes are fixed at their extracted values as the dynamical formation of the bipolaron is investigated at longer evolution times.

5.4 Formation of bipolarons

Bipolarons are formed when polarons interact through the density of the medium. An experimental approach to investigate bipolarons using ejection spectroscopy was discussed in Sec. 5.2, and in Sec. 5.3 a physically motived line shape function was introduced. In this section, the first experimental observations of bipolarons are presented and the formation time is obtained. Furthermore, the effects of the impurity fraction are discussed.

5.4.1 Bipolaronic spectral response

The formation of polarons has been shown to occur at times $\sim t_n = \hbar / E_n$ at large interaction strengths, as discussed in Chap. 4. For bipolarons to form dynamically, it is thus expected that evolution times longer than t_n are required. A spectrum at $t > t_n$ is therefore investigated in order to observe a spectral signature of bipolarons.

An ejection spectrum is shown in Fig. 5.5 at interaction strength $1/k_n a = -0.17$ with evolution time $33\,\mu\mathrm{s} \sim 6 t_n$. Here, the measured spectral response displays a polaron peak and a continuum of scattering states similarly to the ejection spectrum with short evolution time shown in Fig. 5.4. However, the spectrum in Fig. 5.5 furthermore contains a peak at negative energies. This peak is attributed to the spectral response of bipolarons, which are expected to have a larger binding energy than po-

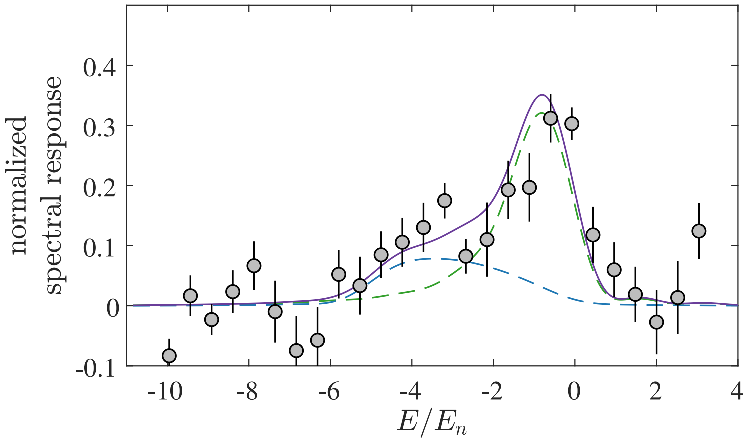

Figure 5.5: Ejection spectrum at $1/k_n a = -0.17$ with evolution time 33 µs $\sim 6t_n$. The measured normalized spectral response is shown as circles. The line shape function function of Eq. (5.8), with additional broadening from the inhomogeneous density and the finite pulse length, is fitted to the data and shown as a solid purple line. The contribution from the polaron peak and continuum is indicated with a dashed green line and the contribution from the bipolaron is indicated with a dashed blue line.

larons. The peak is broad since the energies span from the deepest bound bipolarons at highest density to the very loosely bound bipolarons close to the edge of the atomic cloud.

The line shape model of Eq. (5.8) is fitted to the data for energies < 0. This fit is also shown in Fig. 5.5 and captures the behavior of the data well, especially for lower energies where the bipolaron peak is present. The fit only contains the two amplitudes α and β as free parameters, whereas the energies of the polarons and bipolarons are fixed. Thus, the agreement highlights how well the previous spectroscopic result describes the energy of the deepest bound polaron and, importantly, how well the diagrammatic model describes the energy of the deepest bound bipolaron.

5.4.2 Dynamical formation

To investigate the timescale of bipolaron formation, ejection spectra at various evolution times are acquired and each data set is fitted with Eq. (5.8). The only free parameters are the amplitudes α and β. By extracting the relative amplitude of the bipolaron as $\tilde{\beta} = \beta/\alpha$ at each evolution time, a reliable measure of the amount of bipolarons formed up to this specific time is then obtained.

The extracted relative amplitude $\tilde{\beta}$ of the bipolaron peak is shown in Fig. 5.6 as a function of evolution time. The data sets are obtained at interaction strength $1/k_n a = -0.17$ and with an impurity fraction of 17% relative to the total amount of atoms. The relative amplitude reveals a gradual increase with increasing evolution time, until it settles after $\sim 6t_n$. The second data point at $t/t_n = 0.5$ deviates from this trend, which could be due to the quality of that data set or the fit to it. Nonetheless, the behavior of the data provides an indication of bipolarons dynamically forming as polarons gradually begin interacting with each other through the medium.

To analyze the formation of bipolarons, a simple model is now constructed and fitted to the data. The aim is not to gain a complete understanding, but merely to provide some insight in the timescale of bipolaron formation. For capturing the behavior of the bipolaronic relative amplitude, an exponential function saturating at a given offset, representing the equilibrated amount of bipolarons in the system, is a reasonable choice of a simple fitting function. Naively, this model is therefore used for the formation of bipolarons to obtain an estimate of the formation time. Thus, the fitting function contains a characteristic timescale t_{form}

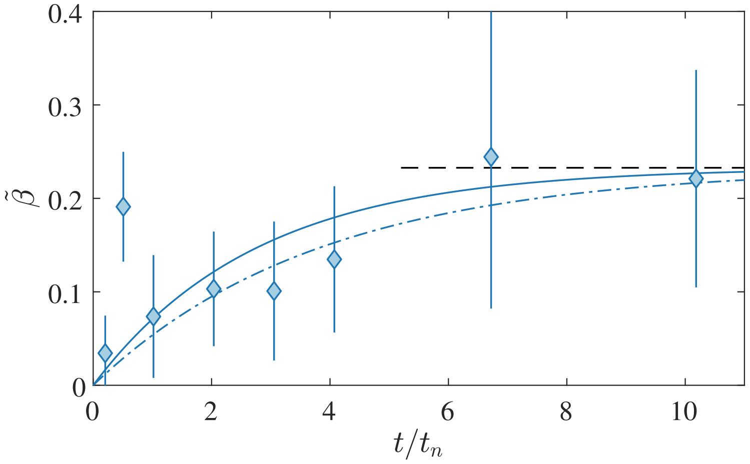

Figure 5.6: Relative amplitude of the bipolaron peak. The data is obtained at interaction strength $1/k_n a = -0.17$ and with a fraction of 17% impurities relative to the total number of atoms. The extracted relative amplitude is shown as blue diamonds. To analyze the observed behavior, Eq. (5.9) is fitted to the data. A fit using all data points is shown as a solid blue line and a fit excluding the second data point at $t/t_n = 0.5$ is shown as a dash-dotted blue line. The equilibrated relative amplitude $\tilde{\beta}_0$ is indicated as a dashed black line.

as a free parameter and is written as

$$\tilde{\beta}(t) = (1 - e^{-t/t_{\text{form}}})\tilde{\beta}_0, \tag{5.9}$$

where $\tilde{\beta}_0$ is a fixed parameter describing the equilibrated relative amplitude. This parameter is extracted from the average of the last two data points.

A fit of Eq. (5.9) to the extracted relative amplitude is shown in Fig. 5.6. The fit displays an initial increase in $\tilde{\beta}$, before it slowly approaches $\tilde{\beta}_0$.

From the fit, a formation time of $t_{\text{form}} = 3(3)\,t_n$ is extracted. This is approximately twice as long as the previously observed transition time to the many-body regime $\sim 1.4\,t_n$ for polarons [84, 94], indicating fast subsequent formation of bipolarons. The general good agreement between the data and the fit, with only a single free parameter, reveals that the simple model captures some of the underlying processes in bipolaron formation.

To investigate how much the second data point at $t/t_n = 0.5$ influences the fit quality, another fit is applied to the observations excluding this data point. This fit is also shown in Fig. 5.6 in good agreement with the data. It is apparent that the included data points are closer to this fitted line and more evenly spread around it as compared to the previous fit, which indicates a lower systematic error. Furthermore, the fit yields an extracted formation time of $t_{\text{form}} = 4(1)\,t_n$, where the smaller fitting error again suggest that the fit more consistently captures the behavior of the data.

The formation timescale is now estimated by considering the time required for two impurities to encounter each other. At large interaction strengths close to the resonance, the density-limited timescale t_n governs decoherence processes of impurities in the two-body universal regime [84]. Therefore, t_n is used as the time associated with collisions between an impurity and another atom in the following. For an impurity fraction of 17%, the probability that the encountered atom is an impurity as well is $0.17/(1-0.17) \sim 0.21$. To ensure unity probability of two impurity atoms interacting with each other, a total number of $1/0.21 \sim 4.8$ collisions are required. Thus, the formation timescale of bipolarons at an impurity fraction of 17% is estimated to be $t_{\text{form,calc}} \sim 4.8\,t_n$. This value is slightly higher than the two extracted formation times. However, $t_{\text{form, calc}}$ is within error bars of both fitted values, which indicates that this estimate elucidates some parts of the mechanism and timescale of bipolaron formation.

5.4.3 Effects of the impurity fraction

The effects of the impurity concentration in the system are important to consider. Evidently, one of the most prominent consequences have already been observed, namely the bound state of a bipolaron formed through the induced interactions between two polarons. To observe how the impurity fraction influences the formation of bipolarons, a data set similar to the one shown in Fig. 5.6 is obtained, but using a slightly longer initial rf pulse yielding a larger impurity fraction of 27%. Again, the spectrum obtained at an evolution time of $0.2\,t_n$ is fitted with Eq. (5.6), and $\mathscr{A}_\mathrm{P}$, $\mathscr{A}_\mathrm{cont}$ are extracted for this impurity fraction. Subsequently they are fixed, when fitting the data at various evolution times with Eq. (5.8).

The extracted relative amplitude $\tilde{\beta}$ for an impurity fraction of 27% at $1/k_n a = -0.16$ is shown in Fig. 5.7. This displays an initial increase with increasing evolution time, whereafter it settles at times $\sim 3\,t_n$. The behavior thus indicates faster formation of bipolarons at this higher concentration of impurities, as compared to Fig. 5.6. This difference qualitatively agrees with the expectation, that the likelihood of two polarons encountering and binding with each other increases, when the amount of impurities in the system is larger.

A fit of the data with Eq. (5.9) is also shown in Fig. 5.7 and display initial increase and subsequent equilibration. The fit yields an extracted formation time of $t_\mathrm{form} = 2(2)\,t_n$. This value may be compared to the estimated formation time, which is $t_\mathrm{form,calc} \sim 2.7\,t_n$ calculated using an impurity fraction of 27%. The estimated time is thus again within error bars of the fitted formation time.

The fitted formation time of Fig. 5.7 can also be compared to the fitted times of Fig. 5.6. This comparison reveals that they are all within error bars of each other. Therefore, no substantial difference is observed in the fitted formation times of the two data sets at different impurity fractions. Nonetheless, the simplicity of these fits suggests that the model may be used preliminary for further investigations of the bipolaronic

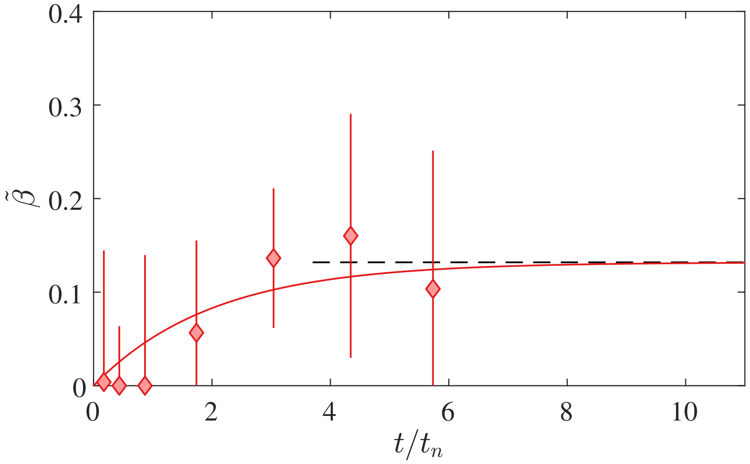

Figure 5.7: Relative amplitude of the bipolaron peak. The data is obtained at interaction strength $1/k_n a = -0.16$ and impurity fraction 27% relative to the total number of atoms, and the measured relative amplitude is shown as red diamonds. Equation (5.9) is fitted to the data and shown as a solid red line, and the equilibrated relative amplitude $\tilde{\beta}_0$ is indicated as a dashed black line.

formation time. These investigations should be conducted at smaller or larger concentration of impurities to possibly observe a dependence of the formation time on the impurity fraction.

Related studies of effects due to the impurity fraction have been carried out in the same system. For previous spectroscopic investigations, larger impurity fractions were observed to distort the rf spectrum [37] similarly to the broadening effects discussed in Sec. 5.3. For interferometric measurements, no effect was reported for the behavior of impurity dynamics at $1/k_n a = -1$ for varying impurity fractions [84]. However, since the bipolaron is predicted to exist only at sufficiently large interaction strengths [57], this may explain the lack of observed effects at the interferometrically investigated interaction strength. Thus, the measurements presented in this section do not conflict with previously reported results.

5.5 Bipolaron energy at strong attractive interactions

The bipolaron investigated in Ref. [57] is predicted to exhibit a significant shift in energy with increasing interaction strength. Whereas the polaron energy is only $\sim E_n$ at unitarity [37, 38, 54], the bipolaron energy is expected to approach several E_n. To investigate this behavior, the spectral response of bipolarons at various attractive interaction strengths is measured. The explored interval of interaction strengths is limited by the bipolaron peak being indistinguishable from the polaron peak (especially the tail of excited states) for intermediate interaction strengths $|1/k_n a| > 0.25$. The obtained data sets are fitted with Eq. (5.8), where the amplitudes α, β and the bipolaron energy at maximum density $E_{\mathrm{BP,\,max}}$ are free parameters. Thus, the bipolaron energy across attractive interaction strengths is traced.

The fitted bipolaron energies are shown in Fig. 5.8 as a function of the inverse interaction strength. All measurements are performed using a first pulse of $0.2t_n$ duration. Furthermore, an evolution time of $\sim 5t_n$ is employed to allow for sufficient interaction time. The extracted bipolaron energy shows a decrease for increasing interaction strength and ranges from $-4E_n$ at $1/k_n a = -0.21$ to $\sim -8E_n$ at $1/k_n a = -0.09$, where only the data point closest to the resonance at $1/k_n a = -0.05$ diverges from this trend with an observed bipolaron energy of $\sim -6E_n$.

It is important to realize that the decay rate of the impurity atoms are considerable at these large interaction strengths [84, 94], which is

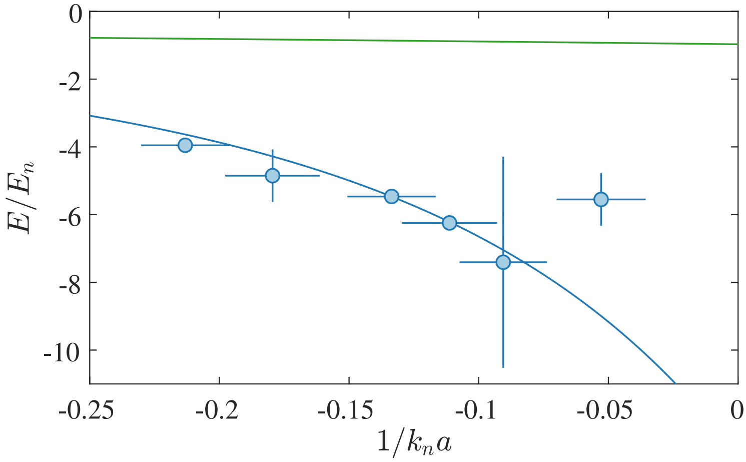

Figure 5.8: Energy of the bipolaron at large attractive interaction strengths. The extracted bipolaron energy at maximum density is shown as blue circles for an impurity fraction of $\sim 20\%$. Horizontal error bars stem from the uncertainty of the density and the scattering length. Vertical error bars are 1σ confidence intervals of the fitted value, which for some data points are smaller than the marker. The predicted bipolaron energy [57] is shown as a solid blue line and the previously observed polaron energy [54] as a solid green line.

especially true in the center of the atomic cloud where fast losses may consequently occur during the evolution time. This effectively decreases the observed energy and may contribute to obscure the observations at the largest interaction strengths. Nonetheless, the clear shift in the energy of the bipolarons is in qualitative agreement with the expectation of deeper bound bipolarons with increasing interaction strength.

Figure 5.8 also shows the previously measured polaron energy [54] and the diagrammatic predicted bipolaron energy [57]. The polaron energy is relatively small for this interval of interaction strengths, whereas the predicted bipolaron energy extends from $-3E_n$ to $-11E_n$. Importantly, excellent agreement is obtained between the data and the diagrammatic description besides the discrepancy very close to unitarity. This provides clear evidence that the observed peak behaves like a bipolaron and consolidates the theoretical understanding.

The dynamical formation of bipolarons and their energy dependence at large attractive interaction strengths have thus been explored using ejection spectroscopy. The observations have revealed a clear signature of bipolarons in the system, and in the following section the quasiparticle residue of both polarons and bipolarons is investigated using a similar experimental approach.

5.6 Quasiparticle residue

The quasiparticle residue of the polaron describes the spectral weight of the polaron peak and can be calculated as the overlap between the non-interacting and the interacting impurity state. In Ref. [29] it was observed for the Fermi polaron using rf spectroscopy, and subsequently it has been determined from Rabi oscillations between the interacting and non-interacting impurity state [30, 32]. For the Bose polaron it has been studied both perturbatively [49], variationally [50] and diagrammatically [47, 55], however, so far it has not been observed experimentally.

To investigate the residue of the polaron and bipolaron, Rabi oscillations between the $|2\rangle$ state and $|3\rangle$ state are realized using an experimental method similar to that of ejection spectroscopy discussed in Sec. 5.2. The experimental sequence is as follows. An initial short rf pulse with length $0.2t_n$ transfers population into the $|2\rangle$ state whereafter the system evolves for a duration of $\sim 2t_n$. This time is chosen to allow significant formation of both polarons and bipolarons but reduce the effect of losses during the evolution. Subsequently, a second rf pulse couples the $|2\rangle$ and the

$|3\rangle$ state. Previously, the chosen pulse length was $20\,\mu\mathrm{s} \sim 4t_n$, the power of the pulse was adjusted to yield π-pulses for thermal atoms, and the frequency was varied to obtain the spectral response of the impurity. However, a pulse at full power is now applied and the pulse duration is varied. This drives Rabi oscillations between the impurity state and the $|3\rangle$ state. The atomic response can be observed as a corresponding oscillation in the number of atoms in the medium state. By extracting this oscillation frequency Ω relative to the Rabi frequency of thermal atoms Ω_0, it is then possible to determine the parameter $(\Omega/\Omega_0)^2$.

The observed number of medium atoms as a function of the pulse length is shown in Fig. 5.9 at $1/k_n a = -0.4$. The data sets are obtained using a pulse resonant with the average polaron energy [54], shown in Fig. 5.9(a), and with the experimentally observed average bipolaron energy, shown in Fig. 5.9(b). Both panels clearly display an oscillating atom number as a signature of cyclic behavior of the impurities between two states. The oscillation amplitudes are damped for longer pulse durations as coherence is lost in the system. The oscillations appear to be faster in Fig. 5.9(b). This initially seems counter-intuitive, since bipolarons are expected to exhibit a lower residue compared to polarons and thus a lower Rabi frequency and slower oscillations. However, the cyclic behavior in Fig. 5.9(b) can also be attributed to polarons oscillating due to a rf field with a detuning Δ, which results in a higher general Rabi frequency $\tilde{\Omega} = \sqrt{\Omega^2 + \Delta^2}$. This distinction will be further investigated in the following.

To analyze the oscillations, the atom numbers of Fig. 5.9 are fitted with a damped, sinusoidal function of the form

$$N(t) = A_\mathrm{R} e^{-t/\tau_\mathrm{R}} \sin\left(\Omega(t - t_{\mathrm{R},0})\right) + N_{\mathrm{R},0}, \tag{5.10}$$

where the amplitude A_R, damping time τ_R, angular frequency Ω, phase $t_{\mathrm{R},0}$ and offset $N_{\mathrm{R},0}$ are free parameters. The resulting fits according to Eq. (5.10) are also shown in Fig. 5.9. Generally, the fits capture both the os-

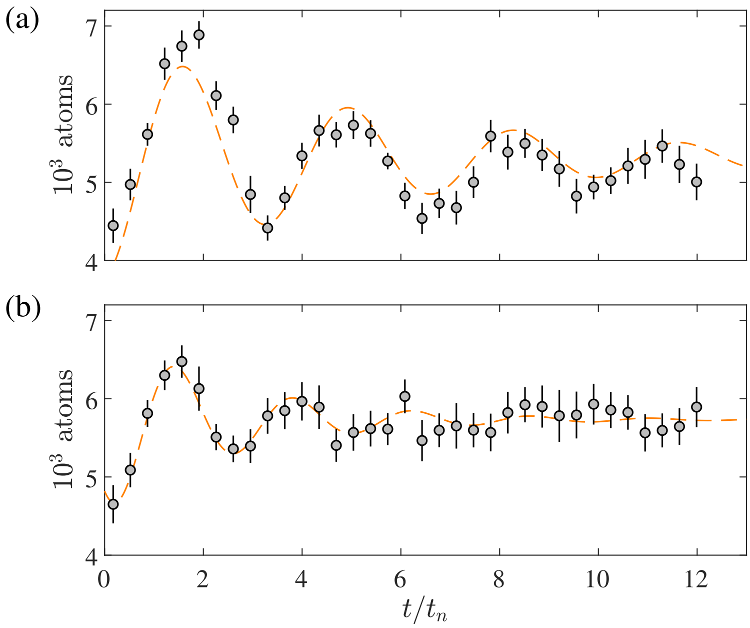

Figure 5.9: Rabi oscillations of impurities at interaction strength $1/k_n a = -0.4$. A pulse of duration t/t_n drives oscillations between the impurity state and the weakly-interacting $|3\rangle$ state. The observed number of medium atoms are shown as circles for a pulse resonant with the average polaron energy (a) and bipolaron energy (b). A damped sinusoidal fit is shown as a dashed orange line.

cillatory behavior and the damping well. This underlines the applicability of the Rabi model.

The fit shown in Fig. 5.9(a) yields an extracted Rabi frequency of $\Omega = 2\pi \times 1.88(9) E_n/\hbar$. Using this value and the independently measured Rabi frequency of thermal atoms $\Omega_0 = 2\pi \times 1.936(4) E_n/\hbar$, the squared fraction is determined to be $(\Omega/\Omega_0)^2 = 0.94(9)$.

If this parameter is affiliated with the quasiparticle residue of the polaron Z_P, it is possible to compare it with expectations. The value is below one as expected but is slightly higher than a predicted value of 0.784(3) from a recent diagrammatic study [55], where the error stems from experimental uncertainties of the density and scattering length. The predicted value is the residue for a polaron at average energy in a homogeneous medium. However experimentally, the inhomogeneous density causes many polaron states at different energies to be involved in the oscillations. Since the frequency of the second rf pulse is chosen to be resonant with the average polaron energy, a large number of these polaron states experience the pulse as having a slight detuning leading to faster oscillations. The apparent discrepancy between the predicted and the extracted values may therefore be attributed to this effect.

The oscillations shown in Fig. 5.9(b) are now investigated. Here, the fitted Rabi frequency is $\Omega = 2\pi \times 2.6(1) E_n/\hbar$, which is higher than the frequency of the oscillations in Fig. 5.9(a). If the quasiparticle residue of the bipolaron is naively estimated using this value, an unphysical value of $Z_\mathrm{BP} = 1.8(2)$ is obtained. To analyze if the oscillations in Fig. 5.9(b) are instead primarily caused by polarons experiencing a detuned rf field, the general Rabi frequency is calculated using the already extracted Rabi frequency for resonant polaron oscillations. The detuning is given by the difference between the average polaron energy and the energy of the pulse, which for the data set shown in Fig. 5.9(b) corresponds to $\Delta = 2\pi \times 1.4 E_n/\hbar$. Thus, the general Rabi frequency is calculated to be $\tilde{\Omega}_\mathrm{calc} = 2\pi \times 2.37(7) E_n/\hbar$, which is slightly lower than the fitted frequency of $2\pi \times 2.6(1) E_n/\hbar$. However, the two values almost agree within error bars indicating that the fast oscillations observed in Fig. 5.9(b) may in fact also be caused by polarons. It is therefore difficult to draw any clear conclusions based on these oscillations, since many processes may be involved in the behavior of the data.

The observations presented in Fig. 5.9 represent the first measurements of Rabi oscillations with Bose polarons, and though no exact agreement is obtained between the extracted and predicted quasiparticle residue, the estimated value is below one as expected. An interesting continuation of this investigation is to measure the Rabi frequency across various attractive interaction strengths. This could possibly display the behavior of the residue, which is predicted to decrease with increasing interaction strength. Furthermore, better agreement with theoretical descriptions is expected if the observations are restricted to the Rabi response of polarons with similar energies. Such investigations are possible using a BEC trapped in a uniform potential with a homogeneous medium density [103, 104] or using spatial resolution similarly to recent spectroscopic measurements of the Bose polaron [70].

5.7 Summary

In summary, this chapter has presented the first experimental evidence of bipolarons in a Bose-Einstein condensate. A physically motivated spectral line shape function was constructed and compared with an injection spectrum and an ejection spectrum for short evolution time, clearly showing a polaron peak and a tail of excited states. For longer evolution times, a bipolaron peak was observed to emerge at the predicted energy. This allowed measuring the dynamical formation of bipolarons, which was investigated at two impurity fractions. Moreover, the energy of the bipolaron at maximum density was extracted at various attractive interaction strengths in excellent agreement with theoretical predictions. Finally, the quasiparticle residue of the polaron was measured using a similar experimental scheme.

These investigations have been conducted using a higher impurity fraction than previous polaron studies [37, 38, 70, 84]. However, these were primarily concerned with the properties of single impurities and effective interactions between polarons were unwanted, since they could distort the experimental signal. To allow formation and observation of bipolarons, it is inherently necessary to use a larger impurity fraction. Increasing the fraction further to the limit of quantum mixtures and observing how the properties of the system change, constitutes an interesting extension of the experimental research. This could elucidate a possible breakdown of the impurity quasiparticle framework.

CHAPTER 6

CONCLUSION AND OUTLOOK

In this thesis, impurity dynamics in ultracold gases was investigated. Experiments were performed with interacting impurities immersed in Bose-Einstein condensates and their dynamical evolution was observed. In particular, these investigations permitted measuring the dynamical formation of both polarons and bipolarons in Bose-Einstein condensates, and the observations were successfully compared with theoretical models.

In Chap. 2, ultracold quantum gases and polarons were reviewed. Important concepts such as condensation of bosons, interactions between ultracold atoms and quasiparticle models were considered. Furthermore, recent experimental studies of both Fermi and Bose polarons were discussed.

Chapter 3 introduced and presented two publications reporting the first observations of formation dynamics of the Bose polaron at attractive interaction strengths [84, 85]. These experiments were conducted in ^{39}K BECs using a Ramsey-like interferometric sequence. In the first publication, three regimes of impurity dynamics, depending on both the interaction strength between medium and impurity and the evolution time, were observed experimentally. Excellent agreement between theory and experimental data was obtained at all interaction strengths. The second publication expanded this work with a thorough investigation of the two initial regimes. This included analyzing the extracted transition times and obtaining the functional behavior of the dynamics in the two regimes.

Chapter 4 analyzed and compared interferometric and spectroscopic polaron results. In particular, the notion of repulsive impurity dynamics, the instantaneous energy of the impurity and the timescales of the Bose polaron were introduced. Furthermore, a publication [94] was presented which investigated these concepts in greater detail. This included a measurement of impurity dynamics at repulsive interaction strengths indicating the presence of two polaron branches. Moreover, it showed the interferometrically extracted instantaneous energy of the impurity and compared it with previous spectroscopic polaron results yielding good agreement. Finally, the publication presented an analysis of the polaronic timescales revealing a well-defined quasiparticle at all interaction strengths.

In Chap. 5, the effective interactions between polarons and the emergence of bipolarons were examined. A physically motivated line shape function was constructed and compared with experimental data yielding clear evidence of bipolarons. The formation time was then extracted and subsequently the bipolaron energies at large attractive interaction strengths were obtained in excellent agreement with predicted values. Finally, an estimate of the quasiparticle residue of the polaron was extracted, while a similar measurement did not provide the residue of the bipolaron.

6.1 Outlook

Based on these observations of impurity dynamics in a BEC, the stage is set for further investigations. These include the extension of current studies by improving the experimental apparatus and the exploration of new aspects of impurity physics.

One large obstacle for the current investigations of the Bose polaron, is the harmonic trapping potential, which results in an inhomogeneous density of the medium. This leads to a distribution of polaron energies from the deepest bound polaron in the center of the trap to the weakly interacting polaron in the edges of the cloud at vanishing density. This problem can be circumvented by using analytic tools to extract the properties of the polaron at maximum density [54] or using spatial resolution [70]. However, employing a uniform trapping potential to produce a homogeneous density of the medium would greatly simplify the experiments. Moreover, such a box trap [103, 104] may reduce dephasing effects for interferometric measurements and enable investigations further into the many-body regime or at repulsive interaction strengths. Additionally, this trap may provide better experimental settings for measuring the quasiparticle reside of the polaron and allow a more precise comparison with theoretical predictions.

Investigations of the Bose polaron in the unitary regime are especially intriguing, since the scattering length diverges and the interactions are limited by the density. A recent study investigated how the Efimov trimer influences the energy at these unitary interactions [51]. Observing such a dependence constitutes an exciting experiment, which is possible by measuring the polaron energy at unitarity with various densities of the condensate.

Impurity physics in lower dimensions also represents an interesting research avenue. In lower dimensions quantum fluctuations are enhanced, however, long-range order of the medium also suffers from going to lower dimensions where it is not necessarily possible to obtain a Bose-Einstein condensate. Nonetheless, it is possible to achieve quasi-long range order in two-dimensional Bose gases [105], which therefore pose as an ideal platform for studying lower dimensionality polaron physics. While the Fermi polaron has been studied in two dimensions [31], the Bose polaron has only been investigated in one dimension [63]. It is therefore intriguing to experimentally realize the two-dimensional Bose polaron and compare observations with recent theoretical predictions [106–108].

To summarize, the results presented in this thesis have improved and consolidated the current understanding of both Bose polarons and bipolarons. The presented experimental platform moreover suggests new ways of investigating quantum impurities with prospects of observing novel physics with exciting results.

BIBLIOGRAPHY

[1] M. K. E. L. Planck, Zur Theorie des Gesetzes der Energieverteilung im Normalspectrum, Verhandl. Dtsc. Phys. Ges. **2**, 237 (1900).

[2] N. Bohr, On the constitution of atoms and molecules, The London, Edinburgh, and Dublin Philosophical Magazine and Journal of Science **26**, 1–25 (1913).

[3] M. Head-Gordon, Quantum chemistry and molecular processes, The Journal of Physical Chemistry **100**, 13213–13225 (1996).

[4] J. Cao, R. J. Cogdell, D. F. Coker, H.-G. Duan, J. Hauer, U. Kleinekathöfer, T. L. C. Jansen, T. Mančal, R. J. D. Miller, J. P. Ogilvie, V. I. Prokhorenko, T. Renger, H.-S. Tan, R. Tempelaar, M. Thorwart, E. Thyrhaug, S. Westenhoff, and D. Zigmantas, Quantum biology revisited, Science Advances **6** (2020).

[5] T. H. Maiman, Stimulated optical radiation in ruby, Nature **187**, 493–494 (1960).

[6] J. Bardeen, and W. H. Brattain, The transistor, a semi-conductor triode, Phys. Rev. **74**, 230–231 (1948).

[7] R. P. Feynman, Simulating physics with computers, International Journal of Theoretical Physics **21**, 467–488 (1982).

[8] J. P. Dowling, and G. J. Milburn, Quantum technology: the second quantum revolution, Phil. Trans. R. Soc. Lond. A **361**, 1655–1674 (2003).

[9] S. N. Bose, Plancks gesetz und lichtquantenhypothese, Z. Phys. **26**, 178–181 (1924).

[10] A. Einstein, Quantentheorie des einatomigen idealen Gases, zweite Abhandlung, Sitzungsber. Kgl. Preuss. Akad. Wiss. **1**, 3–14 (1925).

[11] M. H. Anderson, J. R. Ensher, M. R. Matthews, C. E. Wieman, and E. A. Cornell, Observation of Bose-Einstein condensation in a dilute atomic vapor, Science **269**, 198–201 (1995).

[12] C. C. Bradley, C. A. Sackett, J. J. Tollett, and R. G. Hulet, Evidence of Bose-Einstein condensation in an atomic gas with attractive interactions, Phys. Rev. Lett. **75**, 1687–1690 (1995).

[13] K. B. Davis, M. .-.-O. Mewes, M. R. Andrews, N. J. van Druten, D. S. Durfee, D. M. Kurn, and W. Ketterle, Bose-Einstein condensation in a gas of sodium atoms, Phys. Rev. Lett. **75**, 3969–3973 (1995).

[14] B. DeMarco, and D. S. Jin, Onset of Fermi degeneracy in a trapped atomic gas, Science **285**, 1703–1706 (1999).

[15] F. Pereira Dos Santos, J. Léonard, J. Wang, C. J. Barrelet, F. Perales, E. Rasel, C. S. Unnikrishnan, M. Leduc, and C. Cohen-Tannoudji, Bose-Einstein condensation of metastable helium, Phys. Rev. Lett. **86**, 3459–3462 (2001).

[16] S. Kraft, F. Vogt, O. Appel, F. Riehle, and U. Sterr, Bose-Einstein condensation of alkaline earth atoms: ^{40}Ca, Phys. Rev. Lett. **103**, 130401 (2009).

[17] T. Fukuhara, S. Sugawa, and Y. Takahashi, Bose-Einstein condensation of an ytterbium isotope, Phys. Rev. A **76**, 051604 (2007).

[18] M. Lu, N. Q. Burdick, S. H. Youn, and B. L. Lev, Strongly dipolar Bose-Einstein condensate of dysprosium, Phys. Rev. Lett. **107**, 190401 (2011).

[19] D. C. Aveline, J. R. Williams, E. R. Elliott, C. Dutenhoffer, J. R. Kellogg, J. M. Kohel, N. E. Lay, K. Oudrhiri, R. F. Shotwell, N. Yu, and R. J. Thompson, Observation of Bose–Einstein condensates in an Earth-orbiting research lab, Nature **582**, 193–197 (2020).

[20] I. Bloch, J. Dalibard, and S. Nascimbène, Quantum simulations with ultracold quantum gases, Nature Physics **8**, 267–276 (2012).

[21] L. Tanzi, E. Lucioni, F. Famà, J. Catani, A. Fioretti, C. Gabbanini, R. N. Bisset, L. Santos, and G. Modugno, Observation of a dipolar quantum gas with metastable supersolid properties, Phys. Rev. Lett. **122**, 130405 (2019).

[22] F. Böttcher, J.-N. Schmidt, M. Wenzel, J. Hertkorn, M. Guo, T. Langen, and T. Pfau, Transient supersolid properties in an array of dipolar quantum droplets, Phys. Rev. X **9**, 011051 (2019).

[23] L. Chomaz, D. Petter, P. Ilzhöfer, G. Natale, A. Trautmann, C. Politi, G. Durastante, R. M. W. van Bijnen, A. Patscheider, M. Sohmen, M. J. Mark, and F. Ferlaino, Long-lived and transient supersolid behaviors in dipolar quantum gases, Phys. Rev. X **9**, 021012 (2019).

[24] J. R. M. de Nova, K. Golubkov, V. I. Kolobov, and J. Steinhauer, Observation of thermal Hawking radiation and its temperature in an analogue black hole, Nature **569**, 688–691 (2019).

[25] L. D. Landau, and S. I. Pekar, Effective mass of a polaron, Zh. Eksp. Teor. Fiz. **18**, 419 (1948).

[26] M. E. Gershenson, V. Podzorov, and A. F. Morpurgo, *Colloquium*: electronic transport in single-crystal organic transistors, Rev. Mod. Phys. **78**, 973–989 (2006).

[27] A. S. Alexandrov, and N. F. Mott, Bipolarons, Reports on Progress in Physics **57**, 1197–1288 (1994).

[28] C. Chin, R. Grimm, P. Julienne, and E. Tiesinga, Feshbach resonances in ultracold gases, Rev. Mod. Phys. **82**, 1225–1286 (2010).

[29] A. Schirotzek, C.-H. Wu, A. Sommer, and M. W. Zwierlein, Observation of Fermi polarons in a tunable Fermi liquid of ultracold atoms, Phys. Rev. Lett. **102**, 230402 (2009).

[30] C. Kohstall, M. Zaccanti, M. Jag, A. Trenkwalder, P. Massignan, G. M. Bruun, F. Schreck, and R. Grimm, Metastability and coherence of repulsive polarons in a strongly interacting Fermi mixture, Nature **485**, 615–618 (2012).

[31] M. Koschorreck, D. Pertot, E. Vogt, B. Fröhlich, M. Feld, and M. Köhl, Attractive and repulsive Fermi polarons in two dimensions, Nature **485**, 619–622 (2012).

[32] F. Scazza, G. Valtolina, P. Massignan, A. Recati, A. Amico, A. Burchianti, C. Fort, M. Inguscio, M. Zaccanti, and G. Roati, Repulsive Fermi polarons in a resonant mixture of ultracold ^{6}Li atoms, Phys. Rev. Lett. **118**, 083602 (2017).

[33] Z. Yan, P. B. Patel, B. Mukherjee, R. J. Fletcher, J. Struck, and M. W. Zwierlein, Boiling a unitary Fermi liquid, Phys. Rev. Lett. **122**, 093401 (2019).

[34] N. Darkwah Oppong, L. Riegger, O. Bettermann, M. Höfer, J. Levinsen, M. M. Parish, I. Bloch, and S. Fölling, Observation of coherent multiorbital polarons in a two-dimensional Fermi gas, Phys. Rev. Lett. **122**, 193604 (2019).

[35] M. Cetina, M. Jag, R. S. Lous, J. T. M. Walraven, R. Grimm, R. S. Christensen, and G. M. Bruun, Decoherence of impurities in a Fermi sea of ultracold atoms, Phys. Rev. Lett. **115**, 135302 (2015).

[36] M. Cetina, M. Jag, R. S. Lous, I. Fritsche, J. T. Walraven, R. Grimm, J. Levinsen, M. M. Parish, R. Schmidt, M. Knap, et al., Ultrafast many-body interferometry of impurities coupled to a Fermi sea, Science **354**, 96–99 (2016).

[37] N. B. Jørgensen, L. Wacker, K. T. Skalmstang, M. M. Parish, J. Levinsen, R. S. Christensen, G. M. Bruun, and J. J. Arlt, Observation of attractive and repulsive polarons in a Bose-Einstein condensate, Phys. Rev. Lett. **117**, 055302 (2016).

[38] M.-G. Hu, M. J. Van de Graaff, D. Kedar, J. P. Corson, E. A. Cornell, and D. S. Jin, Bose polarons in the strongly interacting regime, Phys. Rev. Lett. **117**, 055301 (2016).

[39] C. J. Pethick, and H. Smith, Bose-Einstein condensation in dilute gases, Second Edition (Cambridge University Press, 2008).

[40] S. Giorgini, L. P. Pitaevskii, and S. Stringari, Condensate fraction and critical temperature of a trapped interacting Bose gas, Phys. Rev. A **54**, R4633–R4636 (1996).

[41] M. Lysebo, and L. Veseth, Feshbach resonances and transition rates for cold homonuclear collisions between ^{39}K and ^{41}K atoms, Phys. Rev. A **81**, 032702 (2010).

[42] L. Tanzi, C. R. Cabrera, J. Sanz, P. Cheiney, M. Tomza, and L. Tarruell, Feshbach resonances in potassium Bose-Bose mixtures, Phys. Rev. A **98**, 062712 (2018).

[43] E. A. Donley, N. R. Claussen, S. L. Cornish, J. L. Roberts, E. A. Cornell, and C. E. Wieman, Dynamics of collapsing and exploding Bose–Einstein condensates, Nature **412**, 295–299 (2001).

[44] G. Mahan, Many-particle physics (Kluwer Academic/Plenum Publishers, 2000).

[45] A. S. Alexandrov, and J. T. Devreese, Advances in Polaron Physics, Vol. 159 (Springer-Verlag Berlin Heidelberg, 2010).

[46] H. Fröhlich, Electrons in lattice fields, Advances in Physics **3**, 325–361 (1954).

[47] S. P. Rath, and R. Schmidt, Field-theoretical study of the Bose polaron, Phys. Rev. A **88**, 053632 (2013).

[48] W. Li, and S. Das Sarma, Variational study of polarons in Bose-Einstein condensates, Phys. Rev. A **90**, 013618 (2014).

[49] R. S. Christensen, J. Levinsen, and G. M. Bruun, Quasiparticle properties of a mobile impurity in a Bose-Einstein condensate, Phys. Rev. Lett. **115**, 160401 (2015).

[50] J. Levinsen, M. M. Parish, and G. M. Bruun, Impurity in a Bose-Einstein condensate and the Efimov effect, Phys. Rev. Lett. **115**, 125302 (2015).

[51] S. M. Yoshida, S. Endo, J. Levinsen, and M. M. Parish, Universality of an impurity in a Bose-Einstein condensate, Phys. Rev. X **8**, 011024 (2018).

[52] L. A. Peña Ardila, and S. Giorgini, Impurity in a Bose-Einstein condensate: Study of the attractive and repulsive branch using quantum Monte Carlo methods, Phys. Rev. A **92**, 033612 (2015).

[53] L. A. Peña Ardila, and S. Giorgini, Bose polaron problem: Effect of mass imbalance on binding energy, Phys. Rev. A **94**, 063640 (2016).

[54] L. A. Peña Ardila, N. B. Jørgensen, T. Pohl, S. Giorgini, G. M. Bruun, and J. J. Arlt, Analyzing a Bose polaron across resonant interactions, Phys. Rev. A **99**, 063607 (2019).

[55] N.-E. Guenther, P. Massignan, M. Lewenstein, and G. M. Bruun, Bose polarons at finite temperature and strong coupling, Phys. Rev. Lett. **120**, 050405 (2018).

[56] A. Camacho-Guardian, and G. M. Bruun, Landau effective interaction between quasiparticles in a Bose-Einstein condensate, Phys. Rev. X **8**, 031042 (2018).

[57] A. Camacho-Guardian, L. A. Peña Ardila, T. Pohl, and G. M. Bruun, Bipolarons in a Bose-Einstein condensate, Phys. Rev. Lett. **121**, 013401 (2018).

[58] P. Makotyn, C. E. Klauss, D. L. Goldberger, E. A. Cornell, and D. S. Jin, Universal dynamics of a degenerate unitary Bose gas, Nat. Phys. **10**, 116–119 (2014).

[59] G. Baym, and C. Pethick, Landau Fermi-liquid theory: Concepts and applications (Wiley-VCH, 1991).

[60] J. Kondo, Resistance Minimum in Dilute Magnetic Alloys, Progress of Theoretical Physics **32**, 37–49 (1964).

[61] S. Nascimbène, N. Navon, K. J. Jiang, L. Tarruell, M. Teichmann, J. McKeever, F. Chevy, and C. Salomon, Collective oscillations of an imbalanced Fermi gas: Axial compression modes and polaron effective mass, Phys. Rev. Lett. **103**, 170402 (2009).

[62] N. Spethmann, F. Kindermann, S. John, C. Weber, D. Meschede, and A. Widera, Dynamics of single neutral impurity atoms immersed in an ultracold gas, Phys. Rev. Lett. **109**, 235301 (2012).

[63] J. Catani, G. Lamporesi, D. Naik, M. Gring, M. Inguscio, F. Minardi, A. Kantian, and T. Giamarchi, Quantum dynamics of impurities in a one-dimensional Bose gas, Phys. Rev. A **85**, 023623 (2012).

[64] C. Zipkes, S. Palzer, C. Sias, and M. Kohl, A trapped single ion inside a Bose-Einstein condensate, Nature **464**, 388–391 (2010).

[65] S. Schmid, A. Härter, and J. H. Denschlag, Dynamics of a cold trapped ion in a Bose-Einstein condensate, Phys. Rev. Lett. **105**, 133202 (2010).

[66] J. B. Balewski, A. T. Krupp, A. Gaj, D. Peter, H. P. Buchler, R. Low, S. Hofferberth, and T. Pfau, Coupling a single electron to a Bose-Einstein condensate, Nature **502**, 664–667 (2013).

[67] R. Scelle, T. Rentrop, A. Trautmann, T. Schuster, and M. K. Oberthaler, Motional coherence of fermions immersed in a Bose gas, Phys. Rev. Lett. **111**, 070401 (2013).

[68] T. Rentrop, A. Trautmann, F. A. Olivares, F. Jendrzejewski, A. Komnik, and M. K. Oberthaler, Observation of the phononic Lamb shift with a synthetic vacuum, Phys. Rev. X **6**, 041041 (2016).

[69] F. Camargo, R. Schmidt, J. D. Whalen, R. Ding, G. Woehl, S. Yoshida, J. Burgdörfer, F. B. Dunning, H. R. Sadeghpour, E. Demler, and T. C. Killian, Creation of Rydberg polarons in a Bose gas, Phys. Rev. Lett. **120**, 083401 (2018).

[70] Z. Z. Yan, Y. Ni, C. Robens, and M. W. Zwierlein, Bose polarons near quantum criticality, Science **368**, 190–194 (2020).

[71] E. Altman, Non equilibrium quantum dynamics in ultra-cold quantum gases, arXiv:1512.00870 (2015).

[72] L. J. Wacker, N. B. Jørgensen, D. Birkmose, N. Winter, M. Mikkelsen, J. Sherson, N. Zinner, and J. J. Arlt, Universal three-body physics in ultracold KRb mixtures, Phys. Rev. Lett. **117**, 163201 (2016).

[73] L. Wacker, N. B. Jørgensen, D. Birkmose, R. Horchani, W. Ertmer, C. Klempt, N. Winter, J. Sherson, and J. J. Arlt, Tunable dual-species Bose-Einstein condensates of ^{39}K and ^{87}Rb, Phys. Rev. A **92**, 053602 (2015).

[74] L. Wacker, Few-body physics with ultracold potassium rubidium mixtures, PhD thesis (Aarhus University, 2015).

[75] N. B. Jørgensen, Observation of Bose polarons in a quantum gas mixture, PhD thesis (Aarhus University, 2018).

[76] U. Schlöder, H. Engler, U. Schünemann, R. Grimm, and M. Weidemüller, Cold inelastic collisions between lithium and cesium in a two-species magneto-optical trap, Eur. Phys. J. D **7**, 331–340 (1999).

[77] L. G. Marcassa, G. D. Telles, S. R. Muniz, and V. S. Bagnato, Collisional losses in a K-Rb cold mixture, Phys. Rev. A **63**, 013413 (2000).

[78] P. D. Lett, R. N. Watts, C. I. Westbrook, W. D. Phillips, P. L. Gould, and H. J. Metcalf, Observation of atoms laser cooled below the Doppler limit, Phys. Rev. Lett. **61**, 169–172 (1988).

[79] M. Landini, S. Roy, L. Carcagní, D. Trypogeorgos, M. Fattori, M. Inguscio, and G. Modugno, Sub-Doppler laser cooling of potassium atoms, Phys. Rev. A **84**, 043432 (2011).

[80] T. Esslinger, I. Bloch, and T. W. Hänsch, Bose-Einstein condensation in a quadrupole-Ioffe-configuration trap, Phys. Rev. A **58**, R2664–R2667 (1998).

[81] R. Grimm, M. Weidemüller, and Y. B. Ovchinnikov, Optical dipole traps for neutral atoms, Adv. At. Mol. Opt. Phys. **42**, 95–170 (2000).

[82] N. F. Ramsey, A new molecular beam resonance method, Phys. Rev. **76**, 996–996 (1949).

[83] A. D. Cronin, J. Schmiedmayer, and D. E. Pritchard, Optics and interferometry with atoms and molecules, Rev. Mod. Phys. **81**, 1051–1129 (2009).

[84] M. G. Skou, T. G. Skov, N. B. Jørgensen, K. K. Nielsen, A. Camacho-Guardian, T. Pohl, G. M. Bruun, and J. J. Arlt, Non-equilibrium quantum dynamics and formation of the Bose polaron, Nat. Phys. (2021).

[85] M. G. Skou, T. G. Skov, N. B. Jørgensen, and J. J. Arlt, Initial dynamics of quantum impurities in a Bose–Einstein condensate, Atoms **9**, 22 (2021).

[86] R. J. Fletcher, R. Lopes, J. Man, N. Navon, R. P. Smith, M. W. Zwierlein, and Z. Hadzibabic, Two-and three-body contacts in the unitary Bose gas, Science **355**, 377–380 (2017).

[87] E. Braaten, D. Kang, and L. Platter, Short-time operator product expansion for rf spectroscopy of a strongly interacting Fermi gas, Phys. Rev. Lett. **104**, 223004 (2010).

[88] S. Tan, Energetics of a strongly correlated Fermi gas, Annals of Physics **323**, 2952–2970 (2008).

[89] J. T. Stewart, J. P. Gaebler, T. E. Drake, and D. S. Jin, Verification of universal relations in a strongly interacting Fermi gas, Phys. Rev. Lett. **104**, 235301 (2010).

[90] E. D. Kuhnle, H. Hu, X.-J. Liu, P. Dyke, M. Mark, P. D. Drummond, P. Hannaford, and C. J. Vale, Universal behavior of pair correlations in a strongly interacting Fermi gas, Phys. Rev. Lett. **105**, 070402 (2010).

[91] E. Braaten, D. Kang, and L. Platter, Universal relations for identical bosons from three-body physics, Phys. Rev. Lett. **106**, 153005 (2011).

[92] R. J. Wild, P. Makotyn, J. M. Pino, E. A. Cornell, and D. S. Jin, Measurements of Tan's contact in an atomic Bose-Einstein condensate, Phys. Rev. Lett. **108**, 145305 (2012).

[93] M. Drescher, M. Salmhofer, and T. Enss, Theory of a resonantly interacting impurity in a Bose-Einstein condensate, Phys. Rev. Research **2**, 032011 (2020).

[94] M. G. Skou, T. G. Skov, N. B. Jørgensen, K. K. Nielsen, A. Camacho-Guardian, T. Pohl, G. M. Bruun, and J. J. Arlt, Life and death of the Bose polaron, in preparation.

[95] Y. E. Shchadilova, R. Schmidt, F. Grusdt, and E. Demler, Quantum dynamics of ultracold Bose polarons, Phys. Rev. Lett. **117**, 113002 (2016).

[96] K. K. Nielsen, L. A. Peña Ardila, G. M. Bruun, and T. Pohl, Critical slowdown of non-equilibrium polaron dynamics, New Journal of Physics **21**, 043014 (2019).

[97] K. K. Nielsen, Dynamics of quantum impurities in a Bose-Einstein condensate, PhD thesis (Aarhus University, 2020).

[98] B. Field, J. Levinsen, and M. M. Parish, Fate of the Bose polaron at finite temperature, Phys. Rev. A **101**, 013623 (2020).

[99] J. T. Devreese, and A. S. Alexandrov, Fröhlich polaron and bipolaron: recent developments, Reports on Progress in Physics **72**, 066501 (2009).

[100] M. Hohenadler, and P. B. Littlewood, Quantum Monte Carlo results for bipolaron stability in quantum dots, Phys. Rev. B **76**, 155122 (2007).

[101] P. A. Bobbert, T. D. Nguyen, F. W. A. van Oost, B. Koopmans, and M. Wohlgenannt, Bipolaron mechanism for organic magnetoresistance, Phys. Rev. Lett. **99**, 216801 (2007).

[102] W. E. Liu, Z.-Y. Shi, J. Levinsen, and M. M. Parish, Radio-frequency response and contact of impurities in a quantum gas, Phys. Rev. Lett. **125**, 065301 (2020).

[103] A. L. Gaunt, T. F. Schmidutz, I. Gotlibovych, R. P. Smith, and Z. Hadzibabic, Bose-Einstein condensation of atoms in a uniform potential, Physical Review Letters **110**, 200406 (2013).

[104] B. Mukherjee, Z. Yan, P. B. Patel, Z. Hadzibabic, T. Yefsah, J. Struck, and M. W. Zwierlein, Homogeneous atomic Fermi gases, Phys. Rev. Lett. **118**, 123401 (2017).

[105] Z. Hadzibabic, and J. Dalibard, Two-dimensional Bose fluids: An atomic physics perspective, Riv. Nuovo Cimento **34**, 389–434 (2011).

[106] W. Casteels, J. Tempere, and J. T. Devreese, Polaronic properties of an impurity in a Bose-Einstein condensate in reduced dimensions, Phys. Rev. A **86**, 043614 (2012).

[107] V. Pastukhov, Polaron in dilute 2D Bose gas at low temperatures, Journal of Physics B: Atomic, Molecular and Optical Physics **51**, 155203 (2018).

[108] L. A. Peña Ardila, G. E. Astrakharchik, and S. Giorgini, Strong coupling Bose polarons in a two-dimensional gas, Phys. Rev. Research **2**, 023405 (2020).